# Transient Thermography for Detection of Micro Defects in Multilayer Thin Films

By

Xiaoting Wang

A Doctoral Thesis
Submitted in Partial Fulfilment of the Requirements
For the Award of
Doctor of Philosophy of Loughborough University
Jan 2016

LOUGHBOROUGH UNIVERSITY

WOLFSON SCHOOL OF

MECHANICAL AND MANUFACTURING ENGINEERING

Dated: January 2016

First Supervisor: ________________________________________

David C. Whalley

Second Supervisor: ________________________________________

Vadim V. Silberschmidt

# Contents

# List of Figures

# List of Tables

# List of Abbreviations

| | |
|---|---|
| CPW | Coplanar Waveguide |
| CTE | Coefficients of Thermal Expansion |
| CT | Computed Tomography |
| DTT | Dynamic Thermal Tomography |
| DWT | Discrete Wavelength Tunable |
| FEA | Finite element analysis |
| FIB | Focused ion beam |
| FPA | Focal Plane Arrays |
| IC | Integrated Circuits |
| ITO | Indium Tin Oxide |
| IR | Infrared |
| NDT | Non-Destructive Technique |
| MEMS | Micro-Electronic-Mechanical System |
| NETD | Noise Equivalent Temperature Difference |
| NI | National Instruments |
| PED | Partial Differential Equations |
| SEM | Scanning Electron Microscopy |
| SNR | Signal-to-Noise Ratio |
| TCT | Thermal Cycling Tests |
| TEM | Transmission Electron Microscopy |
| XRD | X-Ray Diffraction |

# Abstract

Delamination and cracks within the multilayer structure are typical failure modes observed in microelectronic and micro electro mechanical system (MEMS) devices and packages. As destructive detection methods consume large numbers of devices during reliability tests, non-destructive techniques (NDT) are critical for measuring the size and position of internal defects throughout such tests. There are several established NDT methods; however, some of them have significant disadvantages for detecting defects within multilayer structures such as those found in MEMS devices.

This thesis presents research into the application of transient infrared thermography as a non-destructive method for detecting and measuring internal defects, such as delamination and cracks, in the multilayer structure of MEMS devices. This technique works through the use of an infrared imaging system to map the changing temperature distribution over the surface of a target object following a sudden change in the boundary conditions, such as the application of a heat source to an external surface. It has previously been utilised in various applications, such as damage assessment in aerospace composites and verification of printed circuit board solder joint manufacture, but little research of its applicability to MEMS structures has previously been reported.

In this work, the thermal behaviour of a multilayer structure containing defects was first numerically analysed. A multilayer structure was then successfully modelled using COMSOL finite element analysis (FEA) software with pulse heating on the bottom surface and observing the resulting time varying temperature distribution on the top. The optimum detecting conditions such as the pulse heating energy, pulse duration and heating method were determined and applied in the simulation. The influences of thermal properties of materials, physical dimensions of film, substrate and defect and other factors that will influence the surface temperature gradients were analytically evaluated. Furthermore, a functional relationship between the defect size and the resulting surface temperature was obtained to improve the accuracy of estimating the physical dimensions and location of the internal defect in detection. Corresponding experiments on specimens containing artificially created defects in macro-scale revealed the ability of the thermographic method to detect the internal defect. The precision of the established model was confirmed by contrasting the experimental results and numerical simulations.

Keywords: micro-electronic-mechanical system (MEMS), transient infrared thermography, non-destructive technique (NDT), delamination

# Acknowledgements

I would like to acknowledge the financial support from Wolfson School of Mechanical and Manufacturing Engineering in Loughborough University, which granted me the opportunity to undertake this research. I would like to express my sincere gratitude to both of my supervisors, David C. Whalley and Prof. Vadim V. Silberschmidt in Wolfson School of Mechanical and Manufacturing Engineering, for their constant support and guidance throughout this research. They have always been patient and flexible for research ideas, which is beneficial to improving my capability as a real researcher.

Many thanks are given to all the staff and fellow researchers in Wolfson School who have been supportive in various aspects of this thesis and to my personal learning. Particularly, I appreciate the discussion, assistance and supervision received from Mr Andy Sandaver and Mr Bob Temple in sample preparation and the operation of experimental facilities. Meanwhile, I am thankful to Dr Junyan Liu from Harbin Institute of Technology for his support on the lock-in thermographic NDT test.

Last but not least, I am deeply grateful to my parents for their financial support in the difficult times during my PhD study.

# Chapter 1 Introduction

In this introductory chapter, background information and the aims of this research are introduced, followed by a discussion of the structure of this thesis.

## 1.1 Background

Multilayer structures are widely applied in integrated circuits (ICs) and related industrial micro-engineering fields, such as microelectromechanical systems (MEMS), actuators, sensors and solar cells [1], [2], [3]. These structures contrast monolithic engineering structures, which are typically formed from a single piece of a material. Multilayer structures can serve as functional components in devices, occupy a reduced area, and avoid the cross wiring of large ICs [4]. For example, the main advantage of applying a multilayer structure to piezoelectric actuators is that it enables larger displacements to be generated than possible with a single layer, given the same total thickness, for a given actuating voltage [5] [6].

However, multiple layers in a device require the use of more than one material, one or more material interfaces, and more than one manufacturing step, which increases the probability of failure during manufacturing and service. The interface between a thin film and a substrate, or between films, is very important to the stability of a composite structure [7]. Defects, such as cracks, delamination, voids, etc., may occur in the multilayer structure during the manufacturing process. For example, the adverse influences of impurities, such as metal impurities, organic contaminants, particulate matter and other contaminants, created during the manufacture of devices have been shown in numerous studies. In multilayer structure manufacturing (such as oxidation, plating, sputtering, etc.), contaminants can lead to the abnormal growth and peeling of thin films [8].

Thermal stresses due to differences between the coefficients of thermal expansion (CTE) of different layers may cause bulking, delamination and even peeling during temperature excursions. Although temperature excursions during the service of a device are lower than those during manufacturing, fracture may occur due to cumulative damage fatigue, which limits the device lifetime [9].

The potential influence of micro defects on the device performance is amplified as the feature sizes decrease. Thus, higher resolution defect detection methods for multilayer structure devices are necessary to guarantee the quality of the devices. Using high-resolution methods in reliability testing to monitor the state of potential failure defects will contribute to determining and lengthening the device lifetime.

Many approaches have been established to detect defects in micro-engineered devices [10-12]. Destructive detecting methods are most common in reliability testing due to their ability to provide clear and visual results of defects inside devices. For instance, cross-sectioning and polishing specimens embedded in resin before observation under an optical or electron microscope is a common method for detecting defects inside an object. However, considering the high cost of some devices and the complex processes of micromachining, non-destructive techniques (NDT) are preferable for measuring the size and position of defects inside a device. More importantly, non-destructive detection can monitor the evolution of defects, such as cracks, inside a specimen during reliability testing, such as thermal cycling tests (TCT), tensile tests, etc. This type of analysis cannot be achieved using destructive methods because the irreversible damage to specimens prevents repeated detection. Defects may also be expanded during sample preparation processes in destructive methods.

The detection principles used in NDT typically rely on the propagation of sound or electromagnetic radiation and the inherent differences in the properties of materials and defects to inspect the internal device structure [12]. X-rays and high-frequency sound waves are currently the most common methods used internal scanning at both the microscale and macroscale and are especially powerful for the detection of voids [13-14]. However, X-rays are not effective at identifying delamination, and ultrasound scanning performs poorly when there is delamination in multilayer structures due to echoes [14-15]. Meanwhile, high costs and long times are required for the maintenance of X-ray and ultrasound equipment. In contrast, thermographic inspection, as a non-destructive test method, measures the damage in a structure by using an infrared (IR) imaging system to map the temperature over the surface of a target object. The detecting principle of IR thermography is that defects act as thermal barriers to disrupt the temperature distribution, thus inducing a temperature difference on the surface between the damaged and less-damaged areas [17]. Although the temperature difference may decrease due to transversal thermal conductance parallel to the interface, the difference can be magnified by pulse heating. Moreover, high-resolution IR imagers are relatively inexpensive, portable and safe compared with X-ray equipment.

## 1.2 Aims and objectives of this thesis

This PhD research project aims to establish a method for evaluating internal damage in multilayer structures through mapping the temperature distribution over the surface of a target object. This work involves reliability testing, comparison of destructive and non-destructive detection methods, numerical simulation of the thermographic method and related thermography experiments. The objectives are therefore identified as follows:

- The main failure modes of target and defect features are determined though TCT and focused ion beam (FIB) measurements. A MEMS DC switch composed of a nickel film plated onto a silicon substrate is used as the test case, and the generation mechanism of cracks and delamination between the film and substrate are discussed.

- Geometrical and thermal models of multilayer structures and interfacial defects are built based on the experimental results. The geometry and thermal properties of the defects and seed layers are simplified, and the parameters of each material are determined.

- A qualitative physical model is established. The basic principles and theoretical calculation of the thermal distribution are elaborated, including one-dimensional and two-dimensional mathematical models and steady-state and unsteady-state thermal conduction calculations.

- The factors influencing the temperature mapping and detection resolution are quantitively determined, including the ratio of defects to the entire system, the heating period, the data acquisition time, convective cooling, and the material properties (heat conductivity, heat capacity and density).

- The relationship between the specific defect size and the resulting surface temperature distribution is investigated to formulate a method to deduce the location and geometry of defects from the temperature data.

- The simulation results are compared with those from related experiments and simulations to estimate the applicability and detectability of transient thermographic detection methods.

## 1.3 Thesis structure

This thesis contains a total of seven chapters. Figure 1. 1 illustrates the structure of the thesis. An introduction to the research is presented in Chapter 1, outlining the background, aims and objectives of this thesis. Some of the current challenges in the electronics industry are also illustrated, and the significance of researching the thermal detection of defects is explained.

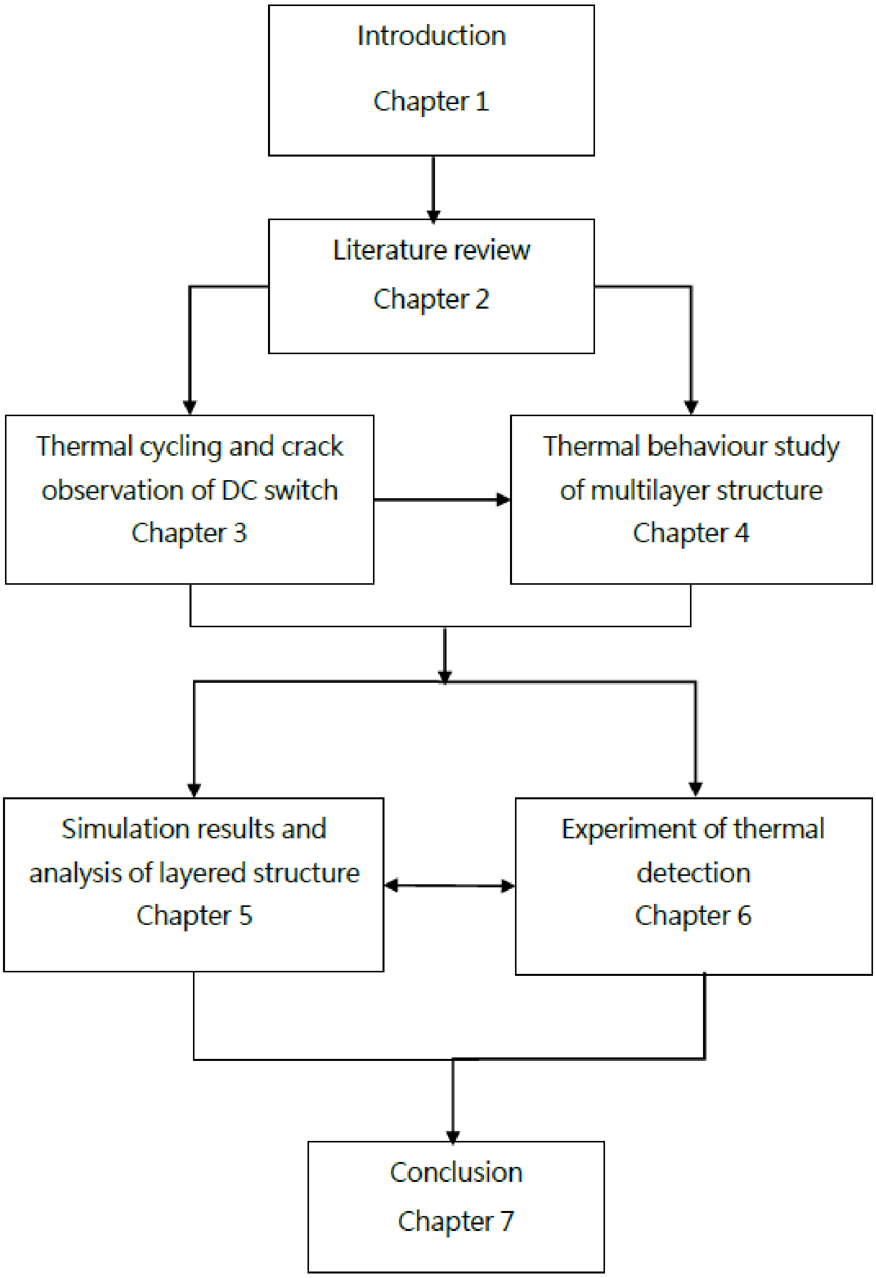

Figure 1. 1 Overview of the thesis structure.

The literature review in Chapter 2 provides a more detailed comparison of the various inspection methods available for MEMS reliability testing, as well as an overview of the early history of thermal detection by NDT methods, recent achievements and applications in thermal detection research.

Chapter 3 details the type of MEMS DC switch used in the main case study of this thesis, which involves a multilayer structure and metal/semiconductor interface. In addition, some reliability and detection experiments on these switches are used to determine the main failure modes of the switch and the geometry and position of typical defects. This chapter also explains why defect detection methods such as X-ray and FIB are not suitable for such complex metal/semiconductor structures.

Chapter 4 presents the results of the numerical analysis of the thermal behaviour of layered/multilayer structures with defects. The main heat transfer mode of the defects and the bonding interface are discussed, and the steady and unsteady states of thermal diffusion are investigated.

Chapter 5 describes the finite element analysis (FEA) of thermal multilayer structures modelled using the COMSOL software, with static and transient heating on the bottom of the substrate and IR thermography on the top of the film. A transient excitation source is introduced to amplify the temperature differences due to defects. Meanwhile, to ensure the general applicability of the method, other materials regularly used in MEMS manufacturing are considered by replacing the original material in the model.

Chapter 6 lists various instruments used for thermal detection, such as those for excitation sources, receiving terminals (thermal cameras), specimen preparation processes, and experimental results.

Finally, Chapter 7 concludes the thesis with a summary of achievements and discusses potential future work.

# Chapter 2 Context and Literature Review: Thermography as a Non-Destructive Detection Method for MEMS Devices

## 2.1 Introduction

The principal of this literature review is to provide significant insights into the basic theory of transient thermography as a detection method and the advantages of this method for MEMS reliability testing. First, the category and structures of MEMS devices are introduced, as well as the most common failure modes of MEMS. Second, some commonly used detection methods are introduced, including destructive and non-destructive detection methods, the advantages and disadvantages of each method are discussed, and the methods are compared with thermography. Third, the history, application, associated technologies and research achievements of thermographic detection are presented.

## 2.2 MEMS Device Technologies

Unlike purely microelectronic devices, MEMS contain both electronic devices and mechanical components produced by microfabrication techniques. The integration of micromechanical structures with electronics provides mechanical functionality, depending on if these elements can move, as well as electrical functionality. However, the mechanical components also risk causing the failure of MEMS devices. Having a cognizance of the structural and material properties of the MEMS devices helps to define the failure mechanisms and suitable detection methods.

### 2.2.1 MEMS Structures

Microsensors and actuators are the most common functions of MEMS devices and are used in a wide variety of health care, automotive, and military applications [16]. Moreover, multiple thin films are common structures in these devices. For example, pressure sensors are commonly designed and fabricated with piezoresistive, nanosized thin films on silicon substrates in a Wheatstone bridge structure (an electrical circuit used to measure unknown electrical resistance by balancing two legs of a bridge circuit). The main structure consists of a monocrystalline silicon diaphragm layer and deposited silicon strain gauges [17-18]. As shown in Figure 2.1, a capacitive pressure sensor was composed of thin films on the substrate [17]. The thin film properties are therefore important.

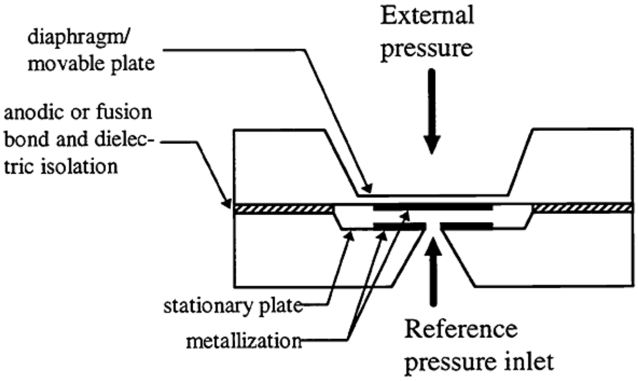

Figure 2.1 Cross-section schematic of a micromachined capacitive pressure sensor with thin films on top [17].

Structures for RF MEMS applications are commonly developed on glass or semiconductor substrates and also have a multilayered thin film structure. For example, a band-stop filter, designed by Simion [19], was monolithically integrated to a coplanar waveguide (CPW) inductor using MEMS. Such structures are typically fabricated on 400 µm-thick, high-resistivity silicon substrates covered with a thermal $SiO_2$ layer (1 µm thickness). A 1 µm-thick metal layer was sputter-patterned to define the CPW. Reliability assessments concentrated on the junction of the MEMS and inductor.

In optical MEMS applications, photonic MEMS tunable lasers have inspired significant research into developing dynamic and optical networks [20]. These systems achieve fast tuning speeds and low power consumption through the inclusion of micromachined mirrors on silicon wafers. The MEMS discrete wavelength tunable (DWT) laser includes a simple mirror configuration that uses a curved mirror as the external reflector to form an external cavity to the semiconductor laser. The laser output can be tuned to different wavelengths by actuating the mirror to change the cavity length [21]. MEMS injection-locked tunable lasers were fabricated on silicon or insulating wafer of gratings, actuators, microlens and trenches for the laser chips and optical fibres. The injection locking method is an approach to locking the oscillation state of a laser by injecting external laser light [22]. A coupled-cavity laser is formed by two laser chips (lasing chip and tuning chip) and a movable parabolic mirror [22]. Moreover, a recently demonstrated MEMS tunable dual-wavelength laser integrates a semiconductor gain chip with silicon micromachined grating and mirrors onto a silicon chip [25].

Switches are typical acceleration sensors widely applied in toys, accessories, automobiles and other applications [24]. The basic structure of a switch is a proof mass suspended by springs or cantilevers, working as a movable electrode. When sufficient acceleration is applied, the switch will move towards the sensitive direction and contact the fixed electrode, switching the external circuit in the ON position [26]. In the early 1980s, bulk micromachined piezoresistive silicon accelerometers were commonly applied in pressure sensor technology [104]. However, due to certain drawbacks, such as low drift, uncalibrated offset and sensitivity, capacitive silicon accelerometers, which have the benefits of lower thermal drift and high resolution, have become established alternatives to piezoresistive devices [27]. In addition to capacitive relays, electrothermal switches, electrostatic microactuators, and electromagnetic micro-relays, are also commonly used switches in industry [28]. The materials and structure involve typical multilayered metal with semiconductor and simulated cantilever beams; for instance, Barracks [29] designed a micromechanical switch with electroplated nickel using a four-level surface micromachining process.

### 2.2.2 Failure Mechanisms in MEMS Devices

This section introduces some of the failure mechanisms of MEMS consisting of multilayer structures. Many MEMS failure modes are introduced during fabrication and operation processes and are related to the device structure [30]. For electrical and mechanical devices, failure often occurs during operating and manufacturing processes. One of the most general methods for the production of MEMS is subtractive bulk micromachining, in which 3D structures are fabricated through lithographic patterning, followed by etching on a single-crystal silicon substrate. Another method is surface micromachining, which is an additive method in which layers of semiconductor (polysilicon, silicon nitride, silicon dioxide, etc.) and metal materials are sequentially added and patterned to form 3D structures. Bulk and surface micromachining methods are limited by the materials used [31].

Most MEMS are designed with basic parts recurring throughout the field, such as cantilever beams (single-side or double-side fixed) and membranes (thin pliable sheets of material closed at the sides to another structural unit) [32]. The problem is that multiple layers must be built up to form active devices, requiring adhesion between layers, which is of great practical concern [31]. Thin films can be built by deposition and patterning on wafers. Moreover, membrane devices are a subclass of thin-film devices, which are manufactured on top of a thin film without the mechanical support of a full wafer, where only a thin membrane supports the structure [33].

Failure mechanisms, such as delamination, cracks and voids, can occur in devices due to mismatched thermal expansion coefficients [34, 35], especially due to contamination during the manufacturing process [36-37]. Regardless of the actual cause, the effects of delamination can be disastrous. Moreover, during service, thermal stress or mechanical stress due to bending or stretching can lead to the loss of the adhesive bond [38-39]. Thus, a method for monitoring defect generation and growth during the manufacturing and operating processes is necessary to tailor the lifetime and improve the devices.

### 2.2.3 Destructive Detection in MEMS Devices

Optical and electron microscopes are commonly used for the defect analysis of MEMS devices [40]. The systems must be sectioned and well polished to obtain information on internal defects. Electron microscopy methods, such as scanning electron microscopy (SEM), transmission electron microscopy (TEM), etc., can achieve high-magnification and high-resolution images of the surface roughness and cracks. However, all samples must be of an appropriate size to fit in the specimen chamber, generally mounted on a specimen stub. For some insulator and semiconductor materials, the sample must be coated with a conductive layer of metal to inhibit charging [41]. Thus, electron microscopy is a destructive testing method.

Considering the large amount and high cost of devices consumed in destructive testing, enhanced NDT testing can instead be used to monitor the occurrence of cracks and delamination during the manufacturing process in real time during the reliability test in order to reduce the risk of defects and improve the finished product yield. For example, in a TCT or strength test, systems can be removed and tested for defects by NDT and then readmitted to the cycling test. NDT does not require the destruction of any specimens for the detection of internal defects. Similarly, the non-destructive monitoring of defects during service could predict the lifetime of a device or product. Traditional reliability test methods, for instance, TCT, typically require many fatigue tests and specimens [42]. Thus, the non-destructive detection of defects during reliability testing may help to increase the efficiency of reliability analysis and reduce the consumption of specimens.

## 2.3 Non-Destructive Detection Techniques

Non-destructive detection is an important cross-subject technology that involves the continuous monitoring or periodic inspection of the actual components to identify internal defects within devices, such as cracks or voids [43]. Considering that the length of such defects can range from hundreds of nanometres to hundreds of micrometres, depending on the structure and size of the device, non-destructive detection methods are required to achieve high resolution. Established non-destructive methods include ultrasonic detection, radiography detection, eddy current testing, magnetic techniques and thermography [44].

### 2.3.1 Ultrasonic Detection

Ultrasound has been commonly and successfully used in non-destructive detection for many years [45]. In such methods, defects in the object under examination are measured by their ultrasound response using measurements of the scattering or reflection of ultrasound from any interface that separates regions of different acoustic impedance [46]. The resulting echo signal is also usually received by a transmitting transducer.

The advantage of ultrasonic detection is the ability to produce images of the samples at specific depth levels. This method is useful for locating cracks and voids in monolayer or bulk materials with high resolution and high magnification. For 3D detection, a resolution of approximately 10 μm can be achieved, as that is the limit of the ultrasound wavelength [47]. However, for objects with complex structures, such as multilayer structures, the multiple reflections of the waves at each interface, an ultrasonic signature, can appear very complex, due to different propagation modes, as a function of both the ultrasonic probe parameters and the material characteristics, creating echoes [15]. It is therefore difficult to produce a good image of internal defects or locate their position in a device.

Meanwhile, ultrasound excitation has long been suspected to not be completely non-destructive. For example, the growth of pre-existing cracks under high excitation power has been reported many times in the literature [48-50]. Scanning acoustic microscope also requires the whole specimen to be immersed in liquid, which is a type of contacting detection. This method also requires the object to be small enough to fit inside the testing chamber, which is inconvenient for detection during operation if the object was previously assembled in a large facility [51]. The contacting detection method may contaminate the object and limits the dimension of the specimen as well.

### 2.3.2 Radiography Detection

X-rays, gamma-rays and particle rays, as types of short wavelength electromagnetic radiation, are used for NDT because of their ability to penetrate solid media while being partially absorbed. The amount of absorption is related to the density and thickness of the material that the radiation is passing through, as well as characteristics of the radiation. The radiation passing through the material can be measured by electronic sensors [12]. X-ray computed tomography (CT) scanning is a radiation-based detection method that has been widely used for non-destructive detection. Image reconstruction using X-ray CT scanning provides a method for the non-invasive measurement of the internal structure from external measurements. This method can achieve high-quality, high-resolution and three-dimensional defect detection [53]. However, radiation detection is dependent on the specific materials in the sample. For instance, when radiation penetrates a complex structure containing metal and semiconductor materials, the metal parts will absorb most of the radiation, while the semiconductor parts will be relatively transparent. If a defect, such as a crack or delamination, occurs between the metal and semiconductor layers, it will be very difficult to observe by radiation detection because the semiconductor layer and thus the delamination will be relatively transparent. More importantly, ionizing radiation can injure human health, and thus a protection chamber is required; in addition, radiation methods require a long time for processing, and the instruments are costly [51].

### 2.3.3 Other NDT Methods

I. Eddy current testing

Eddy current methods can be used for the non-destructive evaluation of cracks and other defects in any electrically conductive material because the defects interrupt the flow of eddy currents generated in the material and change the magnetic field. Then, the presence of very small cracks can be detected by monitoring changes in the eddy current flow [43, 44, 54, 56]. However, this method is only applicable to electrically conductive materials. Edge effects are well-known disadvantages of eddy current testing because the eddy current cannot flow at the edge of an object; thus, the current flow will be disordered, and the test results will be faulty [55].

II. Magnetic particle inspection

Magnetic particle inspection was the first magnetic method put into widespread use for non-destructive detection. This method is very simple in principle, and the technique depends on the leakage of magnetic flux at the surface of a ferromagnetic material near surface-breaking or near-surface flaws [57]. However, due to limitations of ferromagnetic materials, magnetic methods have not yet been fully exploited, when compared, for example, with ultrasound and eddy current testing [58].

III. Optical interferometric methods

Optical interferometric techniques are used for the measurement of small displacements, refractive index changes and surface irregularities. The working principle is that when two waves with the same frequency combine, the resulting intensity pattern is determined by the phase difference between the two waves. The relative phase difference can be used to measure the surface displacement, which can be enhanced by an external load if the object contains internal defects [59]. Typical external loads include negative pressures [60], tensile loads [61], vibrations [62], etc. This method benefits from high resolution and is applicable to all kinds of materials. However, the method requires long testing times.

### 2.3.4 Infrared Thermography

Thermography is a method to measure and map the temperature on the surface of an object [63]. The principle of thermography for NDT defect detection involves the difference in heat transfer between a continuous solid material and a defect-containing area, as the defect will highly obstruct heat transfer such that the temperature at the surface over the defect area will be much different than that over the defect-less area. The IR radiation emitted from the surface of all objects with a temperature above absolute zero can be detected by a thermal IR camera and processed to create an image. Thus, compared with the NDT detection methods mentioned above, IR thermography, as a non-destructive method, offers significant advantages, such as non-contact measurement, fast acquisition time and simple test setup [64, 65]. A major advantage of IR thermography is its ability to detect and monitor subsurface cracking [68]. The comparison of thermography and other methods is shown in Table 2.1. Further details about the history, application and challenges of thermography will be introduced in the next section.

Table 2.1 A comparison of infrared thermography with other non-destructive detection methods.

| | **Applicable defect location and types** | **Applicable materials** | **Advantages** | **Disadvantages** |
|---|---|---|---|---|
| **Ultrasound [45,46]** | Internal, surface voids, cracks | Non-metallic, metallic, composite materials | High accuracy, capable to locate defect [15] | Poor quality for complex geometry and multilayer structure [48,49,50] |
| **Radiation [12,53]** | Internal voids | Non-metallic, metallic, composite materials | High quality and resolution [53] | High cost in facility, high risk for health, long acquisition time, poor quality for multilayer structures [51] |
| **Eddy current [43,44,54]** | Surface, sub-surface cracks | Electrically conductive materials | Fast acquisition time, non-contact, automatic | Not suitable for non-metal materials, edge effect [55] |
| **Magnetic [57,58]** | Surface, sub-surface defects | Ferromagnetic materials | Highly sensitive to surface defects, easy operation, intuitional and believable results | Limited to ferromagnetic materials, poor performance in depth determination |
| **Optical interferometric methods [59]** | Surface, sub-surface defects | Metallic, non-metallic, composite materials | High quality and resolution [60,61,62] | Long acquisition time, risk to damage specimen |
| **Thermography [63,69]** | Surface, sub-surface, internal cracks and voids, interface delamination in multilayer structure | metallic, non-metallic, composite materials | Fast acquisition time, non-contact, large inspection area, real-time monitoring | Some objects require coating on surface, depth measurement needs calibration |

## 2.4 Infrared Thermography-Based Defect Detection: Technology and History

As discussed in section 2.3.5, IR thermography offers a number of advantages in NDT detection. IR radiation was discovered by Sir William Herschel in the spring of 1800. IR radiation is radiant energy outside of the visible spectral region and is emitted by all objects with a temperature above absolute zero [70]. Thermographic cameras allow the creation of an image using IR radiation emitted from the surface of an object, which is called thermography [71]. This section will introduce the technology used for thermography, as well as its applications and development history.

### 2.4.1 Infrared Thermography Inspection Excitation Methods

There are two types of approaches to IR thermography-based inspection depending on the external excitation method: passive and active methods. The passive approach can be applied to objects that are naturally at a different temperature from the ambient atmosphere [72], such as animals or machines during operation. This method investigates the heat from the measured object and requires no external heat power. The first investigations using the passive approach date from the 1930s (e.g., Barker in 1934 [73]). This method has been mainly used in military applications to search for targets in poor visibility conditions, such as at night or in fog [72].

Unlike the passive method, in active methods, an external stimulus is necessary to produce a useful thermal contrast between the feature of interest and the background [74]. External heat applied to part of an object causes the local temperature to increase, and the temperature gradient increases the temperature of other parts of the object through thermal conduction. A defect, such as delamination or a crack, will obstruct and reflect parts of the thermal wave, such that the temperature of the opposite surface over the defect will be lower than that of a surface far away from the defect; in contrast, the heated surface will show a higher temperature on the surface over the defect due to reflection of the heat.

The active approach was first investigated in the 1970s for clinical use for tumour detection by implanting an artificial persistent heat source under the skin [76], but this approach was limited by the poor resolution of contemporary thermal cameras. In 1981, McLaughlin used a heat source outside of a graphite/epoxy substrate with 0.64 cm-diameter drilled holes as an external thermal field to generate transient thermal patterns. Perturbations in the thermal patterns read by IR detectors (sensors, cameras, or liquid crystals) imply the presence of a defect [78].

External heat resources will increase the temperature of the specimen until the whole system reaches a steady state where the temperature does not change over time. However, the steady-state heating method achieves only a coarse resolution in the detection of high-conductivity, microsized materials because the temperature difference on the surface induced by internal defects is very small in the steady state, while large undesired noise in the surface temperature data may be created by certain conditions of the specimens and ambient environment, such as surface roughness and airflow on the surface [79].

### 2.4.2 Transient Thermography Method

The general approach to solving this problem is by reducing the noise or increasing the temperature difference. Historically, thermographic NDT development has focused on (a) the excitation source, such as form, intensity, and length; (b) the image display and final processing approach; and (c) application research, such as the type of materials or defects involved.

Transient and lock-in thermography methods are the two most commonly applied active methods, which use rapidly varying excitation methods [80]. Transient thermography and lock-in thermography are used for similar component/structure inspection applications but rely on different excitation methods [82].

I. Transient thermography

For transient thermography, the surface of the subject to be inspected is rapidly stimulated by a pulse of energy, which can be deployed by optical devices such as flash lamps, by laser beams, by a blast of chilled air (for heat pulsed stimulation) or mechanically (e.g., a sonic or ultrasonic transducer) [83].

As shown in Figure 2.2, before the overall temperature of an object reaches a steady value, the surface temperature ($S_1$) over a defect rises much more slowly than the surface temperature ($S_2$) far away from the defect. The temperature difference between $S_1$ and $S_2$ before reaching the steady state is much larger, and the resolution of thermographic detection can be increased if the temperature image is caught when the temperature difference is large enough.

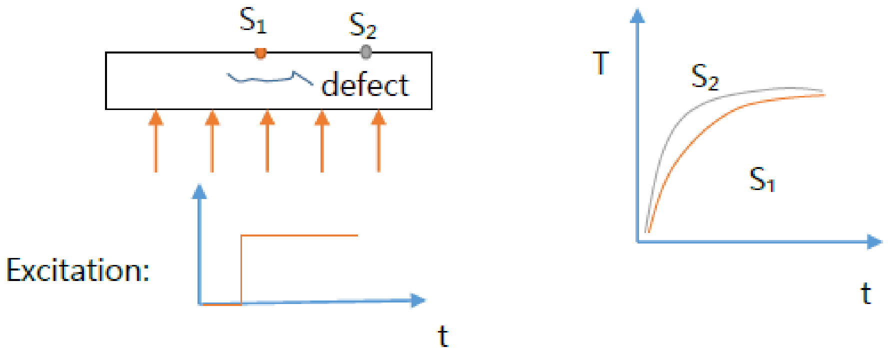

Figure 2.2 Transient thermography schematic of the change in surface temperature over time.

Pulse thermography was first used in the 1960s to examine the thermal diffusivity, heat capacity and thermal conductivity by flash heating the bottom surface. In the experiment, a commercial flash tube that can dissipate 400 Joules of energy in each flash was used as an exciting resource, and the thermograph of the surface was measured using a thermocouple and recorded with an oscilloscope and camera. Additionally, the mathematical and physical principles of measuring the thermal diffusivity properties of homogeneous materials have been well discussed by Parker and Jenkins from the US Naval Radiological Defence Laboratory [84].

Because the main factor of thermographic NDT depends on the resolution and frame frequency of the IR thermal camera, the ability of the IR thermal camera is mainly limited by the IR detector, the detector cooling system, the camera lens, etc. The first thermal imaging camera was developed for the military in the 1950s, contained single-element detectors that scanned scenes and produced line images. The first IR camera for commercial applications was developed in the 1960s and was used for power line inspections. However, microsized detection only began in the late 1980s, after microbolometer technology was developed [86-87]. Thus, thermographic NDT rapidly developed with the development of radiation-based detection techniques.

In the 1980s, scanning IR cameras were introduced as detection instruments, and the detection of internal defects and the internal structure of common microelectronic materials (such as copper, nickel and Teflon) was attempted by Milne and Reynolds [85]. The excitation method used in this experiment was a simple photograph flash-tube that was discharged through a resistance-capacitance circuit and photographed in transmission mode. Although the thermal camera combined fast scanning speeds with relatively good spatial resolution (1.2 radians) and temperature resolution (0.2 °C) and was synchronized to fire the flash at the beginning of a frame, Milne [85] failed to achieve any recording showing the temperature difference between the defect surface and the far surface due to limitations of the thermal camera.

II. Lock-in thermography

The principle of lock-in thermography (also referred to as modulated thermography) is based on the application of a periodic stimulating energy wave. The input energy wave is absorbed and phase shifted as it passes through the surface of the object. Similarly, when the input energy wave reaches the defect area where the thermal properties are different from surrounding material, it is partly reflected back to the surface of the object. The input wave and reflected wave create an interference pattern in the local surface temperature. The internal defect is then evaluated by the phase shift of the local surface temperature of the input signal [83]. However, the lock-in thermography method requires sustained heating that may greatly increase the temperature of the object, causing damage.

### 2.4.3 Infrared Thermography Inspection Observation Methods

In the detection process, there are two possible observation methods: reflection, where the heating source and thermal detector are located on the same side of the object under inspection, as shown in Figure 2.3 (left), and transmission, where the thermal source and detector are placed on opposite sides of the object [74-75], as shown in Figure 2.3 (right). The observation method is influenced by the dimension size, depth and geometry of the defect and the structure and material of the object.

In the reflection method, mechanical excitation is transformed into heat on the surface of the specimen. Thermal waves are spread by conduction through the specimen until they reach the defects and then are reflected back to the surface due to thermal resistance. Thus, higher temperature areas on surface indicate the location of the internal defect. In contrast, in transmission mode, defects are located by measuring the lower temperature area on the opposite surface of the specimen, as the heat travels in all directions and dissipates at the discontinuity [81].

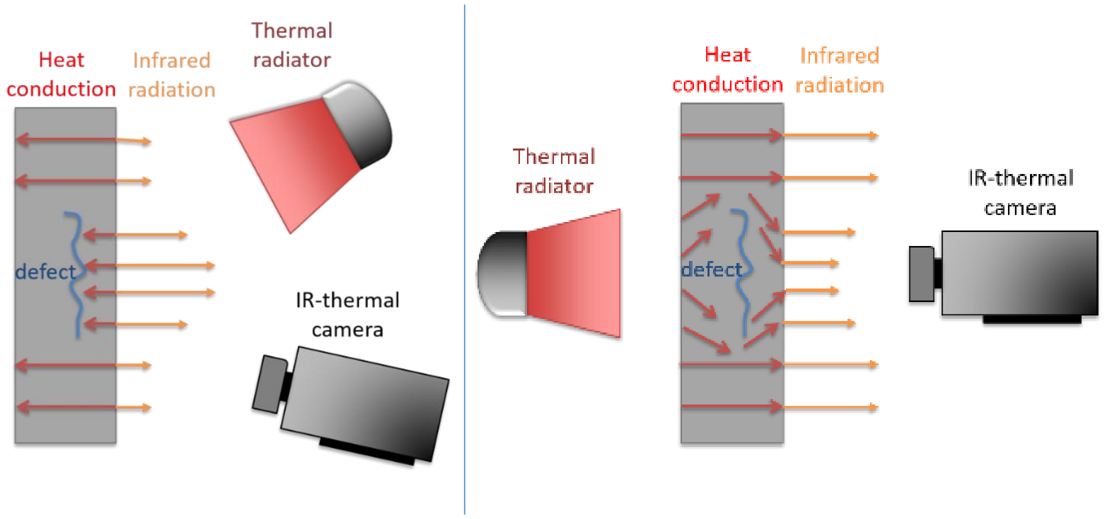

Figure 2.3 Schematic of the active thermographic NDT: reflection mode (left) and transmission mode (right).

### 2.4.4 Application of Thermography Detection

In recent years, with the development of thermal IR cameras, thermographic NDT has attracted much attention in the fields of art diagnostics [96], aerospace [81], military equipment [89], clinical palpation [97], building diagnostics [98], and so on. Due to the benefits of reduced time, non-contact detection, large-area inspection and real-time monitoring, which are listed in Table 2.1, thermographic NDT is recommended for the detection of defects in electrical and mechanical systems. Since the 1990s, thermographic NDT has been used in the study of heat conductivity in solids due to the fast development of thermal cameras [90, 91]. However, there is little research that uses active transient thermography for internal defect detection in multilayer-structured MEMS devices.

In some studies, passive thermographic NDT was used for the thermal characterization of thermally actuated MEMS, for example, to examine the temperature distribution on the surface of thermally actuated MEMS (by Fürjes in 2006 [105] and Serio in 2005 [106]). In 2008, Ishchuk carried out a three-dimensional simulation to examine the problem of heat conduction in a semi-bound isotropic body (15 mm thick) with a defect (80 mm diameter) when it is heated by pulsed thermal radiation and cooled due to convective heat transfer to the surroundings. The situation was considered by examining the nonstationary heat conduction problem when an artificial defect was present, and the solution was obtained by the method of finite differences [88]. In 2012, Suszyński proposed using reflection IR thermographic NDT to detect delamination in a structure composed of a silicon layer (0.4 mm thick), a transitional layer (a eutectic of silicon and aluminium) and a molybdenum base (1.5 mm thick). In the experiment, an aluminium disk (55 mm in diameter and 2 mm in thickness) with milled circular cavities (5-10 mm in diameter) on the side opposite to the excited surface was used as the specimen. The depth of the cavities to the exciting surface ranged from 1 mm to 1.5 mm. A sequence of contrast thermograms were converted into a correlation image using a linear correlation function to enhance the detection of the structure [94].

In 2013, the detection of very thin defects, such as delamination and incomplete bonding of multilayer composite materials, based on carbon fibres was performed by Swiderski. The composite materials are often used for ballistic covers in military. In Swiderski's experiment, four discs of various diameters (1 to 8 mm), made of 0.1-mm thick Teflon film, simulating delamination defects (0.6 mm depth) were introduced into a 1 mm thick specimen. Thermal stimulations of the samples using optical and ultrasonic pulses were compared. The results showed that the signal-to-noise ratio in the ultrasonic stimulation was higher, but no small-area defects were detected in the ultrasonic stimulation [89].

In 2014, thermographic NDT was applied to characterize the surface uniformity of solar cells and LEDs, which are typically made of conductive and semi-conductive thin films. In Leppänen's experiment, a 125 nm-thick indium tin oxide (ITO) film was chosen as the example material. The film was first covered by several poly(3,4-ethylenedioxy-thiophene):poly(styrene sulfonate) (PEDOT:PSS) films, with total thicknesses varied between 16-44 nm, and then bent with a 25 mm cylinder to generate breakages. The result showed that the thermography method provided obvious benefits for measuring the uniformity of multilayer thin films [92].

Since the 2000s, the thermographic NDT method has been considered for the detection of MEMS and microelectronic devices. This method is mainly used for the thermal characterization of thermally actuated MEMS devices and for measuring the surface roughness of LEDs and solar panels and not for the detection of internal defects in devices. The detection of subsurface defects (in tens of millimetres) in some specific materials that can be used in MEMS has been studied.

### 2.4.5 Research of Infrared Thermographic NDT

The development of thermographic NDT is limited by the resolution, number of frames per second and the noise equivalent temperature difference (NETD) of available thermal cameras. Moreover, a suitable excitation method for the specific test case is necessary because it is impossible to find an excitation applicable to all cases; for instance, an unsuitable exciter, such as a laser pulse at a certain wavelength, may penetrate through or burn the specimen [94]. Several solutions have been examined to resolve these problems, such as improving the resolution of the thermal camera or increasing the detectability of the specimen (such as by enhancing the surface temperature difference of the defect and non-defect areas). Analysing the thermal characterization of the object during transient thermographic NDT and improving the detection process based on thermal characterization are two methods to increase the detectability. The definition of detectability commonly used in studies in reflection mode is given in Equation (2.1). $T_{def}$ refers to the surface temperature over the defect centre, and $T_{soa}$ refers to the surface temperature over a defect-free area [107].

$$\text{Detectability} = \frac{T_{def}(t) - T_{def}(0)}{T_{soa}(t) - T_{soa}(0)} \qquad (2.1)$$

In contrast to the detectability in reflection mode, the reflection detectability equation is not suitable for transmission mode. The specimen in transmission mode is heated at the bottom surface, and the temperature of the bottom surface ($T_b$) is proportional to the heat amount, especially when the specimen is heated at constant temperature. If the increase in the top surface temperature is used as the denominator in Equation (2.1), a smaller answer implies better detectability in transmission mode. Therefore, the detectability equation in transmission mode in this thesis should be written as follows:

$$\text{Detectability} = 1 - \frac{T_{def}(t) - T_{def}(0)}{T_{soa}(t) - T_{soa}(0)} \qquad (2.\ 2)$$

Because the initial surface temperature over the defect and sound areas are the same, $T_{def}(0) = T_{soa}(0)$ , the detectability determines the thermal contrast from the surrounding environment over time. This parameter can be termed the relative detectability, and its equation can be written as:

$$\text{Detectability} = \frac{(T_{soa}(t) - T_{soa}(0)) - \left(T_{def}(t) - T_{def}(0)\right)}{T_{soa}(t) - T_{soa}(0)} = \frac{T_{soa}(t) - T_{def}(t)}{T_{soa}(t) - T_{soa}(0)} \qquad (2.\ 3)$$

During heating, the temperature of the surface over the sound area increases over time. The internal defect will hinder the surface over the defect from heating by imparting thermal resistance. Therefore, the top surface temperature over the defect ($T_{def}(t)$) is lower than that of the sound area ($T_{soa}(t)$). The temperature difference between the defect and sound areas ($T_{soa}(t) - T_{def}(t)$) increases from zero to its maximum value and then drops gradually. In addition, at the beginning of heating, the temperature of the top surface ($T_{soa}(t)$) is approximately above the initial surface temperature ($T_{soa}(0)$). The change in the temperature of the sound area ( $T_{soa}(t) - T_{soa}(0)$ ) increases gradually until it approximates the change in the heating temperature ($\Delta T = T_b(t) - T_b(0)$ ). Therefore, the temperature difference ( $T_{soa}(t) - T_{def}(t)$ ) and increment surface temperature ($T_{soa}(t) - T_{soa}(0)$) are both close to zero when t is very small.

The value obtained by Equation (2.3) at the beginning of heating is only slightly smaller than 1, which indicates good detectability. However, the temperature difference $(T_{soa}(t) - T_{def}(t))$ is a more important study factor when the heating temperature increment is constant. Therefore, in this thesis, the value obtained from Equation (2.3) is termed the relative detectability and is used as a reference. The temperature difference, top surface temperature increment and bottom surface temperature increment are examined in the detectability assessment.

Previously, a finite difference 3D model of a semi-infinite isotropic plate of a specific material with a subsurface defect was used to determine the surface temperature distribution using an active approach (by Maldague [107]). This simplified the complex problem corresponding to a one-dimensional case. The author drew important conclusions from the simulation results: the surface temperature difference was smaller than that of the defect surface, and the surface temperature difference reached a maximum value at a specific time. He also mentioned using the maximum temperature gradient to locate the edge of the defect but provided no analytical explanation for this phenomenon.

Additionally, Connolly used a finite element model to examine the influence of some parameters on the detectability of defects in thermographic reflection NDT. The simulation results showed that a major factor influencing the detectability was the depth of the defect beneath the surface, where an increased depth resulted in a decrease in the detectability. A model of a low-diffusivity coating on a high-diffusivity substrate was shown to achieve good results. The analysis also showed the influence of the pulse duration on the defect detectability, where reduced heating times can maximize the defect detectability in any particular application [93]. However, these results only outlined the influence of various factors on the detectability, and no mathematical relationship between the detectability and influencing factors were provided.

To increase the detectability and reduce the noise influence during detection, several methods have been developed for thermographic NDT. For instance, a method that numerically interpolated a thermal parameter, i.e., the difference between the maximal and minimal temperature on the sample surface, was demonstrated by Tomić in 2013 to overcome shortcomings when the maximum temperature difference of the defect occurs between frames [101].

Polynomial solutions of the inverse heat conduction problem were proposed by Borazjani in 2014 to predetermine the frequencies of boundary excitation to detect defects in composite and multilayer materials with lock-in thermography NDT [99]. This detection technique depends on several internal factors, such as the thermal conductivity, heat capacity, and especially, the defect depth. For modulation frequencies inside the predicted detection range, thermal images present a clear pattern at defect-free sites; conversely, thermal images of the defect are blurred.

Vavilov obtained a sequence of images by dynamic thermal tomography (DTT) to detect the defect depth, as the deeper material layers are characterized by longer time delays of the thermal response. In a thermal image sequence of an arbitrary length, the maximum temperature and the time at which each pixel appears in the images determines the ideal detection time [100].

However, the study of the reflection method requires a thermal camera and external heat resource on the same side of the object, which is difficult to achieve for MEMS devices because their size is very small (from 100 μm to 10 mm), while the focus length of the microlens of a thermal camera ranges from 10 mm to 30 mm and the diameter of the microlens is often tens of millimetres. Because the microlens is required to be perpendicular to the surface of the object (limiting the distance between the object surface and the lens and reducing the quality of the IR image), there is no room for the excitation source. Transmission mode is more convenient for the thermographic NDT of small devices.

## 2.5 Current Challenges and Thesis Tasks

The use of external active thermography NDT in the detection of a defect in MEMS or microelectronic devices has been rarely studied because a microlens is required for the detection of microsized defects. The diameter of a microlens is often larger than 20 cm, and its focus length is smaller than 20 mm. Thus, it is difficult to find a place for the heating equipment in such a small space. In addition, considering the low working temperature required for the thermal detector, a very close heat source may reduce the measurement accuracy. There, in this thesis, the detection of MEMS devices is carried out in transmission mode. Most multilayer thin-film devices on silicon or gallium arsenide substrates are thinner than 1000 mm. Therefore, the devices can be heated from the bottom very quickly. The transmission thermographic detection of micro defects in a multilayer structure will be discussed in detail in Chapter 4.

Furthermore, for specimens with a defect, few analytical methods examining thermal diffusion and heat transfer, as well as edge effects of the defect on heat transfer, have been examined using transmission mode, possibly due to the complex calculations involved in the 3D mathematical model, which is best dealt with using numerical modelling techniques. Until now, research based on analytical methods in reflection-mode thermography has considered thermal diffusion from the surface to the delamination interface as a one-dimensional problem. When a heating pulse of energy $J_0$ is applied at the surface of a semi-infinite half space, the response temperature distribution of the solid is given by [108]:

$$T(x,t) = \frac{J_0}{\sqrt{\pi \rho c k t}} \cdot e^{\frac{-x^2}{4\alpha t}} \tag{2. 4}$$

where $T(x,t)$ is the temperature increase at depth $x$ below the surface at time t after a uniform pulse of energy $J_0$ on the surface, and $x$=0 at time $t$=0; $\rho$, $c$, $k$, and $\alpha$ are the density, heat capacity, thermal conductivity, and thermal diffusivity, respectively.

According to Almond and Pickering's analytical research [103], because of the reflection at the delamination interface, the centre surface temperature over a defect will be superimposed, and the impulse heating response of such a layer can be obtained from the expression:

$$T(x,t) = \frac{J_0}{\sqrt{\pi\rho ckt}} \cdot \left[1 + 2\sum_{n=1}^{\infty} R^n e^{-\frac{(nd)^2}{\alpha t}}\right] \tag{2. 5}$$

where R is set at 1. Equation (2.5) was obtained from the inverse Laplace function of the thermal response function of a layer of thickness d with a Dirac delta function impulse of magnitude $J_0$, when the diameter of defect D is much larger than d. Therefore, the temperature difference between the centre of the defect and the reference area is obtained from Equations (2.4) and (2.5):

$$T(x,t) = \frac{2J_0}{\sqrt{\pi\rho ckt}} \cdot \left[\sum_{n=1}^{\infty} R^n e^{-\frac{(nd)^2}{\alpha t}}\right] \tag{2. 6}$$

The central hypothesis of Almond and Pickering's research [103] is that a better representation of the difference temperature at the surface over the centre of a circular defect of diameter D at depth d can be written as:

$$T(x,t) = \frac{2J_0}{\sqrt{\pi\rho ckt}} \cdot \left[\sum_{n=1}^{\infty} R^n e^{-\frac{(nd)^2}{\alpha t}}\right]\left(1 - e^{-\frac{\left({}^{D}/_{2}\right)^2}{4\alpha t}}\right) \tag{2. 7}$$

They subjectively assumed that the defect edge acts as a heat sink, sweeping away heat ($\propto e^{-\frac{\left({}^{D}/_{2}\right)^2}{4\alpha t}}$) reaching the edge at the defect tip, at a distance of D/2.

In contrast to the reflection method, transient thermography has a different heat transfer route, which is much longer than that of the reflection method, as mentioned in section 2.4. The temperature distribution from the bottom to the sound surface and the surface over a defect centre represent two heat transfer routes. The extra route will affect the temperature of the sound and defect-centre surfaces. The temperature distribution within a semi-infinite solid heated through the surface to $T_{bottom}$ has the following relationship with the thermal diffusivity and heating time [127]:

$$\frac{T(x,t)-T_{bottom}}{T_{ext}-T_{bottom}} = erf(\frac{x}{2\sqrt{\alpha t}}) \tag{2. 8}$$

where x is the distance from the bottom surface. When $\frac{x}{2\sqrt{\alpha t}}$ is much smaller than 1, the error function, erf, is approximately linear. Therefore, a relationship may exist between the extra route and the temperature difference. Further details of the analytical calculation of the transient thermography will be investigated in Chapter 4.

Furthermore, the thermographic detection is also influenced by the detecting equipment. The spatial resolution of the IR camera is limited by the IR wavelength (λ), which is longer than 760 nm. When the defect size the same order of magnitude as the wavelength, diffraction limits the spatial resolution. The pixel resolution limit is referred to as Rayleigh's criteria and is given by [128]:

$$\varepsilon = 0.61\frac{\lambda}{NA} \tag{2. 9}$$

where NA is number aperture of the optical detection system.

The temperature resolution is mainly limited by the number of bits of the analogue-to-digital converter (ADC) [128]. For example, the resolution of an 8-bit ADC can encode an analogue input in 256 different levels ($2^8$=256). If the temperature range is from 0 °C to 200 °C, the temperature resolution of an 8-bit ADC is 200 °C/256=0.8 °C/bit. In the same way, the temperature resolution of a 10-bit ADC is 200 °C/1024=0.2 °C/bit. Meanwhile, the signal-to-noise ratio (SNR) is a measurement of the signal strength relative to the background noise ($SNR_{dB}=10\ \log_{10}(A_{signal}/A_{noise})$) [128]. The SNR of a general IR camera is larger than 48 dB. If the temperature difference is larger than 10 °C, the noise of a 10-bit ADC is smaller than 0.2 °C. Therefore, $20\ \log_{10}(10/0.2)=34$ dB <

48 dB.

However, this thesis focuses on the surface temperature response to different heat excitations and the temperature distribution in the specimen during heating. The relative temperature difference is the critical parameter, rather than the actual temperature. The choice to use an IR camera in the experiment depends on the achievable temperature difference and the defect size. The requirement of a thermal camera can be discussed in future work.

In conclusion, the use of transient transmission thermography NDT to locate and measure internal defects in multilayer MEMS devices has been seldom reported. Therefore, in this thesis, the common NDT detection of a MEMS device is compared with a simple thermographic NDT test. Then, the possibility and challenges of using thermographic NDT for the detection of MEMS devices will be discussed in Chapter 3. A model of a multilayer structure with an internal defect was developed based on the discussion, and factors such as the size effect of specific materials commonly used in MEMS devices, the thermal mechanism of defects and the calculation of applied heating energy and duration were studied analytically.

The simulation results with various materials were used to determine the relationship between the detectability and various parameters, such as the thermal characteristics of the material, the heating method and so on. The challenge discussed in this thesis is to analyse the heat diffusion path in transmission mode for systems with various defect sizes and depths. Finally, specimens with a relevant multilayer structure and artificial defects were tested by thermographic NDT to improve the simulation results.

# Chapter 3 A Comparison of Destructive and Non-Destructive Defect Detection Methods for MEMS Devices

This chapter describes destructive and non-destructive detection methods that have been applied to MEMS-based DC switches. First, a standard thermal shock test was applied to generate the defective, multilayer structure of the switches. Then, the tested specimens were sectioned and studied using both a destructive method, i.e., focused ion beam (FIB) combined with scanning electron microscopy (SEM), and non-destructive methods, i.e., optical 3D measurement systems and focal X-ray tomography. This study aims to compare the abilities of the detection methods to examine crack propagation within the multilayer structure of the switches.

## 3.1 Introduction to the Electrothermal MEMS DC Switch

### 3.1.1 Structures and Operation Principal of the Electrothermal DC switch

The specimens used in this case study were supplied by MEMSCAP DC Switches, as used in the Polynoe program [110]. This type of switch is an electrothermal switch driven by Joule heating. As shown in Figure 3.1, two arms (marked in colour) comprise a switch, and each arm consists of two parts: two active beams (red) and one passive beam (green). The beam is fixed to the silicon substrate at one end and is suspended above the substrate. The beam on the left side is termed as the latching actuator, while the beam on the right side, which has a longer latch, is termed as the contact actuator. The switch is fabricated in the open mode, as shown in Figure 3.2 (a), and the tips of the arms are separated when open. Figure 3.2 (b) shows the closed state of the switch, where the tips are in contact and latched. Once contact is made between the two arms, an electrical signal can pass through the switch.

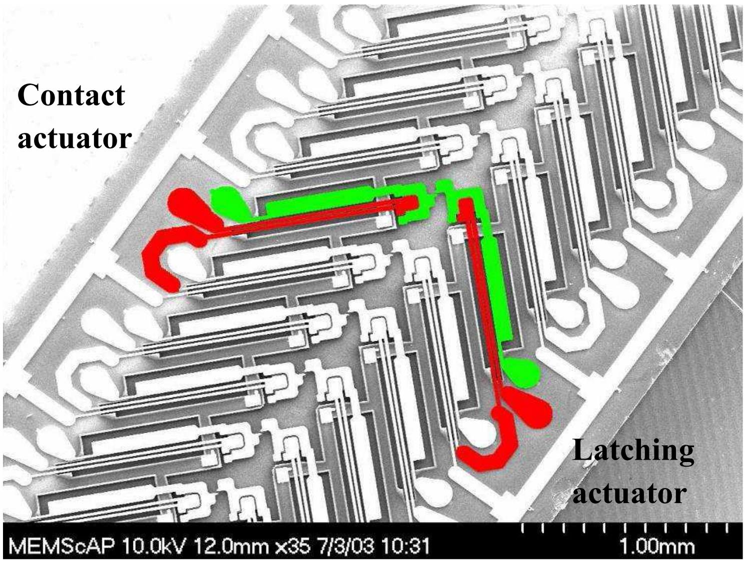

Figure 3.1 MEMSCAP DC Switch matrix [110].

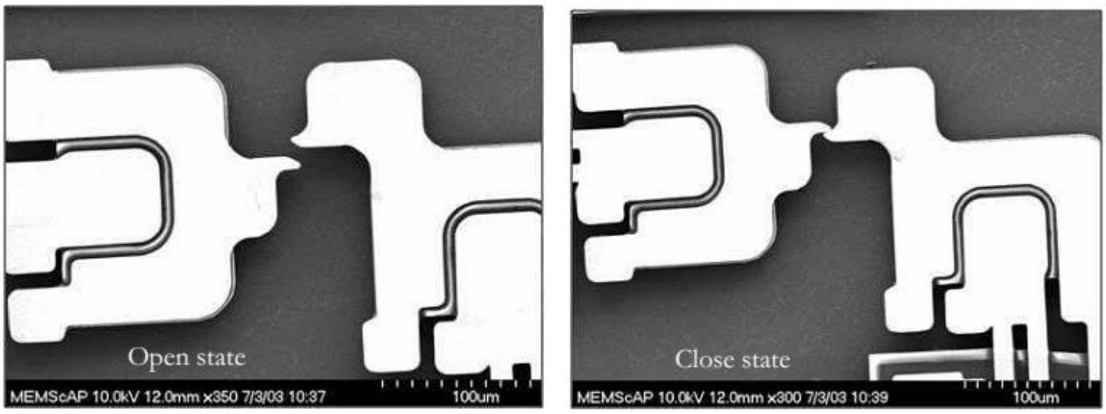

(a) (b)

Figure 3.2 Switch in the open (left) and closed (right) state [110].

Figure 3.3 presents the structure and driving principle for one of the switch arms. The active beams are mechanically connected to the passive beam by a dielectric tether so that the control electrical current will only flow through the active beams, providing heating. This temperature increase results in the elongation of the beams, while the unheated passive beam without heating is unaffected. Therefore, the tip is deflected by the thermal extension. Figure 3.4 reveals the latching sequence as follows. In the fabricated position, the switch is open. In the first step of the closing sequence, the latching arm is actuated to move in the direction of the arrow (1). Then, the contact actuator is also actuated (2). After that, the latching actuator is switched off (3), and finally the contact actuator moves back (4). There is a small latch on the contact tips, which is used to lock the two switch beams when the switch is in the ON position without electrical current, as shown in Figure 3.1.

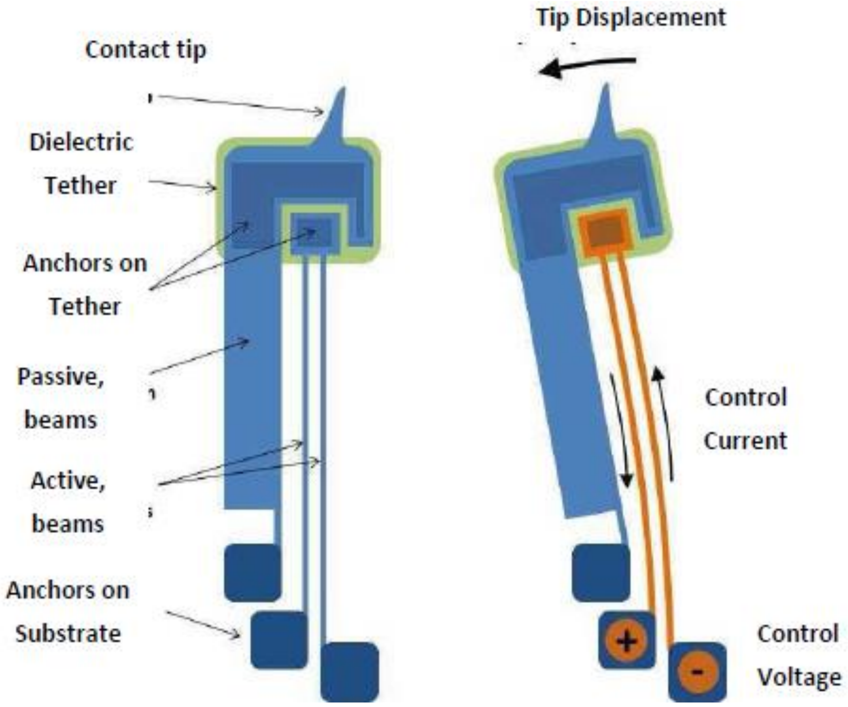

Figure 3.3 Schematic diagram of the working principle of a switch arm [110].

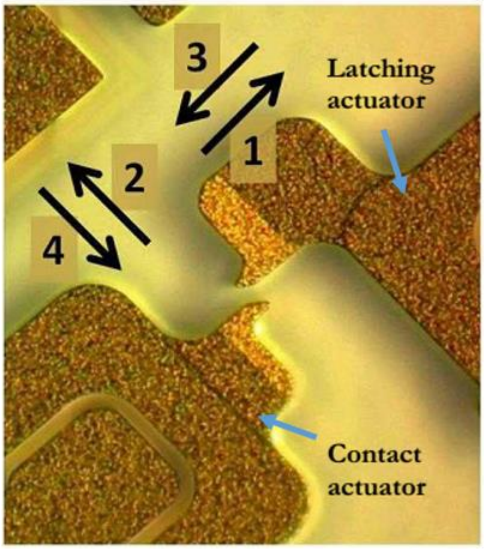

Figure 3.4 Latching sequence of the DC switch.

## 3.1.2 Construction of the Electrothermal DC Switch

A cross section of a switch constructed from layers of several materials is shown in Figure 3.5. First, 20 µm of nickel was electroplated to form the moving arms on an n-type (100) silicon substrate, and a 0.5 µm gold layer was plated on top of the nickel to provide a suitable pad for bonding wires leading to external electrical connections. The combination of 20 µm of electroplated nickel and 0.5 µm of gold (sidewall metal) forms the metal beams. The seed layers and electrical isolation layers between the metal film and the substrate include a 2 µm silicon oxide layer, a 0.7 µm polysilicon film, a 0.35 µm low-stress silicon nitride layer, a thin layer of Cr and Pt (anchor metal) and a 500 nm Cu layer protected with a thin Ti layer. The pattern for the metal anchor was produced by chemical wet etching using a sacrificial oxide layer. Finally, a wet etch of silicon was used to form a 25 µm-deep trench in the silicon substrate.

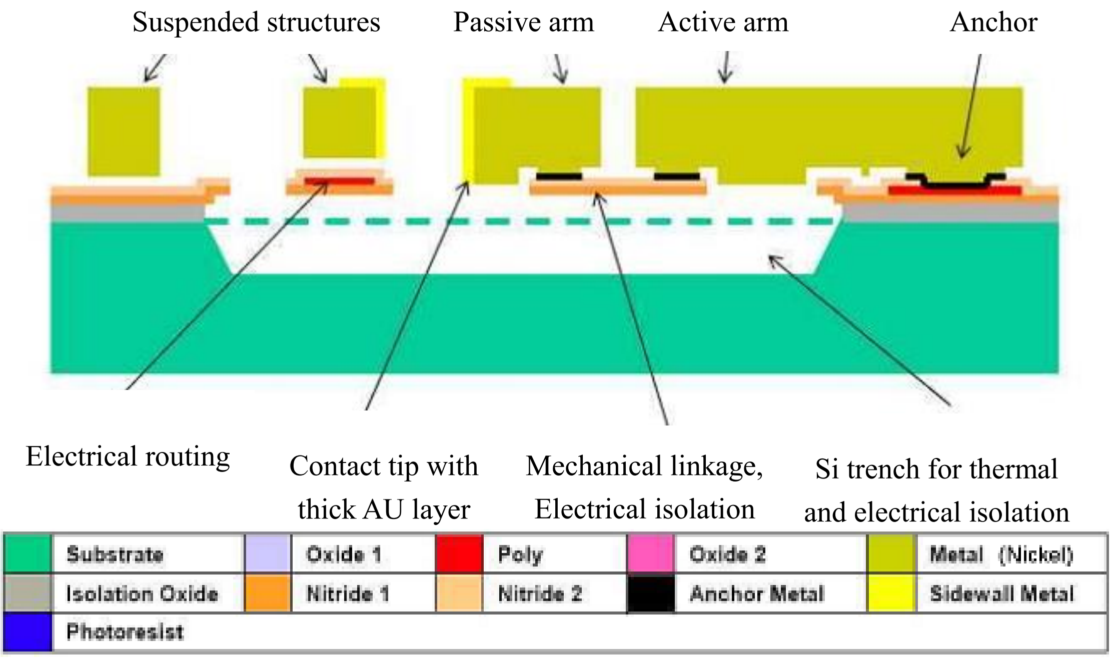

Figure 3.5 Side view of the DC switch and corresponding material layers [110].

## 3.1.3 Characteristics of the Electrothermal DC Switch

Because of the latch, the switch consumes no power in either the ON or OFF position.

Thus, there are two operation states of this thermal actuator:

Actuating: When the switch is opening or closing, the electrical single passes through the passive beam, which is isolated from the active beams. The temperature increase caused by Joule heating elongates the hot beams. Due to the dielectric tether, the cold beam endures a shearing force on the tip and bends. During this bending process, only a mechanical load is applied to the passive beam, while both mechanical and thermomechanical loads occur in the heated beams.

Working: Once the switch is in the ON position, all three beam positions are fixed by the latch on the tip of the contacts, and any signal current passes through the passive beam. Thus, the beams are forced in this stable condition by the restoring force from the opposite beams. No power consumption is required for maintaining the switch in the ON position.

Compared with alternatives, such as electrostatic switches, this type of DC switch offers many advantages, including low on-state contact resistance, high open-state voltage isolation and reduced risk of stiction. These advantages result from the following:

(a) The high contact force when the switch is latched.

Large deformations in the nickel beams when the device is in the ON position results in a high elastic restoring force. This high force produced by the beams is resisted by the small contact tips and therefore causes a high contact pressure. Due to the latching design, the beams will remain in this stable position until the latch is unlocked.

(b) Large open gap between the beams when switch is in the OFF position.

In the OFF position, the switch beams are separated by a 12 μm gap. This large open gap ensures a high degree of isolation between the two contacts, ensuring no current flow will occur when the switch is in the OFF position.

However, these switches have some disadvantages. Because the thermal actuating speed is on the order of milliseconds and thus is slower than that of electrostatic relays [110], these switches cannot achieve high cycle frequency. Due to the high contact force, high electrical current, ON/OFF frequency and high-temperature working environment, several failure modes have been identified: a reduction in the contact force leading to an increase in the contact resistance [111, 112], contact welding, arcing contact, reduction in the open resistance, and contact erosion [113, 114].

### 3.1.4 Failure Mechanisms of the Electrothermal DC Switch

The failure mechanisms of the electrothermal DC switch are as follows:

- **Contact force reduction**: low-frequency cycling leads to long loading times and sustained pressure. Thus, long-time and high-strain applications result in creep deformation [115]. The elastic force between the beams decreases due to the accumulation of deformation.
- **Contact resistance increase**: a reduction in the contact force and wear of the tips at the contact area decrease the contact surface.
- **Open resistance reduction**: switch short circuit. In Figure 3.6, the open gap between the two contact tips is approximately 10 µm. If the beams are deformed enough, the size of the open gap will be reduced until the two tips make contact in the OFF state, or an electrical arc may occur when open gap is too small.
- **Interface delamination**: fatigue induced by the long-term cycling of structures with mismatched coefficients of thermal expansion.

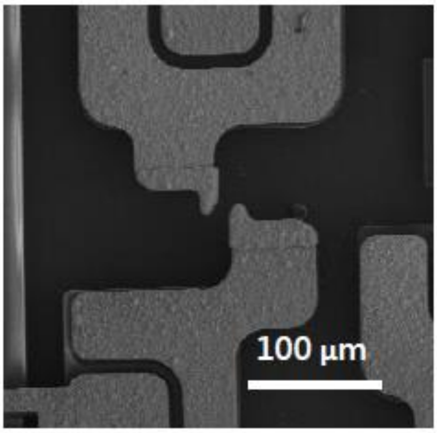

Figure 3.6 SEM image of the contact tips of the switch.

## 3.2 Destructive and Non-destructive Tests of the Electrothermal DC Switch

The MEMS switches were subject to destructive and non-destructive tests, i.e., 3D micro-focal X-ray scans and optical metrology measurements, along with the thermal shock tests. The non-destructive tests were performed both before and after the thermal shock experiments to evaluate the internal structure of the devices and internal defects. Because of the limited number of devices, only one device was tested by the destructive test.

### 3.2.1 Thermal Shock Test for Artificial Defects

Thermal shock testing accelerates device failure caused by temperature cycling or thermal shock during normal use by exposing a sample to alternating low and high temperatures. In this work, to create artificial defects in the MEMS devices, the high- and low-temperature levels were maintained at 150 °C and -50 °C (as shown in Figure 3.7), respectively, according to the reliability specification of the DC switch [121]. To achieve thermal shock, two separate environmental chambers at the high- and low-temperature levels were used, and the tested samples were then manually transferred between the chambers over 5 test cycles. The temperature transitions were under 5 min.

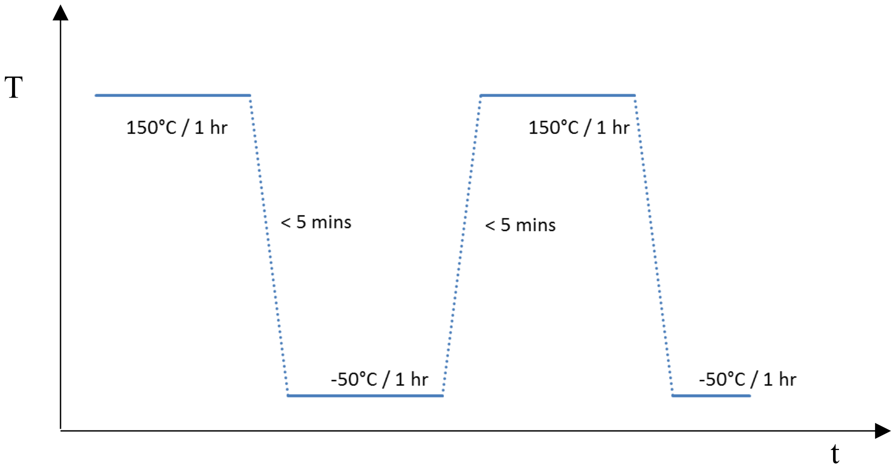

Figure 3.7 Temperature profile for the thermal shock test.

### 3.2.2 Optical Surface Analysis

An optical 3D surface measurement and characterization system (Alicona InfiniteFocus) was used to study the surface geometry of the DC MEMS switches. The vertical and lateral resolution are dependent on the size and structure of the object under studied, which determines the selected objective lens. According to a measurement report published by Alicona [119], when a 5× objective is used, the measurement pixel size is 1.76 μm × 1.76 μm, and 410 nm vertical resolutions and 2.2 μm lateral resolutions can be achieved.

A corner of the switch imaged by the 5× objective is shown in Figure 3.8. The dark areas in the image represent regions with missing data because optical microscopy functions through light signals reflected from the surface of the specimen. If the depth of the trench is too large and the width is too small, light is not readily reflected back to the lens. Vertical deformation was studied along paths A, B and C. The black area represents data loss during measurement because the depth of the trench under the cantilever is too large, such that the incoming light beam is not reflected from the bottom.

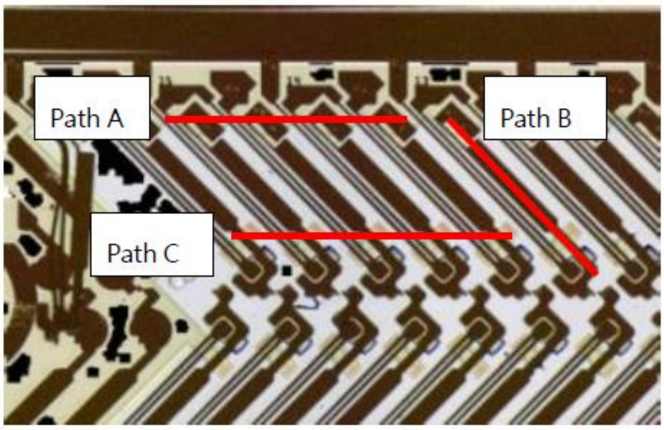

Figure 3.8 Alicona scanning image of DC switch after TCT.

Images of the surface roughness are shown in Figure 3.9. Scanning images of the specimens before and after thermal shock are compared in Figure 3.9 (a) and (b), respectively, to examine the surface morphology of the samples. No obvious change in the surface morphology can be seen from the images after the thermal shock test, except that one of the beams was bent after the test.

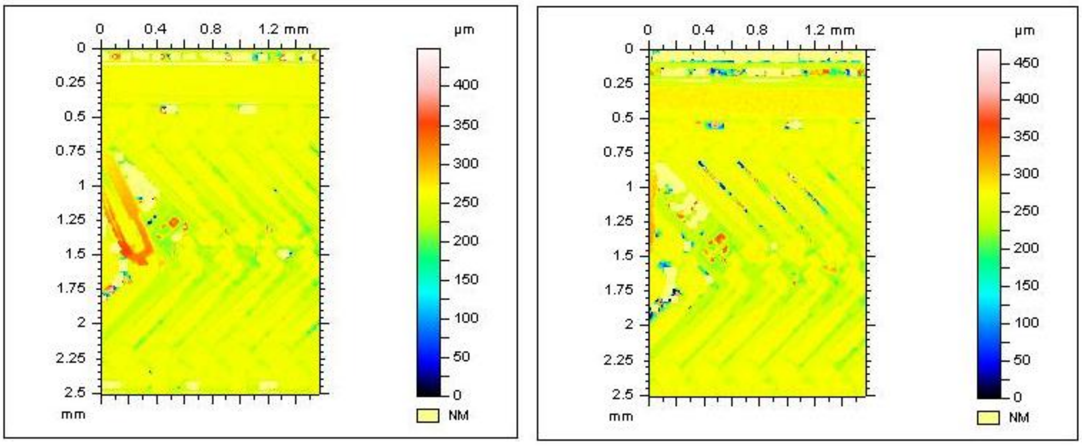

(a) (b)

Figure 3.9 Surface roughness images of the DC switch (a) before and (b) after the thermal shock test.

Because the switch has a very deep trench, the data-loss area will greatly influence the measured roughness parameter. Therefore, in Figure 3.10, a profile was extracted from the surface along path A, where the occurrence of delamination and fracture in the internal structure was predicted. The specimen was fixed on a base during scanning before and after thermal cycling. The profile ran from the end of the 3rd latching actuator to the 11th latching actuator and showed a slight difference before and after thermal treatment. In Figure 3.10, the line marking the fluctuation after thermal treatment is 20 µm larger than that before treatment. In contrast, the displacement along a beam (path B), as shown in Figure 3.11, and the displacement across 5 beams (path C), as shown in Figure 3.12, were less than 10 µm. Thus, the surface investigation of the specimens indicates that after the thermal shock experiment, delamination or fatigue may occur under the nickel film at the anchors. Internal defects can be revealed from the surface observation. However, this detection result cannot be easily repeated. The surface deformation may be caused by interface delamination, but the cause of the fluctuation may be more complex. Optical microscopy can be used for the detection of internal damage. However, the detection result is not enough to prove the occurrence of damage.

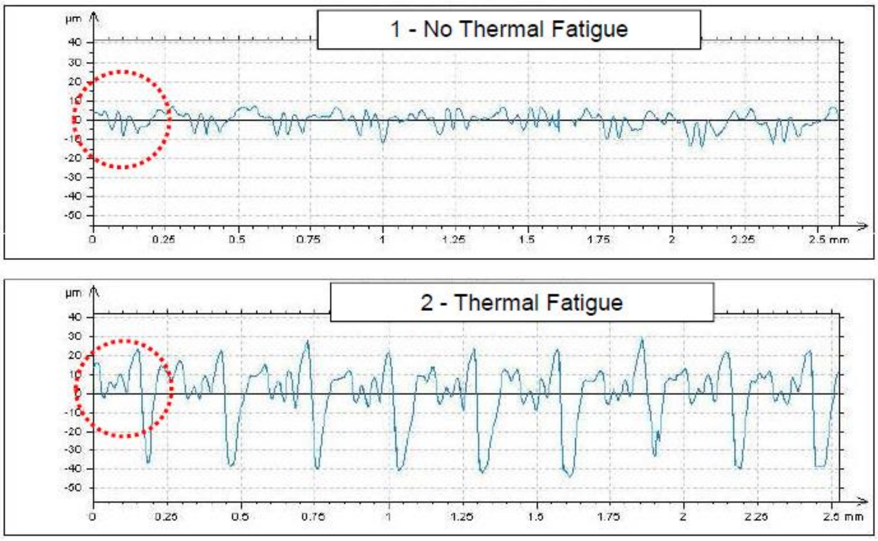

Figure 3.10 Profiles of the extraction line roughness along path A before and after the thermal shock test.

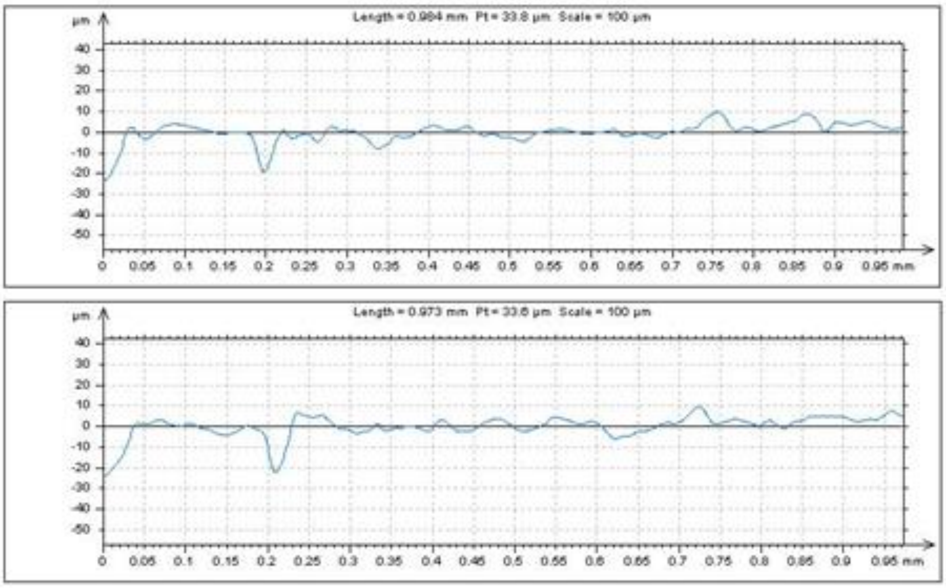

Figure 3.11 Profiles of the extraction line roughness along path B before and after the thermal shock test.

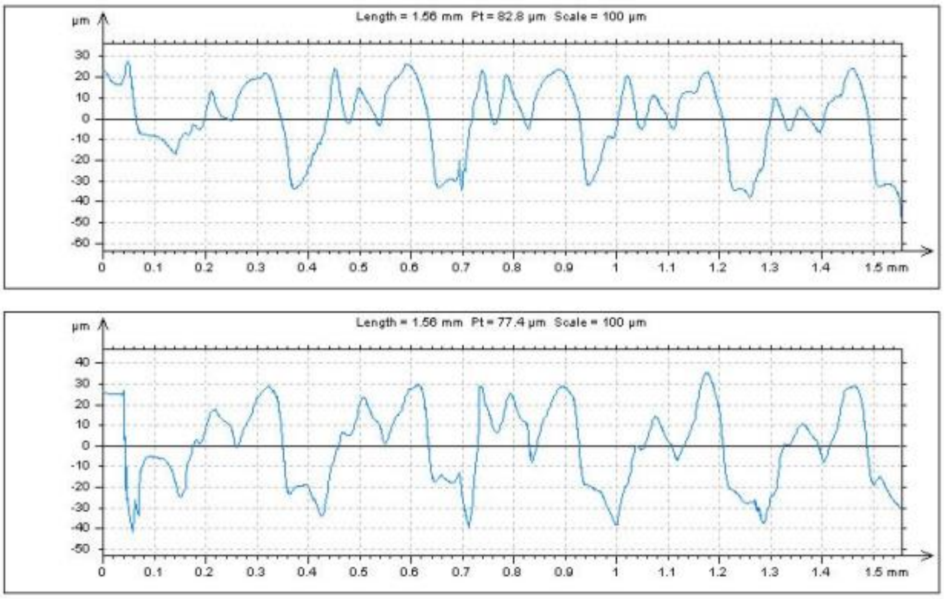

Figure 3.12 Profiles of the extraction line roughness along path C before and after the thermal shock test.

### 3.2.3 X-ray and Computed Tomography

X-ray CT is a common non-destructive method for the detection of internal defects in structures, which uses multiple computer-processed X-rays to produce tomographic images of specific areas of a scanned object. The specimen was scanned by a MHX160 X-ray CT scanner [123], and each scan took more than 4 hours to complete.

Figure 3.13 shows the 2D X-ray image of the MEMS structure using the maximum imaging resolution (0.68 μm) of the MHX160 X-ray CT scanner. From this X-ray scan study, based on the achievable resolution, no internal defects were observed in the manufactured MEMS structure. Figure 3.14 shows the 3D image of part of the specimen, in which the white regions represent the metal materials and the black regions, which cannot be observed, represent silicon. The mass absorption of X-rays by metal and semiconductor materials are very different [120], making it difficult to focus on both the metal and semiconductor materials at the same time. Thus, delamination between the two different materials is difficult to observe using X-ray detection methods.

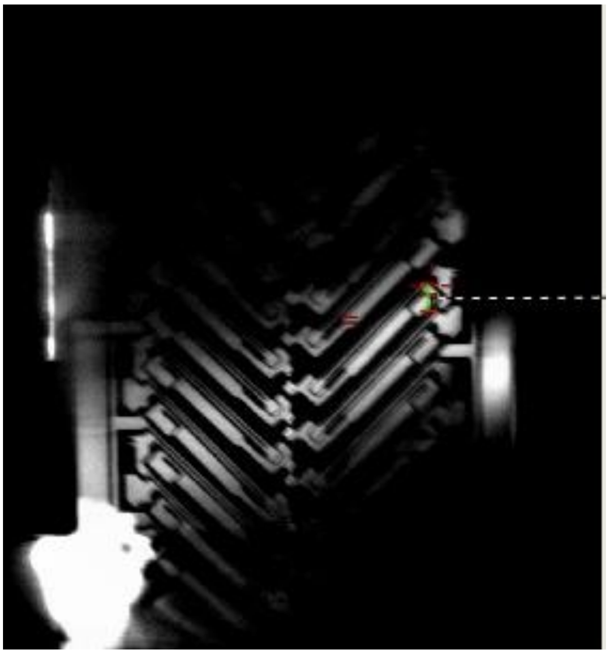

Figure 3.13 X-ray image of the MEMS device.

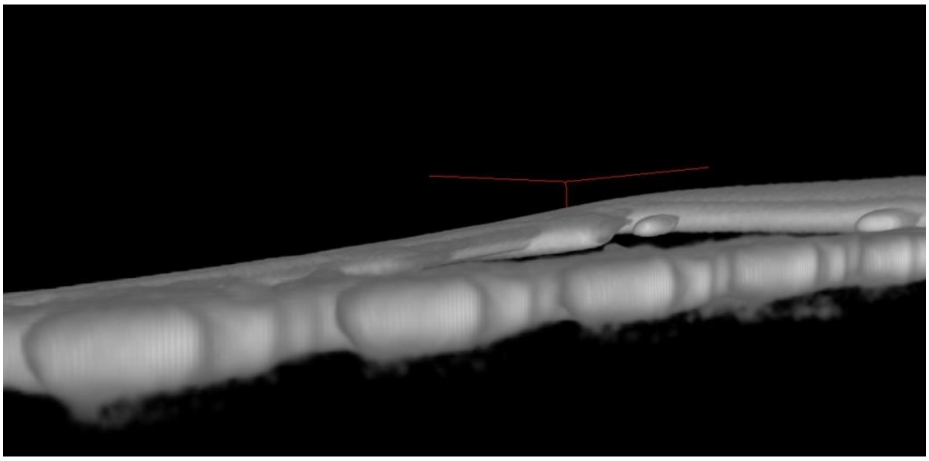

Figure 3.14 3D cross section of the metal film.

### 3.2.4 Thermographic NDT in the Steady State

The thermographic NDT method was also used to examine the DC switch. Figure 3.15 shows an IR image of the DC switch heated from the substrate by a 30 °C hot plate taken by an IR Thermosensorik camera that includes a microlens with a focus length of 22 mm. The speed of the camera is 107 frames per second. The temperature variation in the thermal image is a problem associated with the spatial photoresponse nonuniformity of the IR focal plane arrays (FPAs). The nonuniformity arises because each individual detection element in the FPA exhibits different response characteristics than those of its neighbouring elements [124]. In the image, the outer structure of the device can be clearly seen, but the internal defects are not visible because (1) the overall system is in the steady state, and therefore, the temperature difference between the defect and sound areas is very small, and (2) the pixel resolution is not high enough. Therefore, if we can overcome these two problems, it may be possible to detect internal defects by thermographic NDT.

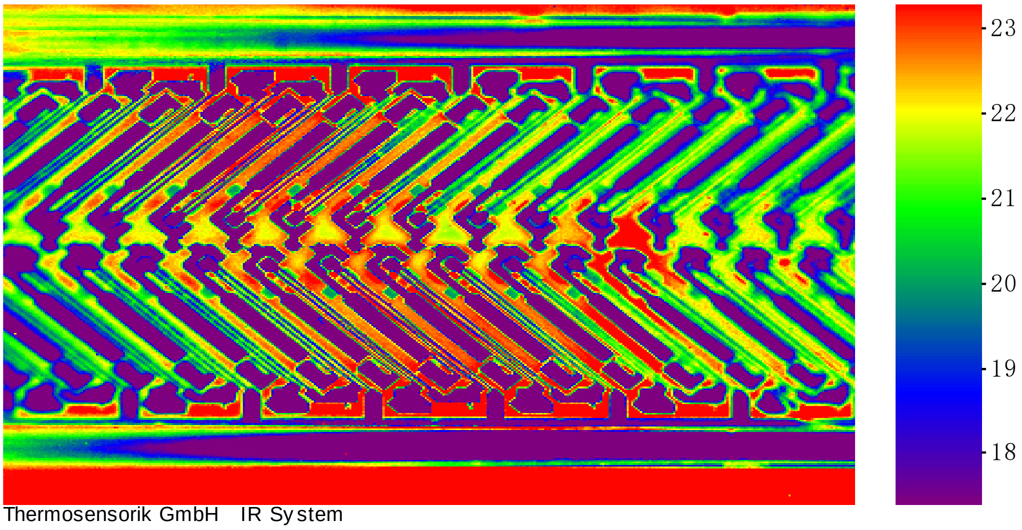

Figure 3.15 IR thermography image of the DC switch.

### 3.2.5 Focused Ion Beam

Previously published simulations of thermal stresses in the multilayer structure of the same type of switch have indicated that interfacial delamination is expected to occur at the anchors of the beams [125]. To study the internal structure of the device after the thermal shock test, a dual-beam FIB system, which is a combination of FIB and SEM, was employed [122]. Both the anchors on the tether and the anchors on the substrate of the switch beams (as shown in the schematic diagram in Figure 3.3) that underwent thermal shock testing were used to locate any interfacial delamination. Because the interface of the switch is 20 μm under the nickel film, 10 μm wide and 30 μm deep notches were micro-milled by FIB into these anchors, as shown in Figures 3.16 and 3.17. All of these regions consist of a multilayered structure, and thus, the occurrence of an interfacial defect was predicted.

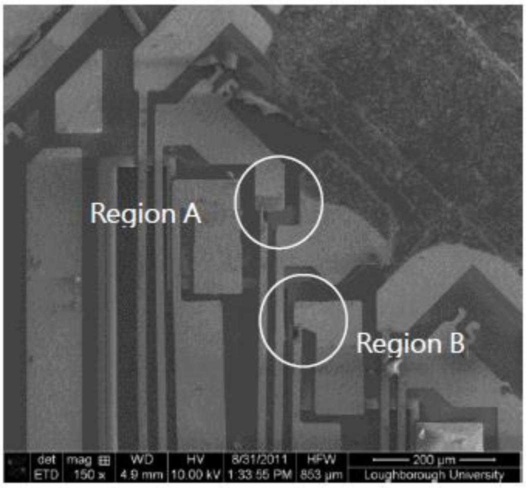

Figure 3.16 SEM image of the end region of the MEMS device studied using the FIB technique.

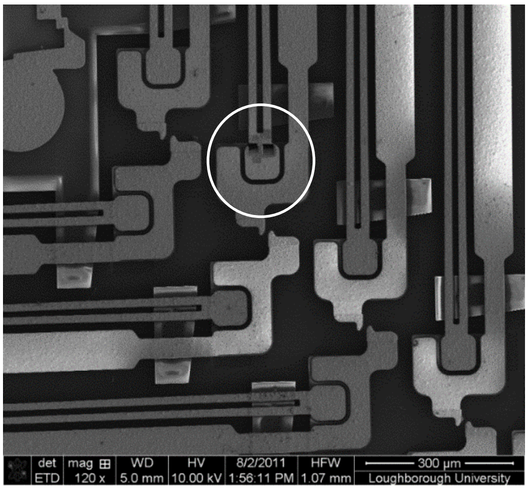

Figure 3.17 SEM image of the tip region of the MEMS device studied using the FIB technique.

After the FIB milling, microscope analysis using SEM revealed interfacial cracks approximately 25 µm below the surface at the anchors on the substrate, as shown in the SEM images of milled regions A and B (Figures 3.18 and 3.19). This observation confirms the occurrence of delamination between the nickel and silicon layers of the structure. In contrast, the SEM image of the milled regions of an anchor on the tether shows no obvious delamination after the thermal shock test (Figure 3.20), which indicates that no damage occurred because the anchors on the tether are not fixed on the substrate.

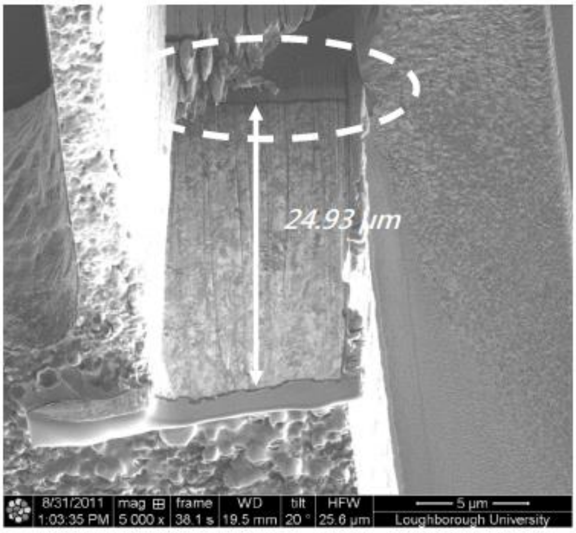

Figure 3.18 SEM image of milled region A.

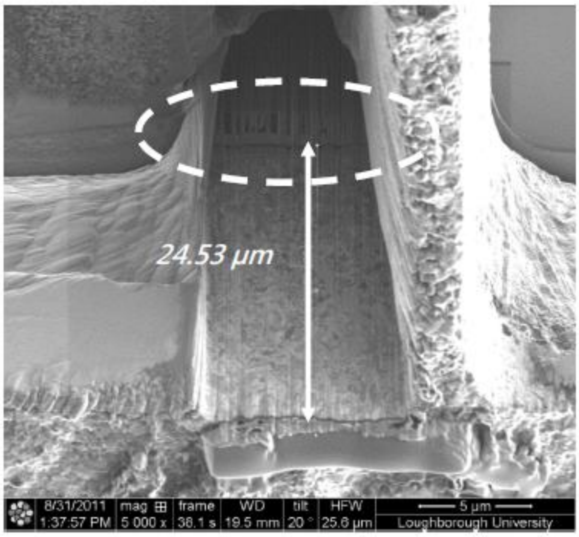

Figure 3.19 SEM image of milled region B.

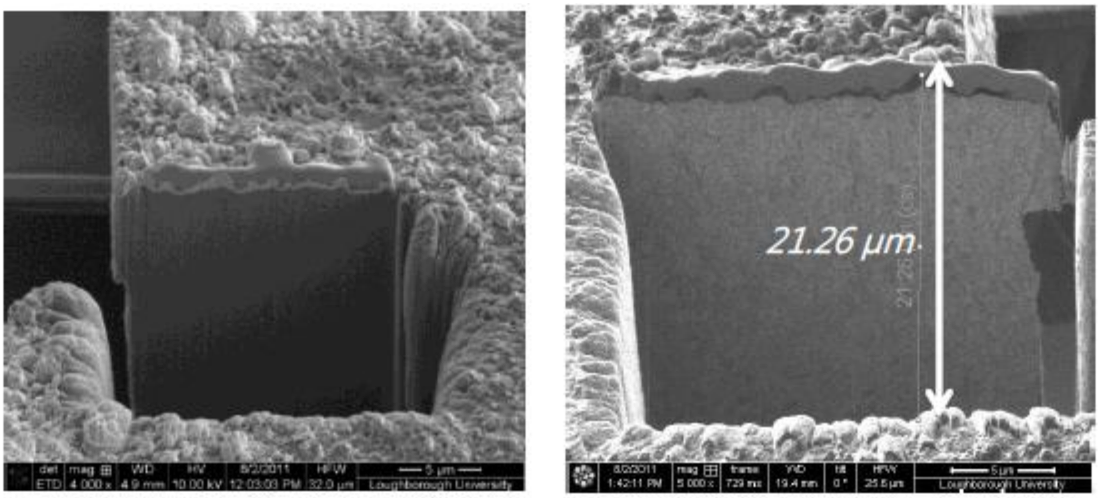

Figure 3.20 SEM images of the milled tip anchor.

Delamination was observed in the SEM images, but the extent of delamination in the anchors cannot be confirmed. The cross section was examined by X-ray diffraction (XRD) to determine the exact position of the crack. Results from the area around the crack indicate that the top and bottom layers are both made of nickel. However, according to the manufacturing process of this micro switch and the thermal failure loading simulation of A. R. Maligno [125], a very thin copper layer may be overlooked when the ion beam reaches the far end of the investigated notches.

## 3.3 Summary

Interfacial delamination is one of the failure modes of MEMS DC switches. Compared with other detection methods, focus X-ray CT was shown to be a poor choice for the detection of delamination between two materials with different X-ray absorption coefficients. Meanwhile, the FIB technique, a destructive detection method, requires a long time to micro-mill the specimen, making this method a slow and expensive process. In contrast, thermography is quick and is also a non-destructive detection method. An IR image of a specimen in steady state cannot be used to observe internal defects due to the poor pixel resolution and small temperature difference. Thus, in the following study, we discuss the thermal behaviour of the multilayer structure of MEMS devices to investigate the feasibility and detectability of transient thermographic NDT.

# Chapter 4 A Study of the Thermal Behaviour of Thin Multilayer Films Containing Micro Defects

## 4.1 Introduction

This chapter will discuss the thermal behaviour of layered/multilayer structures where the thicknesses of the layers are on the order of micrometres, as well as the effect of defects within the structure on this behaviour. The thermal properties, such as the thermal conductivity and heat capacity, of the thin films are compared to those of bulk samples. Then, the heat transfer profiles of the multilayer structures interfaced to MEMS devices are calculated using a simplified thermal model. Emphasis is placed on elucidating heat transfer mechanisms within defect areas, such as thermal transfer due to mechanical contact, radiative exchange inside voids and convective heat transfer (as air or other gasses may be present in some defects, particularly if artificially created by methods such as those discussed in Chapter 6). The influence of parameters affecting the difference in surface temperature between the areas with and without defects for a one-dimensional system under steady-state conditions is evaluated using thermal calculations. Finally, models of areas with and without defects for a two-dimensional system in unsteady-state conditions are discussed, and the question as to whether transverse heat transfer significantly reduces the surface temperature difference is examined.

## 4.2 Microstructure of Thin Films in Thermal Conduction and Diffusion Model

Heat transfer physics describes the kinetics of energy storage, transport, and transformation by principal energy carriers: phonons (lattice vibration waves), electrons, fluid particles, and photons. Among these carriers, phonons, photons and electrons are the three vital heat carriers for thermal conduction and radiative heat transfer between solid materials. Heat is conducted in solids through free electrons and phonons. Similar to electrical conduction, free electrons dominate the heat conduction of metals, while in insulators and semiconductors, phonons are the major heat carriers. Photons are not only responsible for radiative heat transfer between separated solid surfaces but also play a significant role in heat transfer in transparent/translucent materials [142, 143]. The temperature and sample size both affect the thermal conductivity of a material. This section will discuss the consideration of temperature and size in calculations and simulations. Meanwhile, the possible reduction in the transfer of heat carries due to defects will also be discussed in the next section.

### 4.2.1 Temperature Effect

The rate of heat transfer depends on the temperature gradient and thermal conductivity of a material. Temperature changes cannot be avoided during manufacturing and operation nor during active thermographic detection. In addition, the temperature affects the thermal conductivity of a material because of its influence on heat carriers.

Most MEMS devices use solid materials. The thermal conductivity of metal and semiconductor materials increases with temperature, when the temperature is less than a specific value (usually less than 100-200 K). When the temperature is larger than 200 K, the thermal conductivity slightly decreases with temperature [144].

For instance, Figure 4.1 shows the thermal conductivities of silicon devices with different layer thicknesses over temperatures ranging from 10 to 400 K ($\eta$ is the surface roughness) [145]. The thermal conductivities of the silicon thin films increase from 10-20 to 200-300 W/m·K as the temperature increases from 10 K to 80 K and then continuously decrease to approximately 80 W/m·K at 400 K. As thermographic detection techniques require temperatures between 293 K and 343 K, the thermal conductivity of silicon will be in the range of 100 to 150 W/m·K.

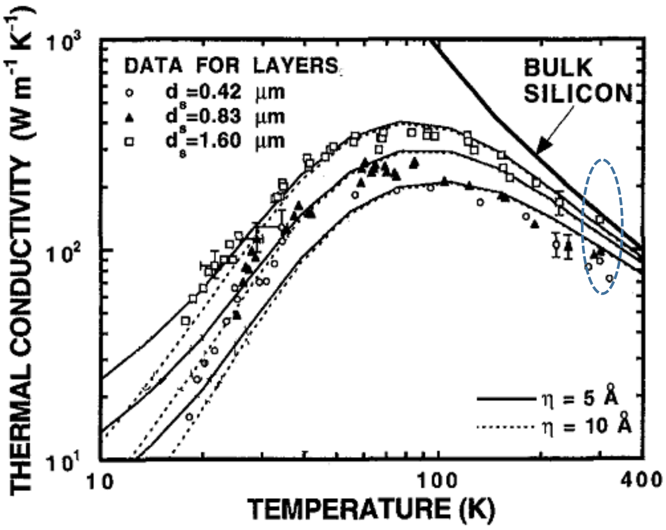

Figure 4.1 Thermal conductivities of silicon devices with various layer thicknesses [145].

Figure 4.2 shows the change in the thermal conductivity of a copper-nickel alloy with temperature [147]. From room temperature (273 K) to the maximum predicted working temperature (373 K), the increase in the thermal conductivity is very small. Thus, the effect of the temperature on the thermal conductivity can be neglected in simulations.

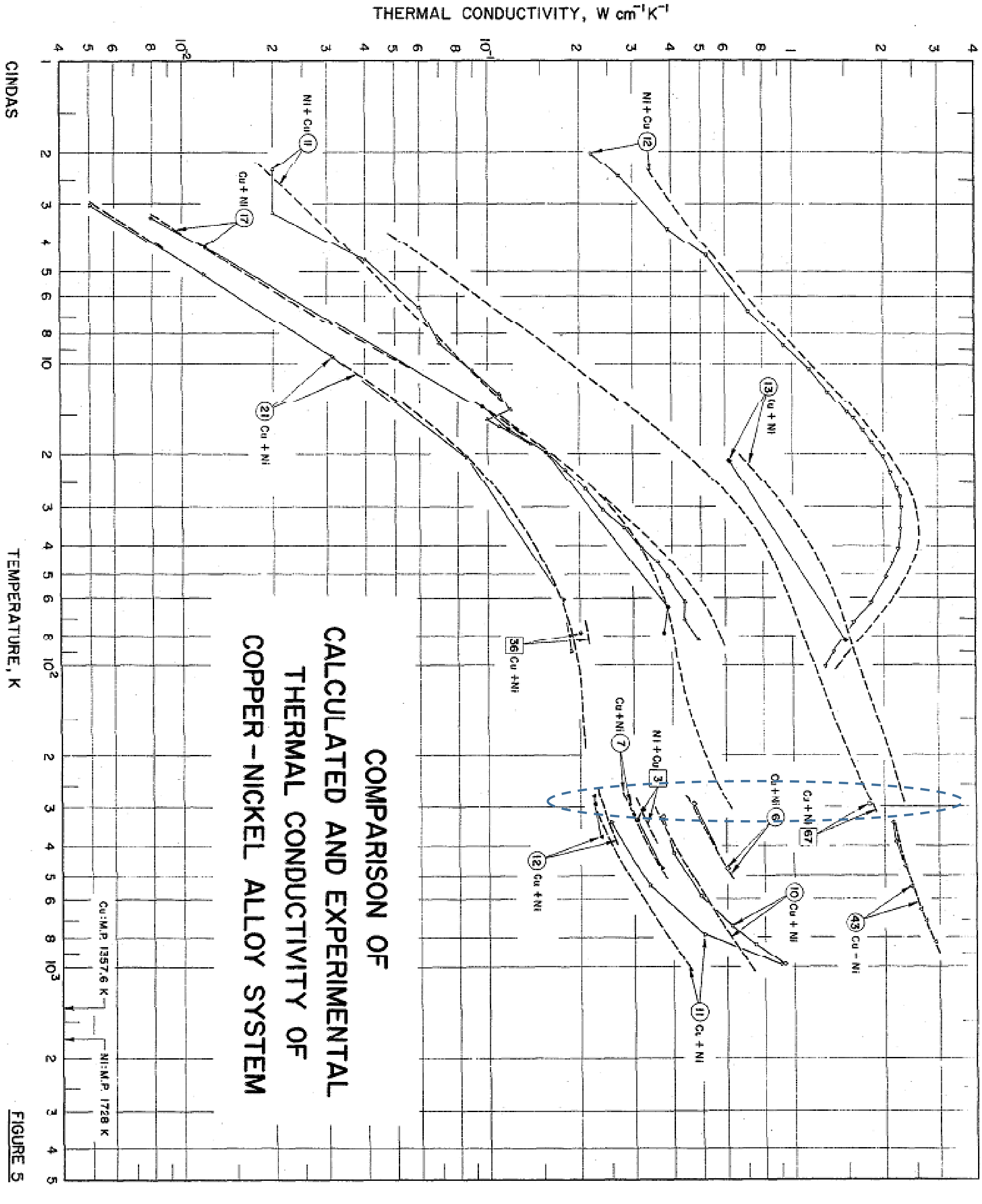

Figure 4.2 Changes in the thermal conductivity of a copper-nickel alloy with temperature [147].

### 4.2.2 Size Effect

Thermal conductivity is a physical property that varies between normal bulk samples and samples with smaller length scales. Recent studies have shown that the conductivities of semiconducting and superconducting films are often lower than that of their bulk counterparts. Nanostructures promote the reduction of thermal conductivity through size and interface effects, due to the improvement in both electron and phonon transport [148].

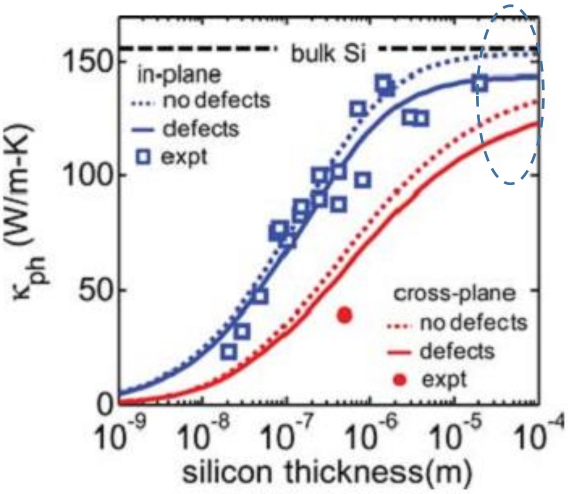

Figure 4.3 Relation between thermal conductivity and silicon layer thickness at room temperature [129].

According to simulations performed by Jeong [129], this reduction in the thermal conductivity of thin films relates to the microstructural differences between thin films and their bulk counterparts. When the thickness of a film is comparable with the mean free path of heat carriers, lattice conduction is expected to exhibit size effects (i.e., a thickness dependence). When the thickness is less than 0.2 µm, most of the heat is carried by phonons with mean free paths that are longer than the film thickness.

The simulations of silicon thin films by Jeong showed a slightly reduced thermal conductivity in the thin films compared with that for the bulk material when the thickness was less than $10^{-4}$ m (100 µm), as shown in Figure 4.3. In the silicon thin films, the measured cross-plane thermal conductivity was even lower than the in-plane thermal conductivity. Because the thickness of silicon substrates ranges from tens to hundreds of micrometres, the thermal conductivities of the defect-less silicon films of interest are 133 W/m·K (in-plane) and 151 W/m·K (cross-plane), as shown in Figure

4.3.

Figure 4.4 shows the thermal conductivity of silicon layers with thicknesses ranging from 0.01 to 50 μm at temperatures of 300 K and 308 K, as determined by Asheghi [149]. Although the bulk material results are slightly different from that of Jeong, the simulation results of the thin films are similar to the results achieved by Jeong.

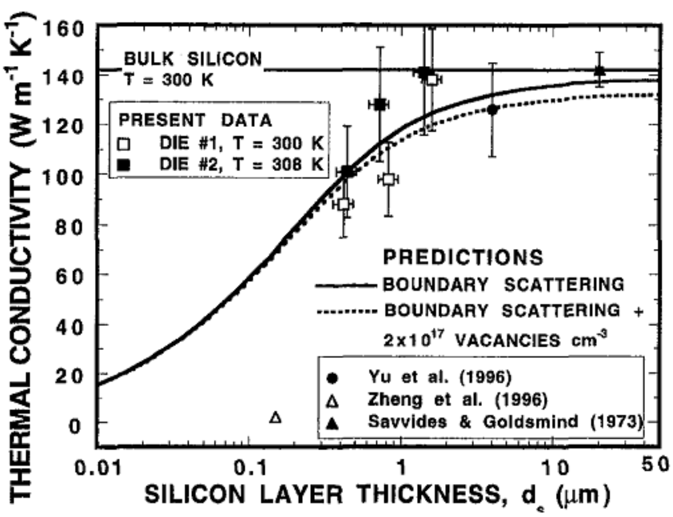

Figure 4.4 Room-temperature thermal conductivity data for silicon layers as a function of thickness [149].

Some researchers have also studied this size effect on MEMS metal materials. For instance, Nath and Chopra [130] examined copper films prepared by thermal evaporation with thicknesses ranging from 50 nm to 800 nm at temperatures of 100 and 325 K. The thermal conductivity of copper films shows a thickness dependence that was smaller at 325 K than at 100 K, as shown in Figure 4.5. In addition, similar to the bulk material, the conductivity of copper films with thicknesses over 600 nm was almost constant.

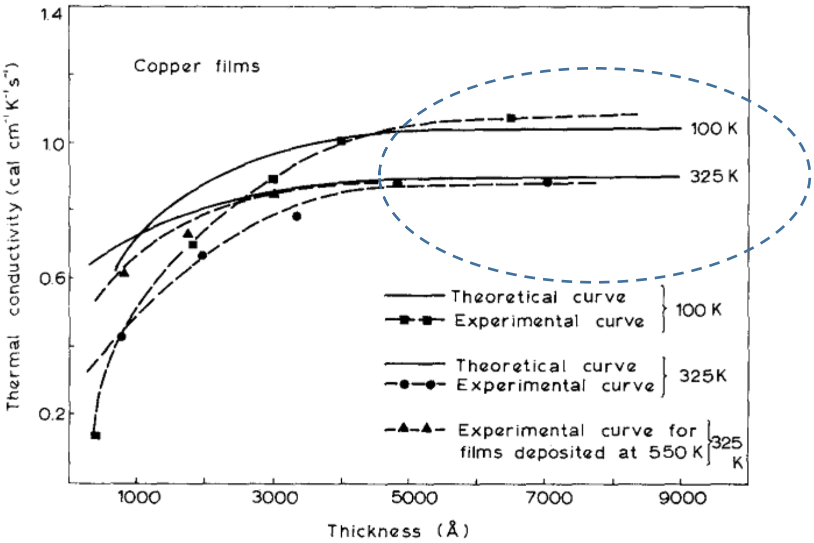

Figure 4.5 Relation between the thermal conductivity and the thickness of copper films [130].

Thus, for metal thin films, if the thickness is on the order of hundreds of micrometres, size effects can be ignored. When considering the thermal conductivity of semiconductor materials, such as a silicon substrates, with thicknesses of 300 µm, the use of the thermal conductivity of bulk silicon in the simulations in this project is satisfactory. Table 4.1 gives the room-temperature thermal properties of some bulk materials commonly used in the MEMS industry.

Table 4.1 Thermal properties of bulk metals and non-metals at room temperature [108, 127].

| **Metal materials** | **k (W/m·K)** | **ρ (kg/m$^3$)** | **c (kJ/kg·K)** |
|---|---|---|---|
| **Nickel** | 90 | 8906 | 0.4459 |
| **Aluminium** | 204 | 2707 | 0.896 |
| **Silver** | 419 | 10524 | 0.2340 |
| **Copper** | 386 | 8954 | 0.3831 |
| **Chrome-Nickel (90%)** | 17 | 8666 | 0.444 |
| **Semiconductor materials** | k (W/m·K) | ρ (kg/m$^3$) | c (kJ/kg·K) |
| **Silicon carbide (4H-SiC)** | 490 | 3210 | 0.68 |
| **Silicon (single crystal)** | 148 | 2330 | 0.700 |
| **Poly-silicon** | 34 | 2320 | 0.678 |
| **Gallium arsenide** | 50 | 5300 | 0.35 |
| **Silicon dioxide** | 1.4 | 2270 | 1.00 |
| **Germanium** | 60 | 5320 | 0.31 |
| **Quartz** | 6.7-12 | 2660 | 0.82-1.20 |

# 4.3 Modelling of Heat Transfer and Convection Cooling in a One-Dimensional System under Steady-state Conditions

## 4.3.1 Thermal Profile of a Multilayer Structure

Figure 4.6 shows the schematic cross section of a two-layer structure containing a defect, which involves a layer on top of a substrate and an interface. If the temperature is increased at the bottom boundary of the substrate, the temperature difference results in heat flowing from this higher temperature area to the lower temperature areas.

Bonding between correctly manufactured layers is typically considered perfect, and thus, the thermal resistance at the interface is extremely small, and the temperatures on both sides of the interface are equal. In contrast, delamination reduces the contact area at the interface, which leads to a very low thermal conductivity. Energy transfer is hindered at the interface between the two materials due to the thermal barrier created by the defect, and the resulting temperature of the top surface over the defect is lower.

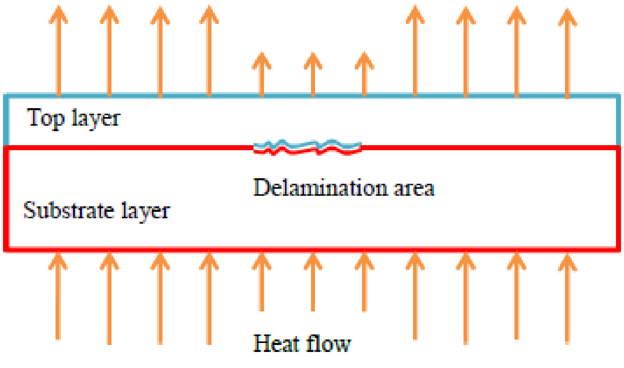

Figure 4.6 Schematic of heat flow through a two-layer structure containing an area of delamination.

For simplicity, the horizontal heat transfer (i.e., in plane) is assumed to be negligible, and only vertical heat transfer from the bottom of the substrate to the surface of the top layer is considered. Therefore, there are effectively two regions that can be treated separately, as shown in Figure 4.7 (a). One region considers the defect area, without including the edge of the defect, as shown on the left in Figure 4.7 (b). Because of the delamination, the upper and lower layers can be viewed as two solid regions separated by a gap. This gap can be considered as a plate of vacuum or gas. Similarly, the intact region is examined using a model of the top film, the substrate and an ideal interface, as shown on the right in Figure 4.7 (b).

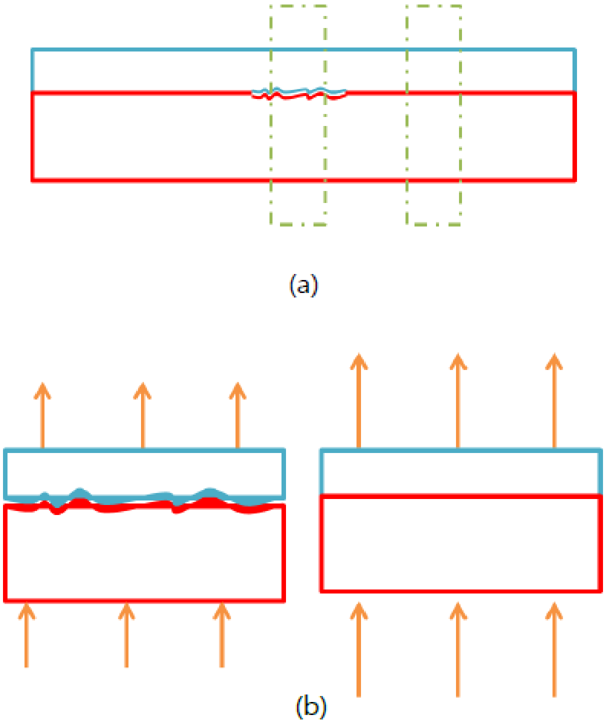

Figure 4.7 Simplified thermal model of a specimen with a defect by dividing the system into two regions.

If we assume that all the sections of the film are infinitely flat and that the bottom surface of the substrate layer is heated at a constant temperature over a long time, the calculation of the two-dimensional thermal conductance behaviour is simplified into two one-dimensional steady-state problems.

In the one-dimensional heat transfer profile shown in Figure 4.8, heat transfers from the bottom surface of the substrate layer, passes through the substrate, the interface and the top film and is finally emitted to the ambient atmosphere. The temperatures at the substrate bottom, the interface and the film surface are denoted $T_b$, $T_i$ and $T_s$, respectively. The text presents the external temperature, and the input and output energies are denoted $q_{in}$ and $q_{out}$, respectively. Among these temperatures, $T_b$ is the applied uniform temperature ($T_b$=ΔT+ $T_{ext}$) on the bottom surface of the substrate layer. ΔT is the temperature increment applied to the bottom surface, which was generally set to 50 K in this study in order to prevent the sample from being destroyed at high temperature.

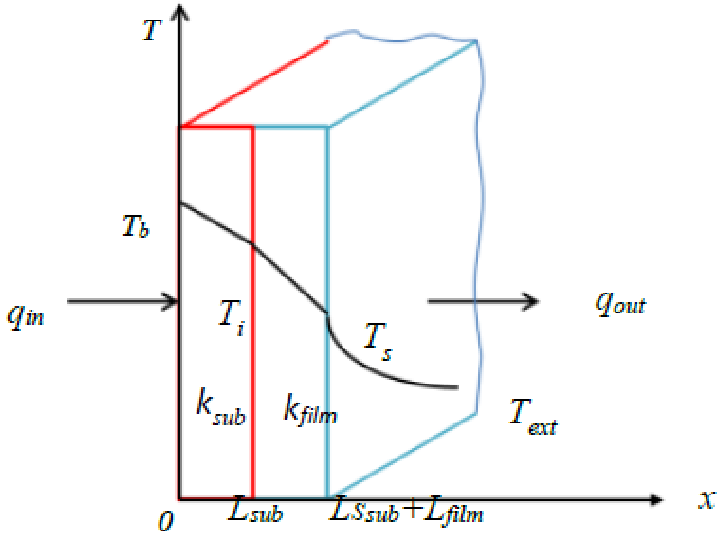

Figure 4.8 The temperature profile of one-dimensional heat transfer through a composite plate.

According to Fourier's law, when a temperature gradient exists in a body of a uniform cross-sectional area A, the energy transfer q from the high-temperature to the low-temperature region is:

$$q = -kA\frac{\partial T}{\partial x} \tag{4. 1}$$

where ∂T/∂x is the temperature gradient in the direction of heat flow and k is the thermal conductivity of the material. As discussed in the previous section, thin films of a material are assumed to be isotropic conductors, where k is constant and uniform. By considering the films in Figure 4.8 as plane plates, a direct application of Fourier's law can be made:

$$q = -\frac{k_{sub}A}{L_{sub}}(T_i - T_b) \tag{4. 2}$$

$$\mathrm{q} = -\frac{k_{film}A}{L_{film}}(T_s - T_i) \tag{4. 3}$$

where $k_{sub}$ and $k_{film}$ are the thermal conductivities (W/m·K) of the substrate and film material, respectively, and $L_{sub}$ and $L_{film}$ are the thickness of the substrate and the film.

Then, on the surface exposed to the ambient environment, the convection heat transfer follows Newton's law of cooling:

$$\mathrm{q} = \mathrm{hA}(T_s - T_{ext}) \tag{4. 4}$$

Here, the heat transfer rate is related to the overall temperature difference among the film surface, the ambient environment, and area A. The parameter h is the convection heat transfer coefficient. Equations (4.2), (4.3) and (4.4) can be reconstructed as:

$$T_b - T_i = \frac{q}{A} \times \frac{L_{sub}}{k_{sub}} \tag{4. 5}$$

$$T_i - T_s = \frac{q}{A} \times \frac{L_{film}}{k_{film}} \tag{4. 6}$$

$$T_s - T_{ext} = \frac{q}{A} \times \frac{1}{h} \tag{4. 7}$$

Because heat flux is uniform in a one-dimensional system, the increment ΔT between the applied temperature $T_b$ on the bottom surface and the external temperature $T_{ext}$ can be obtained by combining Equations (4.5), (4.6) and (4.7):

$$\Delta T = T_b - T_{ext} = \frac{q}{A}\left(\frac{L_{sub}}{k_{sub}} + \frac{L_{film}}{k_{film}} + \frac{1}{h}\right) \tag{4. 8}$$

The surface temperature $T_s$ can be expressed by rearranging Equation (4.8) as:

$$T_s = \frac{q}{hA} + T_{ext} \tag{4. 9}$$

Combining with Equation (4.8) gives:

$$T_s = \frac{\Delta T}{\left(\frac{L_{sub}}{k_{sub}} + \frac{L_{film}}{k_{film}} + \frac{1}{h}\right)h} + T_{ext} \tag{4. 10}$$

The typical thicknesses of nickel and silicon layers in a MEMS device are 10 μm and 300 μm. The natural convection cooling coefficient in air is typically approximately 5-25 W/m$^2$·K [151]. Because the layer thickness of the specimen (310 μm) divided by the thermal conductivity (148 W/m·K) is much smaller than 1/h, the sum of $\left(\frac{L_{sub}}{k_{sub}} + \frac{L_{film}}{k_{film}} + \frac{1}{h}\right)$ can be approximated to 1/h, and $\left(\frac{L_{sub}}{k_{sub}} + \frac{L_{film}}{k_{film}} + \frac{1}{h}\right)h$ is similar to 1+h×10$^{-6}$. Thus, the value of $\frac{\Delta T}{\left(\frac{L_{sub}}{k_{sub}} + \frac{L_{film}}{k_{film}} + \frac{1}{h}\right)h}$ is slightly smaller than ΔT, which indicates that the surface temperature $T_s$ ($= \frac{\Delta T}{\left(\frac{L_{sub}}{k_{sub}} + \frac{L_{film}}{k_{film}} + \frac{1}{h}\right)h} + T_{ext}$) is slightly lower than the bottom temperature $T_b$ ($T_{ext}+\Delta T$) and can be approximated as this value. The temperature difference in structures without defects is only approximately $10^{-5}$-$10^{-6}$ K. Thus, temperature difference at the surface and bottom of the structure with a defect can be calculated and used to predicted the largest achievable surface temperature difference between the sound and defect area.

## 4.3.2 Heat Transfer Mechanisms in Defects

As mentioned in Chapter 2, defects in multilayer structures occur mostly as delamination and voids. Due to the thermal expansion mismatch between the thin film and substrate, residual stress in the film may lead to delamination. In an opaque solid material, thermal energy is transferred by two modes: lattice vibration and free electron diffusion. Any separation between layers will interrupt these main transmission mechanisms. A better understanding of the thermal properties of such defects will help formulate appropriate thermal models for their simulation. Thermal contact conductance, thermal radiation exchange and air gap heat transfer are the three main transfer mechanisms that can occur between separated solid surfaces.

I. Thermal contact resistance

Thermal contact is a complicated phenomenon, and the contact pressure and contact area are the two factors with the most influence on the thermal contact conductance. At sites of delamination and cracks, i.e., a separation between formally bonded surfaces [152], the contact area between the two surfaces is small enough to ignore the thermal contact conductance. Because delamination in MEMS devices is often accompanied by deformation, the defects are prevented from healing, and thus, the contact resistance can be viewed as infinite. On the other hand, as shown in Table 4.2, the contact conductance of typical surfaces under a specific pressure load present a very large resistance, even without excess loading. The parameter $h_c$ represents the contact coefficient.

Table 4.2 Contact conductivity for some typical surfaces [108].

| **Surface type** | **Roughness, μ (m)** | **Temperature, °C** | **Pressure, bar** | **$1/h_c$ $m^2$·°C/W×$10^4$** |
|---|---|---|---|---|
| **Aluminium, ground, air** | 2.54<br>0.25 | 150<br>150 | 12-25<br>12-25 | 0.88<br>0.18 |
| **Copper, ground, air** | 1.27 | 20 | 12-200 | 0.07 |
| **Copper, milled, air** | 3.81 | 20 | 10-50 | 0.18 |
| **Copper, milled, vacuum** | 0.25 | 30 | 7-70 | 0.88 |

II. Radiative heat transfer

Thermal radiation is a form of electromagnetic radiation that is, in essence, generated by the thermal motion of charged particles, such as electrons, at temperatures above absolute zero, being converted into electromagnetic energy. Thermal radiation allows heat transfer between two objects without contact. Energy exchange between two surfaces depends on three factors: temperature, surface properties and geometry. When radiant energy strikes a material surface, a part of the energy is reflected, a part is absorbed and a part is possibly transmitted. The total energy reflected, absorbed and transmitted are represented symbolically by ρ, α and τ, respectively. According to the principle of the conservation of energy:

$$\rho + \alpha + \tau = 1 \qquad (4.\ 11)$$

An idealized physical body that absorbs all incident electromagnetic radiation is called a black body, where α=1. Such a body will emit the maximum theoretical amount of radiation; however, real materials emit a fraction of the energy, called the emissivity, of the black body energy level. The proportion of the emissive power of a body (E) to the emissive power of a black body ($E_b$) at the same temperature is equal to the absorptivity of the body:

$$\alpha = \varepsilon = \frac{E}{E_b} \qquad (4.\ 12)$$

This ratio is called the emissivity (ε) of the body. Most solid bodies do not transmit thermal radiation, and their transmission coefficient (τ) can be taken as zero, and $\rho + \alpha = 1$. Moreover, absorption and radiation occur on the surface of an object, and thus, the surface structure significantly affects these parameters [108].

The monochromatic emissivity $\varepsilon_\lambda$ is defined as the ratio of the monochromatic absorbed power of the body to the monochromatic absorbed power of a black body at the same wavelength and temperature. The monochromatic emissivity of a body varies with wavelength. According to Planck's Law, the emissive power of a black body per unit wavelength $E_{b\lambda}$ is defined as [108]:

$$E_{b\lambda} = \frac{C_1 \lambda^{-5}}{exp\left(\frac{C_2}{\lambda T}\right) - 1} \qquad (4.\ 13)$$

where $c_1$ and $c_2$ are two radiation constants ($c_1=2\pi hc_0^2=3.742\times10^8$ W·µm$^4$/m$^2$ and $c_2=(hc_0/k)=1.439\times10^8$ µm·K), $c_0$ is the speed of light in a vacuum ($2.998\times10^8$ m/s), and λ is the wavelength. The total thermal emission from a black body ($E_b$) over all wavelengths can be obtained by integrating Equation (4.13):

$$E_b = \int_0^\infty E_{b\lambda} d\lambda = \int_0^\infty \frac{c_2 \lambda^{-5}}{exp\left(\frac{c_2}{\lambda T}\right) - 1} d\lambda \tag{4. 14}$$

which can be expressed as:

$$E_b = \sigma T^4 \tag{4. 15}$$

where σ is the Stefan–Boltzmann constant ($5.669 \times 10^{-8}$ $W/m^2 \cdot K^4$). The total emissive energy of a black body is therefore proportional to the fourth power of its temperature, according to Equation (4.15). Thus, the emissive power of a real body can be determined by combining Equations (4.13) and (4.15):

$$E = \varepsilon \sigma T^4 \tag{4. 16}$$

The model in this study initially assumes that the defect consists of a perfect closed space containing a vacuum, i.e., without gas or impurities from the external environment. When heat is transferred through a region where a perfect vacuum exists, the only relevant mechanism is electromagnetic radiation. To simplify the model, the edge of the defect is ignored, and the surfaces of the defect are assumed to be equivalent to two infinite parallel planes, such that the entire defect geometry can be represented as a rectangular region, as shown in Figure 4.9 (a).

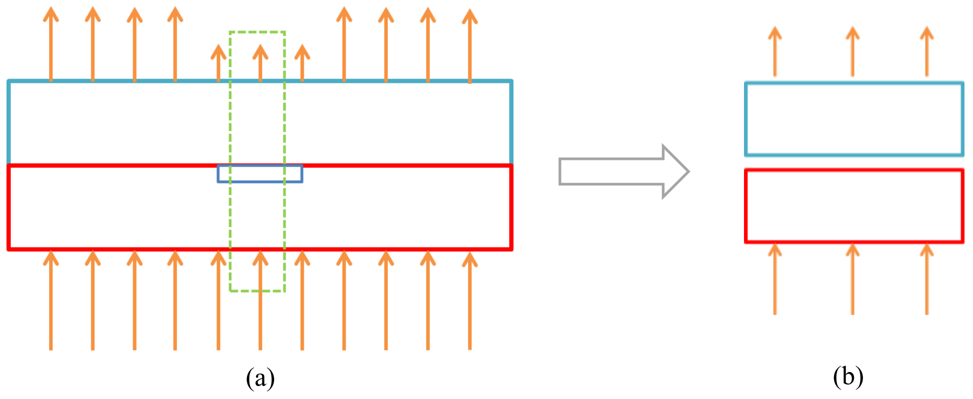

(a) (b)

Figure 4.9 Cross-sectional profile of (a) the simplified defect model and the (b) extracted region of the defect model.

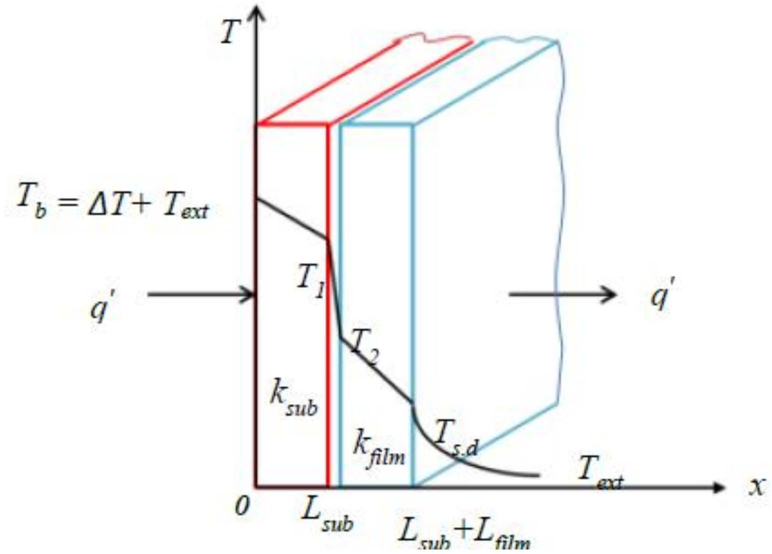

Figure 4.10 Temperature profile of one-dimensional heat transfer through a composite plate with an internal defect.

Figure 4.9 (b) shows the extracted section containing the defect without edge features. Since the upper and lower surfaces are the same, the thickness of the defect is extremely small, and in this one-dimensional model, the film and substrate can be considered as two infinite parallel planes separated by a vacuum. Figure 4.10 reveals the resulting temperature profile of this one-dimensional model, in which heat flow is obstructed by a high thermal resistance, in contrast to the defect-free model, shown in Figure 4.8, where heat transfers through the thin substrate. The quantity $T_1$ represents the upper surface temperature of the substrate, while $T_2$ represents the lower surface temperature of the film.

In this research, the temperature difference ($T_1$–$T_2$) across the defect and the influence of the defect on the observable surface temperature are the key factors to determine the possibility of thermographic detection. Therefore, the surface temperature image may reveal internal defect features; however, ($T_1$–$T_2$) is not equal to the temperature difference between the upper surfaces of the areas with and without defects ($T_s$–$T_{s.d}$). Since the heating temperature and external temperature in this system are fixed, the total steady-state heat flux (q) decreases to q' due to the defect resistance. Therefore, the temperature decrease through each plate is reduced. Thus, ($T_1$–$T_2$) should be slightly larger than ($T_s$–$T_{s.d}$) because the temperature gradient (temperature decrease/L) in the substrate and film is the same and the material properties and thickness of the substrate and film are constant in the steady state when q' is constant. This can be demonstrated as follows.

Similar to Equation (4.6), the temperature difference between the upper and lower surfaces of the film is:

$$T_2 - T_{s.d} = \frac{q'}{A} \times \frac{L_{film}}{k_{film}} \tag{4. 17}$$

If q' < q, then:

$$T_2 - T_{s.d} < T_i - T_s \tag{4. 18}$$

which can be rearranged to give:

$$T_s - T_{s.d} < T_i - T_2 \tag{4. 19}$$

At the same time, $T_b$ is fixed. When the heat flux decreases, the temperature difference ($T_b$–$T_i$) between the upper and lower surfaces of substrate decreases, indicating that ($T_b$–$T_i$) is larger than ($T_b$–$T_1$). Thus, $T_i < T_1$ and

$$T_s - T_{s.d} < T_1 - T_2 \tag{4. 20}$$

Since the two planes are infinite and parallel, the full emissive power ($\varepsilon_1 E_{b1}$) leaving the surface of one plane will reach the surface of the other plane. The other plane absorbs part of the emissive power ($\varepsilon_1\varepsilon_2 E_{b1}$), reflects the remaining power ($\varepsilon_1(1-\varepsilon_2)E_{b1}$) and emits its own power ($\varepsilon_2 E_{b2}$):

$$\mathrm{q} = \frac{E_{b1} - E_{b2}}{\frac{1-\varepsilon_1}{\varepsilon_1 A_1} + \frac{1-\varepsilon_2}{\varepsilon_2 A_2} + \frac{1}{A_1 F_{12}}} \tag{4. 21}$$

where $F_{12}$ is the radiation shape factor, which is unity since all the radiation leaving one plane reaches the other, and $A_1$ and $A_2$ are the areas of the two infinite surfaces. Thus, letting $F_{12}=1$, $A_1=A_2$. The radiation exchange $q_r$ (q') per area in this case can be determined by:

$$\frac{q_r}{A} = \frac{\sigma}{\frac{1}{\varepsilon_1}+\frac{1}{\varepsilon_2}-1}\left({T_1}^4 - {T_2}^4\right) \tag{4. 22}$$

According to Newton's law of cooling, the temperature of a surface can be expressed by the heat transfer rate, area, convective heat transfer coefficient and room temperature as follows:

$$T_s = \frac{q}{Ah} + T_{ext} \tag{4. 23}$$

Thus, the surface temperature of the model with a vacuum defect can be determined by combining Equations (4.22) and (4.23):

$$T_{s.d} = \frac{\sigma\left({T_1}^4-{T_2}^4\right)}{\left(\frac{1}{\varepsilon_1}+\frac{1}{\varepsilon_2}-1\right)h} + T_{ext} \tag{4. 24}$$

When the emissivities $\varepsilon_1$ and $\varepsilon_2$, Stefan-Boltzmann constant $\sigma$ and cooling convection heat transfer coefficient h are fixed, the heat transfer per area $q_r/A$ is proportional to the difference in absolute temperatures to the fourth power.

The surface temperatures are in the order of $T_b > T_1 > T_2 > T_s > T_{s.d} > T_{ext}$, and $T_b=\Delta T+T_{ext}$. Because the thickness of the thin film is extremely small, the temperature difference between the upper and lower surfaces is small. In addition, the reduced power exchange reduces the change in temperature across the plate. Thus, $\left({T_1}^4 - {T_2}^4\right)$ is similar to but less than $\left({T_b}^4 - {T_{ext}}^4\right)$:

$$\frac{\left({T_1}^4-{T_2}^4\right)}{\left(\frac{1}{\varepsilon_1}+\frac{1}{\varepsilon_2}-1\right)h} < \frac{\left({T_b}^4-{T_{ext}}^4\right)}{\left(\frac{1}{\varepsilon_1}+\frac{1}{\varepsilon_2}-1\right)h} \tag{4. 25}$$

The difference between the two equations for the temperature of the surface with a defect ($T_{s.d}$) and that without a defect ($T_s$) is determined by subtracting Equation (4.24) from Equation (4.23):

$$T_s - T_{s.d} = \frac{q}{Ah} - \frac{\sigma(T_1{}^4 - T_2{}^4)}{\left(\frac{1}{\varepsilon_1} + \frac{1}{\varepsilon_2} - 1\right)h} \tag{4. 26}$$

Substituting into Equation (4.26) gives:

$$T_s - T_{s.d} > \frac{1}{h}\left(\frac{q}{A} - \frac{\sigma(T_b{}^4 - T_{ext}{}^4)}{\frac{1}{\varepsilon_1} + \frac{1}{\varepsilon_2} - 1}\right) \tag{4. 27}$$

Considering that T$_b$ is the constant boundary temperature, which is ΔT higher than the external temperature T$_{ext}$, substituting in Equation (4.10) gives:

$$T_s - T_{s.d} \geq \frac{1}{h}\left(\frac{\Delta T}{\frac{L_{sub}}{k_{sub}} + \frac{L_{film}}{k_{film}} + \frac{1}{h}} - \frac{\sigma((T_{ext} + \Delta T)^4 - T_{ext}{}^4)}{\frac{1}{\varepsilon_1} + \frac{1}{\varepsilon_2} - 1}\right) \tag{4. 28}$$

To simplify this equation, the following constants are defined:

$$C_k = \left(\frac{L_{sub}}{k_{sub}} + \frac{L_{film}}{k_{film}}\right)h \tag{4. 29}$$

and

$$C_\varepsilon = \frac{\sigma}{\left(\frac{1}{\varepsilon_1} + \frac{1}{\varepsilon_2} - 1\right)h} \tag{4. 30}$$

Therefore, Equation (4.28) becomes:

$$T_s - T_{s.d} \geq \frac{\Delta T}{C_k + 1} - C_\varepsilon\left((T_{ext} + \Delta T)^4 - T_{ext}{}^4\right) \tag{4. 31}$$

$$T_s - T_{s.d} \geq \frac{\Delta T}{C_k + 1} - C_\varepsilon\left(\Delta T^4 + 4T_{ext}\Delta T^3 + 6T_{ext}{}^2\Delta T^2 + 4T_{ext}{}^3\Delta T\right) \tag{4. 32}$$

According to the discussion of the values of h and $\frac{L_{sub}}{k_{sub}} + \frac{L_{film}}{k_{film}}$, for typical specimen L≈$10^{-5}$-$10^{-4}$ m and k≈40-200 W/m·K, external environmental conditions give h≈10-25 W/m$^2$·K, and C$_k$ is a constant with a value of approximately $2.30\times10^{-6}$-$5.9\times10^{-5}$, resulting in its effect being negligible.

As shown in Table 4.3, according to previous work, the emissivity value of a material can vary considerably, especially with surface roughness or when contaminated, for example, by being oxidized. In addition, considering that copper, nickel and silicon may all be present at the defect surface, the emissivity of the defect surface should be between 0.03 and 0.9, indicating that $C_\varepsilon$ ranges from $3.45\times10^{-11}$ to $4.63\times10^{-9}$.

Table 4.3 Emissivity coefficients of various surfaces exposed to low-temperature thermal radiation [108, 131, 132].

| Surface | Emissivity at 25°C |
|---|---|
| Aluminium, highly polished | 0.04 |
| Aluminium, heavily oxidized | 0.20-0.31 |
| Copper, highly polished | 0.03 |
| Nickel, oxide | 0.2-0.5 |
| Chromium | 0.4 |
| Gold, highly polished | 0.018 |
| Silicon | 0.54-0.7 |
| Silicon carbide | 0.9 |

In Equation (4.32), when the external temperature $T_{ext}$ is fixed at a constant 293 K (20 °C, room temperature), the minimum difference between surface temperatures $T_s$–$T_{s.d}$ can be viewed as a unary quartic polynomial of $\Delta T$. Because $\Delta T$ is set to less than 100 °C in order to prevent the destruction of the devices, although a quartic polynomial is nonlinear, the trend of $T_s$–$T_{s.d}$ relative to $\Delta T$ can be determined. Figure 4.11 reveals the trend in the surface temperature difference for the max and min $C_k$ and $C_\varepsilon$ calculated using the extreme properties of MEMS materials.

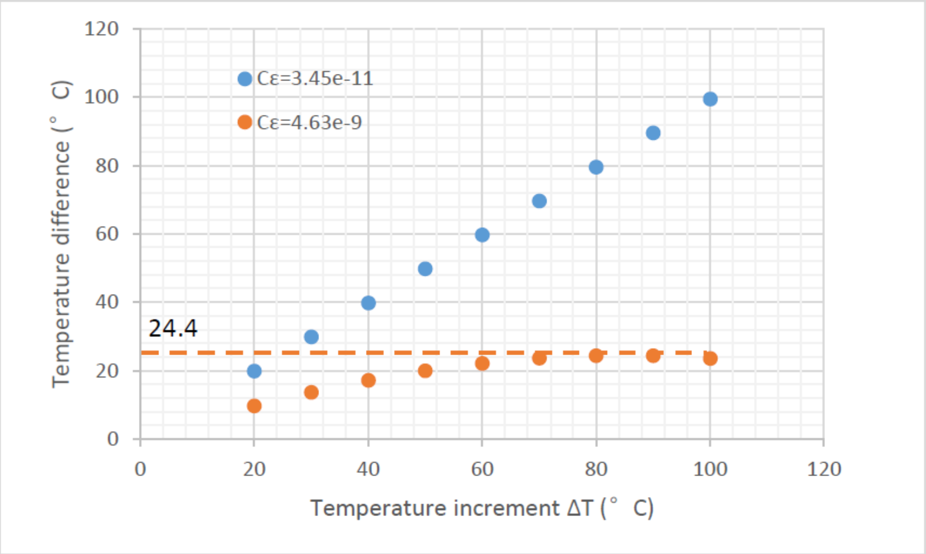

Figure 4.11 Change in the temperature difference $T_s$–$T_{s.d}$ with increasing heating temperature when the external temperature is 20 °C.

The diagram confirms that the surface temperature difference $T_s$–$T_{s.d}$ increases as the heating temperature ΔT is increased. The coefficient $C_\varepsilon$ of the model with a defect has an important influence on the increase in the temperature difference. The smaller the coefficient, the larger the resulting temperature difference. In addition, for the same heating temperature, the temperature difference will increase if the cooling convection coefficient increases. Meanwhile, a higher defect surface emissivity can reduce the temperature difference. A higher emissivity defect makes it easier for heat to flow.

The external temperature also slightly affects the surface temperature difference, especially when $C_\varepsilon$ is very large. Figure 4.12 presents the change in the temperature difference with same coefficients as used in Figure 4.11 but at an external temperature of 0 °C. For the low-emissivity defect, the effect of external temperature is very small, resulting in an increase of only 0.1 °C in $T_s$–$T_{s.d}$ relative to that at 20 °C (room temperature). Conversely, for the high-emissivity defect, the external cooling environment increases the temperature difference by between 2 and 12 °C. Despite the small increment, a lower external temperature could also increase the ratio between the temperature difference to the external temperature, which provides more accurate detection with less noise, in situations where increasing the external temperature is not advisable.

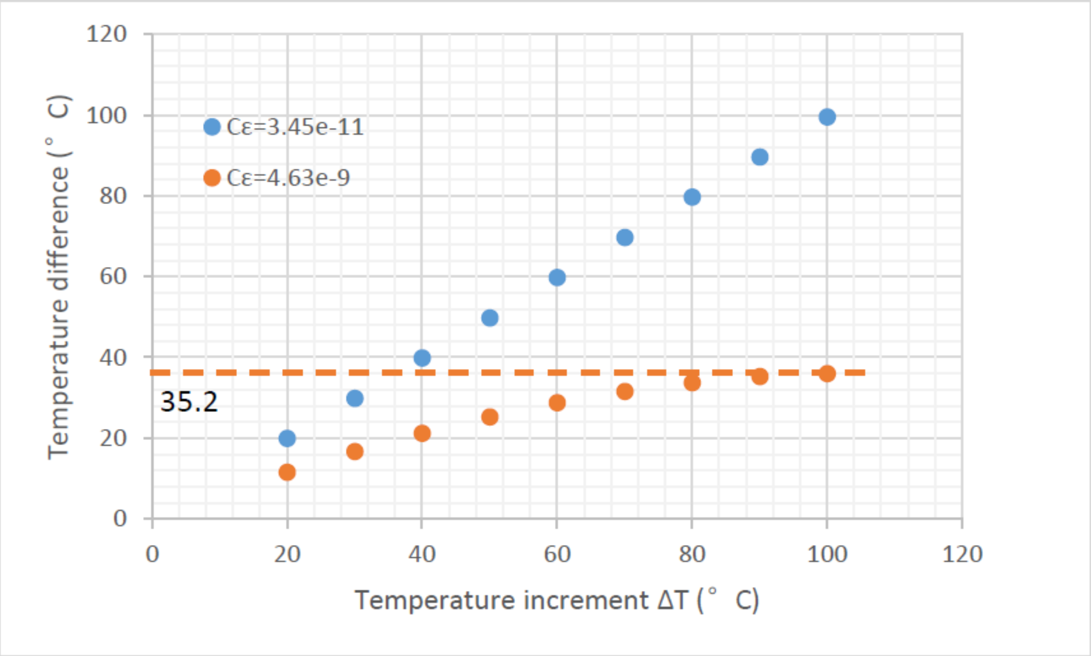

Figure 4.12 Trend of the temperature difference with increasing heating temperature when the external temperature is 0 °C.

To calculate the precision of detection, we divided the surface temperature difference by the temperature of the surface over the undamaged area, as shown in Figure 4.13. As the temperature rises, the relative ratio of the temperature difference to the surface temperature clearly increase when the radiation emissivity of the defect surface is large. However, for the model with low defect emissivity, the precision gradually declines from its peak at ΔT=80 °C. These results indicate that simply increasing the heating temperature does not enlarge the detection accuracy ($T_s$–$T_{s.d}$/$T_s$). However, reducing the external temperature helps to increase the accuracy of the model with a high-emissivity defect. The detection accuracy and relative detectability can both be used to validate the detection method.

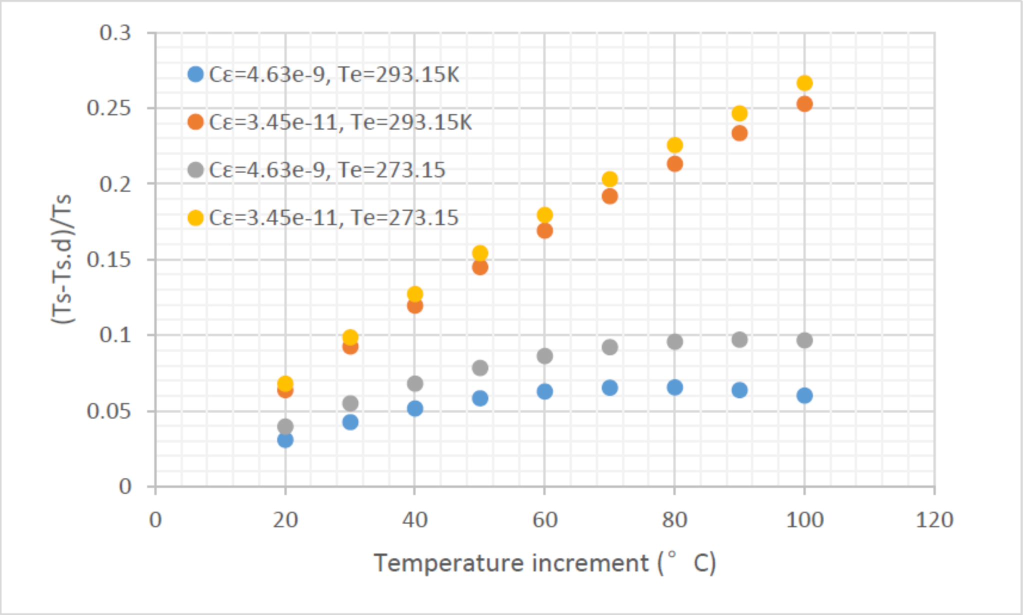

Figure 4.13 Ratio of the surface temperature difference ($T_s$-$T_{s.d}$) to the surface temperature of the defect-free area.

Therefore, in thermal detection, when an internal defect occurs in a material with high emissivity, such as silicon carbide, it may be difficult to induce a large surface temperature difference; however, decreasing the external temperature can enlarge the surface temperature difference and make detection easier.

III. Heat transfer through defects containing air

In most analytical references of thermographic detection, the air gap interface for delamination, cracks or voids is considered in the calculation, but not radiation exchange [157, 158]. The interspace of a model may be chosen to contain air because the quartic polynomial of radiation exchange is more difficult to calculate than that of an air wall and artificial defects are often filled with air. Even if the interspace is full of air, the thermal mechanism is similar to heat transfer in a solid but not convection, because the fluidity of air in a small and enclosed space is restricted. Thus, the surface temperature of the model with a defect can be rewritten with the air plane resistance as follows:

$$T_{s.d} = \frac{\Delta T}{\left(\frac{L_{sub}}{k_{sub}}+\frac{L_{film}}{k_{film}}+\frac{L_d}{k_{air}}+\frac{1}{h}\right)h} + T_{ext} \tag{4. 33}$$

Plugging $C_k$ into this equation gives:

$$T_{s.d} = \frac{\Delta T}{C_k+\left(\frac{L_d}{k_{air}}+\frac{1}{h}\right)h} + T_{ext} \tag{4. 34}$$

Therefore, the temperature difference between the defect and sound areas can be written as:

$$T_s - T_{s.d} = \frac{\Delta T}{C_k+1} - \frac{\Delta T}{C_k+1+\left(\frac{L_d}{k_{air}}\right)h} \tag{4. 35}$$

Then, extracting $\left(\frac{L_d}{k_{air}}\right)h$ gives:

$$T_s - T_{s.d} = \frac{\left(\frac{L_d}{k_{air}}\right)h\Delta T}{(C_k+1)\left(C_k+1+\left(\frac{L_d}{k_{air}}\right)h\right)} \tag{4. 36}$$

$$T_s - T_{s.d} = \frac{\Delta T}{(C_k+1)\left(\frac{C_k}{h}\frac{k_{air}}{L_d}+\frac{k_{air}}{hL_d}+1\right)} \tag{4. 37}$$

Because $C_k$ is much smaller than 1, the equation is approximately equal to:

$$T_s - T_{s.d} \approx \frac{\Delta T}{\left(\frac{L_{sub}}{k_{sub}}+\frac{L_{film}}{k_{film}}\right)\frac{k_{air}}{L_d}+\frac{k_{air}}{hL_d}+1} \tag{4. 38}$$

where $L_d$ is the thickness of the defect on the microscale (taken as 1 μm) and $k_{air}$ is the thermal conductivity of air, which is very small (0.024 W/m·K). Plug these parameters into Equation (4.38) gives:

$$T_s - T_{s.d} \approx \frac{\Delta T}{0.05664+2.4\frac{1}{h}\times 10^4+1} \tag{4. 39}$$

Because the value of h ranges from 10-25 W/m$^2$·K, $2.4\frac{1}{h}\times 10^4$ is much larger than 1. Therefore, the temperature difference is approximately equal to 4.2 $h\Delta T\times 10^{-3}$. The equation is similar to that for radiation exchange, and increasing the convection constant h, increasing the heating temperature ΔT or reducing the external temperature $T_{ext}$ can all enhance the surface temperature difference $T_s$–$T_{s.d}$. Although the temperature difference calculated using an air gap is smaller than that of radiation exchange, the impact factors are the same. Because the calculation is based on the steady state and heat transfer from the sound area to the defect area is neglected, the real temperature be different to a certain extent. The purpose of the state-steady analytical calculation is to predict the maximum achievable temperature difference with various influencing factors, such as the thickness and thermal characteristics of the film and substrate. The defect in the simulation model is simplified into a thin film.

## 4.4 Summary

In conclusion, the thermal conductivity, thickness of the plates and convection heat transfer coefficient are influencing factors in the study of the thermal behaviour of a multilayer structure in steady-state conditions. However, due to the very low thickness, the reduction in the surface temperature due to the thin-film resistance is very small. The temperature at the surface above the defect is dependent on the thermal resistance of the interspace. Three heat transfer mechanisms through the interspace were investigated, of which thermal contact conductance is impossible. Thermal radiation exchange is the most probable mechanism of heat transfer through a defect in a device. While heat transfer through air is very commonly used in theoretical calculations for practical experiments.

According to the radiation exchange calculation, the radiation characteristics of the defect play a decisive role in the resulting surface temperature. Reducing the external temperature, properly increasing the heating temperature and enhancing convection on the surface can enlarge the temperature difference between the surfaces over the defect and defect-free areas. In the calculation of a defect filled with air, the thermal model is viewed as a composite plane with a solid plate made of air. The result shows that the surface temperature difference is very small – on the order of thousands of the heating temperature.

However, all the issues discussed in this section focus on a one-dimensional system with steady-state conduction. If the two models are merged into a two-dimensional model, transverse heat transmission will rapidly decrease the surface temperature difference, especially when the diameter of the defect is very small. However, considering the heat capacity of the material of the film above the defect, the heat capacity of filled air and the time needed for radiation exchange equilibration, a certain surface temperature difference should exist until the system stabilizes, as shown in Figure 4.14. For heat diffusion, energy requires a certain time to diffuse around the thermal barrier and arrive at the surface above the defect. Thus, the next chapter will focus on the study of the surface temperature difference during diffusion in unsteady-state conditions.

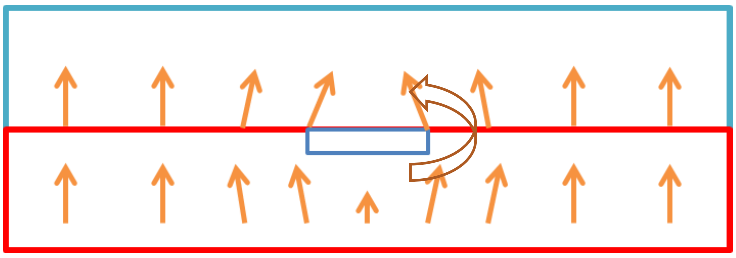

Figure 4.14 A sketch illustrating the effect of the defect geometry on the heat flux path.

# Chapter 5 Thermal Simulation of a Layered Structure under Unsteady-state Conditions

## 5.1 Introduction

This chapter focuses on the thermal conduction behaviour of a layered structure containing an internal defect under unsteady-state conditions. The modelling details, such as the simulation software, geometry of the model and boundary conditions, are given in the first section. Then, the second and third sections discuss the simulation of the model with two excitation methods: constant temperature excitation and constant heat flux excitation. The detectability, temperature distribution over the surface and response time, which are important in the thermographic NDT method, are numerically studied. The simulation results are compared with the theoretical analysis given in Chapter 4 to verify the feasibility and validity of the transient thermographic NDT method in transmission mode. Finally, the materials used in the model are replaced by other materials commonly used in MEMS structures to analyse the relationship between the thermal characteristics of a material and the thermal behaviour model.

## 5.2 Modelling of Heat Transfer in the Unsteady State

An increased temperature difference can be achieved by measuring the temperature difference before the system reaches the steady state. For this, the temperature must be measured before the heat flows from the high-temperature area (defect-less area) to the low-temperature area (defect area). However, because analysing a 2D model in the unsteady state is difficult, most research has focused on numerical solutions. Thus, this section will analyse the 2D defect model and boundary conditions in the unsteady state.

### 5.2.1 COMSOL Multiphysics

Establishing an analytical model for heat transfer in a multi-dimensional system under unsteady-state conditions is not possible; thus, the finite element method (FEM), also known as finite element analysis (FEA), is used to solve this problem. FEA is a numerical method used to analyse complex mechanical and structural problems by dividing the structure into simpler parts. FEA is capable of analysing both static and dynamic problems and is a good choice for solving partial differential equations (PDE) and integral equations in complex structures [153].

COMSOL Multiphysics is a typical solver software that uses the FEA technique for modelling and simulating various physics-based problems, in particular, multiphysics phenomena [154]. This software provides a simulation platform with many physical interfaces for electrical, mechanical, fluid flow, and chemical applications. COMSOL conveniently provides a material library that includes elements, metal alloys, thermal insulators, semiconductors, and piezoelectric materials [155].

In the COMSOL software, the Heat Transfer in Solid (to the study the behaviour of heat in a solid) and Structure Mechanics (to validate and predict thermal stress during heating) modules were used to obtain results in this thesis.

### 5.2.2 Geometry of the Model

The COMSOL Multiphysics software has two 2D modelling modes: 2D and 2D axisymmetric. A 2D axisymmetric meshed slice can be rotated into a 3D cylinder model. To avoid the influence of corners, the defect in the model is simply described as a circle. Because of the symmetry effect, it is only necessary to compute the temperature distribution for the nodes at one side of the model. Thus, as a 2D axisymmetric model is used, and the entire model can be viewed as a stack of three cylinders. Since the uniformity of heat transfer is disturbed mainly around the defect, the thicknesses of the seed and top film layers are the main factors influencing the observed surface temperatures. Therefore, the model is divided into two parts: the layered film with a defect and the substrate. In the 2D axisymmetric model, there are two coordinates: space (r) and space (z).

As shown in Figure 5.1, for simplicity, the lower boundary of the defect (upper surface of the substrate) is set to z=0, and the centreline of the defect extends from z=0 to z=L_d. The substrate is below the r-axis, and the bottom of the substrate is located at z=-L_sub, which is the thickness of substrate. L_d is the thickness of the seed layer with the defect. L_film is the thickness of the film. The model surface is located at z=L_d+L_film. The vertical lines that run across the specimen from the bottom surface to the top surface are denoted “centre line cross film”, “centre line cross substrate”, “crack edge line” and “sound area line” at peak time=170 µs, which will be further discussed in section 5.3.2.

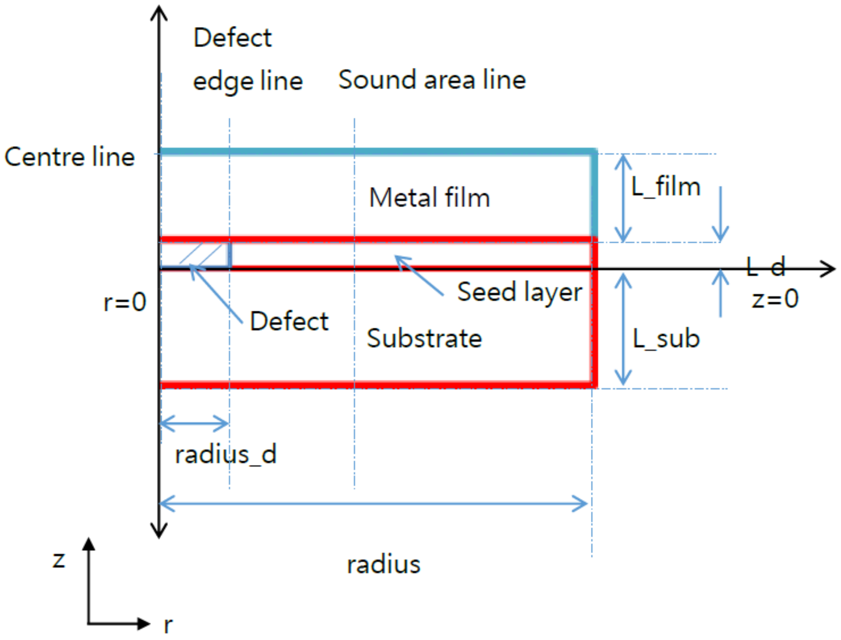

Figure 5.1 Details of the size of the multilayer structure with an internal defect.

The numerical model was developed using parameters extracted from the experiment in Chapter 3 by assuming a uniform 200 µm-thick silicon layer, a 1 µm-thick sputtered copper seed layer and a 20 µm-thick electroplated nickel layer, all with isotropic uniform material properties. Table 5.1 gives the geometrical parameters of the model.

Based on the assumption that there is no significant thermal resistance at the interface between layers, the layers in the simulation were built as well-bonded geometry domains (the thermal resistance is negligible). A 50 μm-radius defect is located within the copper layer, as shown in Figure 5.1, and the nickel and silicon layers were separated by the defect. In the real experiment, some copper components may contain residue on one or both layers, which affects the thermal behaviour of the defect in the considered boundary conditions. This defect is assumed to occur within an effectively infinite plate, and the ratio of the width of the plate to its thickness is at least 10. The defect area is set as a vacuum, and another model with the defect regarded as an air plane is established for comparison. Meanwhile, the width of the film and substrate is set to be more than 10 times of that of the defect. Relevant data from COMSOL's built-in material parameters library were used for the three layers, as listed in Table 5.2.

Table 5.1 Geometrical parameters of the layered model with a defect.

| Name | Value[μm] | Description |
|---|---|---|
| radius_d | 50 | Radius of defect |
| L_film | 20 | Thickness of film |
| L_d | 1 | Thickness of defect |
| L_sub | 200 | Thickness of substrate |
| radius | 5·L_sub | Radius of film and substrate |

Table 5.2 Materials properties [155].

| Material | Heat capacitor at constant pressure (J/kg·K) | Thermal conductivity (W/m·K) | Density (kg/m$^3$) |
|---|---|---|---|
| **Silicon** | 700 | 130 | 2329 |
| **Nickel** | 445 | 90.7 | 8900 |
| **Copper** | 384 | 401 | 8960 |
| **Air** | 1007 | 0.024 | 1.161 |

Several Bezier polygons were used to divide the model into rectangles to reduce the number of mesh elements and simplify the model. The affected area, including the defect tip and the sound area near the defect tip (with a length of one defect radius), was modelled with a fine-size mesh (maximum 1 μm) to effectively improve the accuracy of the numerical simulation, while the rest of the samples were modelled with coarse-size mesh, as shown in Figure 5.2. The complete mesh consists of 1327 quadrilateral elements. The model was compared with that using a free triangular mesh, and the same simulation results were obtained.

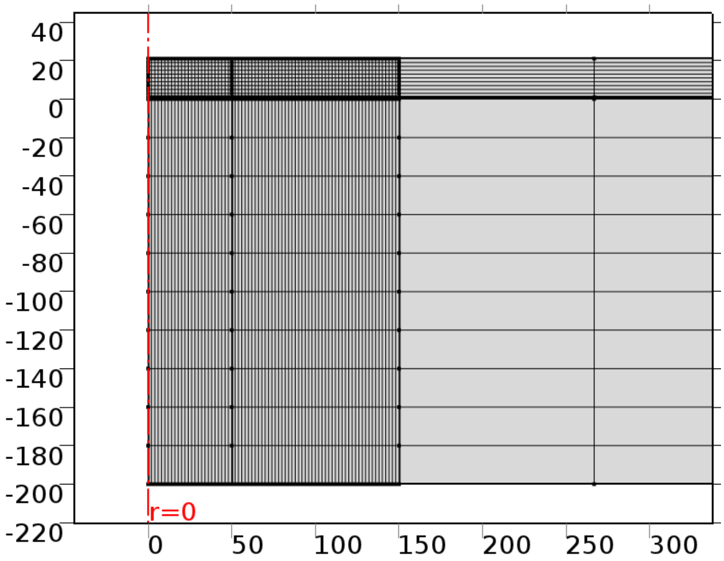

Figure 5.2 Finite element mesh of the multilayer structure.

### 5.2.3 Boundary and Initial Conditions

To determine the variation in the temperature distribution over time, the heat conduction equation must be solved. The solution of this equation is dependent on the boundary conditions and requires the knowledge of the initial conditions within the solid at the initial time.

Two direct heating methods are commonly used for thermographic detection: 1) physical contact with a sudden high temperature on the bottom, i.e., a hot plate, and 2) heated by stimulation with a sudden heat energy, i.e., laser, flash, etc.

The first method is somewhat unrealistic, especially when heat is required to be transferred in a very short time. However, in practice, for safety, the fixed temperature method makes it much easier to control the overall temperature of the specimen in order to support the heat flux and prevent the specimen from being destroyed by high temperature in the experiment. A Dirichlet (or first type) boundary condition in thermodynamics is where a surface is suddenly applied a fixed temperature [127, 154]. In the model, a fixed temperature boundary $T_b=T_{ext}+\Delta T$ is applied over the entire bottom surface of the substrate. Section 5.3 discusses the temperature response to this boundary condition.

Laser heating is commonly used in thermographic NDT tests [127]. However, this type of heating may lead to the temperature increasing more slowly, which does not create an obvious temperature difference on the surface to detect internal defects. In addition, laser heating may continue heating the specimen and increase the temperature to a dangerously high value, reducing the reliability or even destroying the specimen during the test. Therefore, the constant heat flux boundary condition, which is often referred to as a Neumann (or second type) boundary condition, is used. Thus, the heating energy and duration must be carefully set to avoid the destruction of the specimens, which are fully investigated in section 5.4.

Table 5.3 Boundary condition coefficients.

| Name | Value | Description |
|---|---|---|
| $h_{ext}$ | 10 [W/m$^2$·K] | Convection heat transfer coefficient |
| E | 0.5 | Emissivity of defect surfaces ε |
| $T_{ext}$ | 293.15 [K] | External temperature $T_{ext}$ |
| ΔT | 50[°C] | Heating temperature increment ΔT |

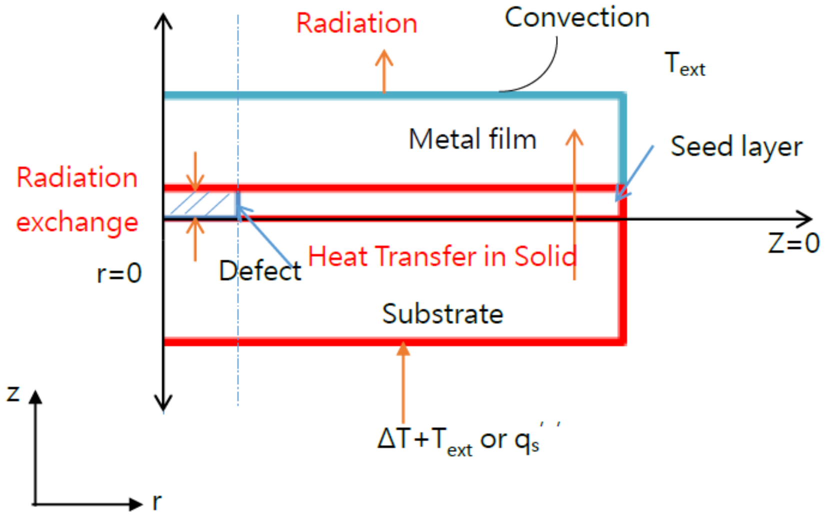

Figure 5.3 Schematic model for the measurement of heat transfer in a solid.

The defect area is assumed to contain a vacuum, and radiation exchange is the only thermal exchange mechanism between the surfaces. The emissivity of the defect surfaces is set at 0.5, according to the discussion in Chapter 4 (Table 5.3). Figure 5.3 shows a schematic of the boundary conduction in the model.

For constant material properties, the differential equation for the temperature distribution T(z, t) is [156]:

$$\frac{\partial^2 T}{\partial z^2} = \frac{1}{\alpha}\frac{\partial T}{\partial \tau} \tag{5. 1}$$

The quantity $\alpha = k/\rho c$ represents the thermal diffusivity of the material, $\rho$ is the density of the material, c is the capacity of the material under constant pressure, and $\tau$ is the time. The larger the value of $\alpha$, the faster heat will diffuse through the material.

Initially, the whole model is at ambient temperature:

$$T(r, z, t) = T_{ext} \tag{5. 2}$$

where t is the time and T(r, z, 0) is the temperature of model when t=0.

For the first boundary condition, the temperature of the surface of the substrate is:

$$T(-L_{sub}, t) = T_{ext} + \Delta T, \text{ t} > 0 \tag{5. 3}$$

For the second boundary condition, the heat flux ($q_z''$) of the surface of the substrate is equal to the supplied heat flux ($q_s''$):

$$q_z''(-L_{sub}) = -k\frac{\partial T}{\partial z} = q_s'', \text{ z=-L}_{\text{sub}} \tag{5. 4}$$

According to Fourier’s law, the heat flux is related to the temperature gradient $\partial T/\partial z$.

Convection heating or cooling of a surface is the third type of boundary condition. Since the specimen is heated from the substrate surface, convection cooling mainly effects the top surface:

$$-k\frac{\partial T}{\partial z} = h(T_{ext} - T(L_d + L_{film}, t)),\ z=L_d+L_{film} \tag{5.5}$$

where $T(L_d + L_{film}, t)$ is the temperature of the film surface and h is the convection heat transfer coefficient.

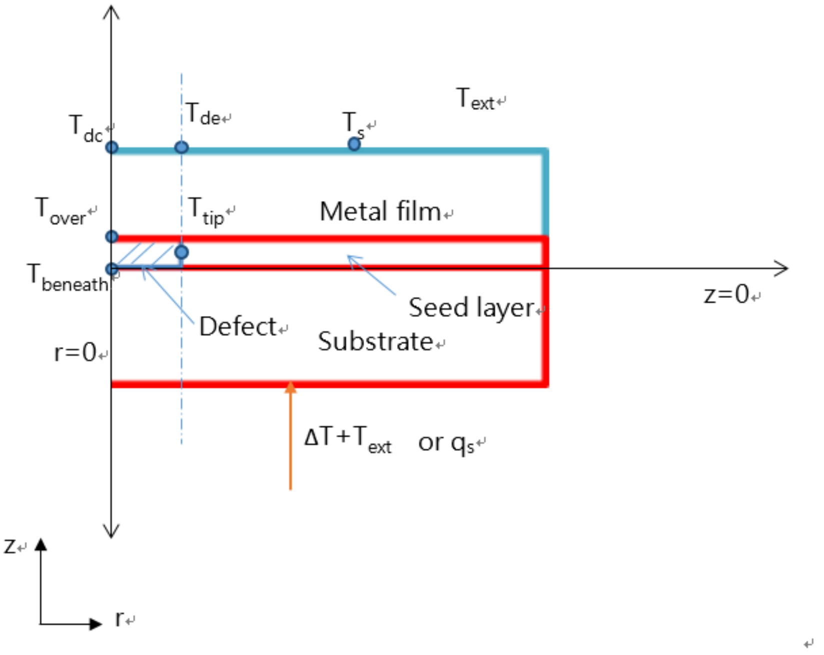

Figure 5.4 Relevant temperature data points.

The points around the defect and in the non-damaged area evaluated in this study are indicated in Figure 5.4. $T_{dc}$ is the temperature of the film surface just above the defect centre, $T_{de}$ is the temperature of the film surface just above the defect edge, $T_s$ is the temperature of the film surface over the non-damaged area, $T_{beneath}$ is the temperature of the substrate just beneath the defect centre, $T_{over}$ is the temperature of the centre surface over the defect, and $T_{tip}$ is the temperature on the defect edge half way through the film thickness. The temperature changes at these points are investigated in the following study.

### 5.2.4 Time-dependence study

When the bottom surface of the model has a sudden applied fixed temperature $T_{ext}+\Delta$

T, the temperature distribution in the solid part is a function of the time and position. Fully heating the whole model requires a significantly long time; however, the speed of the temperature increase during heating will gradually slow when the value reaches approximately $T_{ext}+\Delta T$. Thus, excess time and computer memory will be wasted if the whole heating duration is simulated. Because the period of interest is when the temperature increases rapidly and the temperature difference of the surfaces is detectable, the thermal model can be viewed as a resistance-capacitor circuit during charging at a given voltage. The time constant is equal to the product of the resistance and capacitance. For practicality, the capacitor is considered to be fully charged by the 3-5th time constant [127]. Thus, the time constant of the thermal model can be obtained by calculating the product of the thermal resistance and thermal capacitance of the material used in the model ($t_{constant} = \mathrm{cLA}\rho \cdot \frac{L}{kA} = \frac{cL^2\rho}{k}$). In MEMS devices, the thickness of the substrate is much larger than that of the thin film, and thus, the substrate material supplies most thermal resistance and capacitance. Thus, we chose the thermal resistance and capacitance of silicon to calculate the time constant and obtained a value of approximately 1 ms.

A time-dependent model is used to analyse the characteristics of heat transfer in a multilayer structure. When the surface of a solid body is subjected to a change in temperature or heat flux, the temperature of each internal point begins to change, and some time must elapse before a new equilibrium temperature distribution is reached. During the first few microseconds, when the temperature sharply rises, the time step is set at 10 μs, the initial step is 1 μs, and the relative tolerance is $1\times10^{-6}$. Because the goal of this simulation is to obtain obvious temperature differences, excess time steps will occupy memory and waste time. In addition, an obvious temperature difference often occurs around at a constant time point. Thus, the total study time is set to 2 ms, which is twice the approximate time constant. The mesh consists of 5700 linear quadrilateral elements. The total simulation time of one heating pulse is approximately 20 s.

## 5.3 Analysis of the Model with a Constant Heating Temperature

This section first analyses a model consisting of 20 µm Ni/1 µm Cu/200 µm Si with a 50 µm-radius defect to examine the surface temperature over time and space to detect and measure defects. The temperature difference, time of the peak temperature difference and surface temperature gradient are discussed. Then, the effect of the internal temperature distribution on the surface temperature is discussed. Finally, the influences of factors such as the depth of the defect, the thickness of the substrate and the radius of the defect on the detectability are analysed in detail.

### 5.3.1 Spatial and Temporal Surface Temperature Variation

Figure 5.5 (a) shows the 3D rotation temperature model formulated by the 2D model rotation after 2 ms of heating at 70 °C ($\Delta T$=50 °C). The 3D rotation temperature model presents 3/4 of the film surface of the whole structure, revealing the surface temperature and two cross sections showing the internal temperature distribution. In the cross section of the model, the temperature decreases from the substrate surface to the film surface. A slightly lower temperature area (the dark colour area) at the centre of the model can be seen in the magnified surface temperature image in Figure 5.5 (b), which reveals the internal defect area. Thus, the simulation result indicates that active transmission thermographic NDT can detect the defect from the surface temperature. However, the difference between the highest and lowest temperature in the model at 2 ms is less than 0.01 °C, because the centre of the defect was heated for too long of a time, making it impossible for the thermal camera to detect the difference in the experiment. Therefore, the following study determines the ideal detection time.

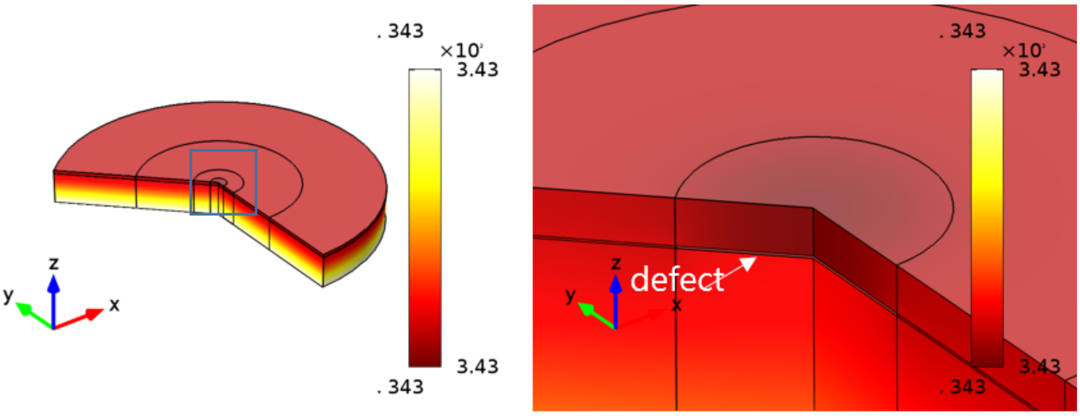

(a) (b)

Figure 5.5 3D surface temperature plot of (a) the entire model after 2 ms of heating and (b) magnified at the defect area.

Moreover, Figure 5.6 shows five surface temperature variations from the defect centre to the edge of the model after 0 µs, 100 µs, 200 µs, 300 µs, 400 µs, and 500 µs of heating. The predicted temperatures at the surface from the defect centre to the edge of the model also indicate a significantly lower temperature area around the defect during heating. The surface temperature over the defect centre ($T_{dc}$) is the lowest and increases as the distance from the radius increases. Meanwhile, the average temperature of the specimen rises sharply with time. However, these temperature plots reveal a non-linear relationship between the temperature difference and the heating period, which indicates that the best detection time is neither at the start nor the end of the heating duration. Additionally, for a specimen with a 50 µm-radius defect, the surface temperature in the r direction steadily increases. The temperature over the defect tip ($T_{de}$) is neither the highest nor the lowest. Thus, measurement of the size of the defect and locating its edge are additional problems, which are discussed in this section.

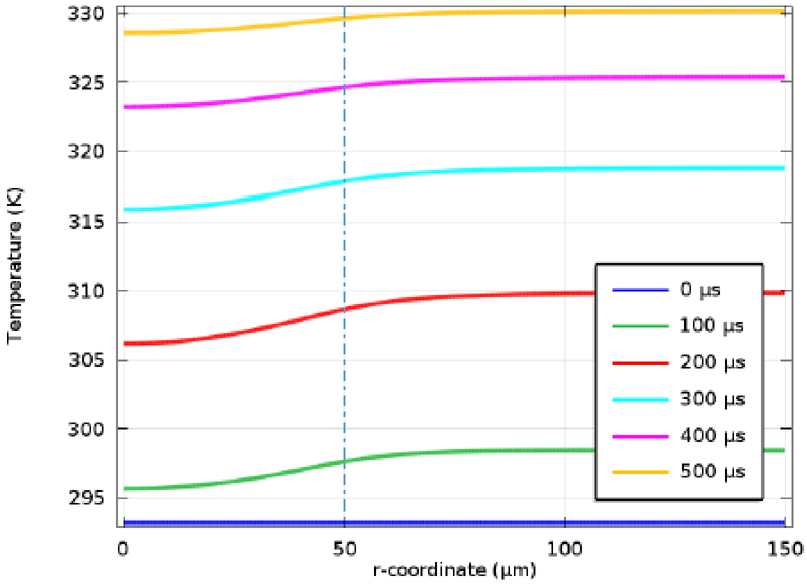

Figure 5.6 Surface temperature variation from the defect centre to the non-damaged area after 0 µs, 100 µs, 200 µs, 300 µs, 400 µs, and 500 µs of heating.

To further evaluate the change in the temperature distribution, three points on the surface of the model were selected: above the defect centre $T_{dc}$, at the edge of the defect $T_{de}$, and in the sound area far away from the defect $T_s$. Figure 5.7 presents the temperatures at these points, along with the temperature difference at the non-damaged and defect-centre points $T_{s-dc}$ over time before the temperature equilibrates (from start to 1 ms). After a short period of heat transfer from the bottom to the surface, at 40 µs, the temperature at the three points increases and then gradually levels off. The surface temperature over the sound area and defect edge increases more quickly than that over the defect centre at the beginning. Thus, the temperature difference shows rapid growth from 40 µs, similar to that at the three points, but with a steeper slope, and peaks at t=170 µs, before declining slowly.

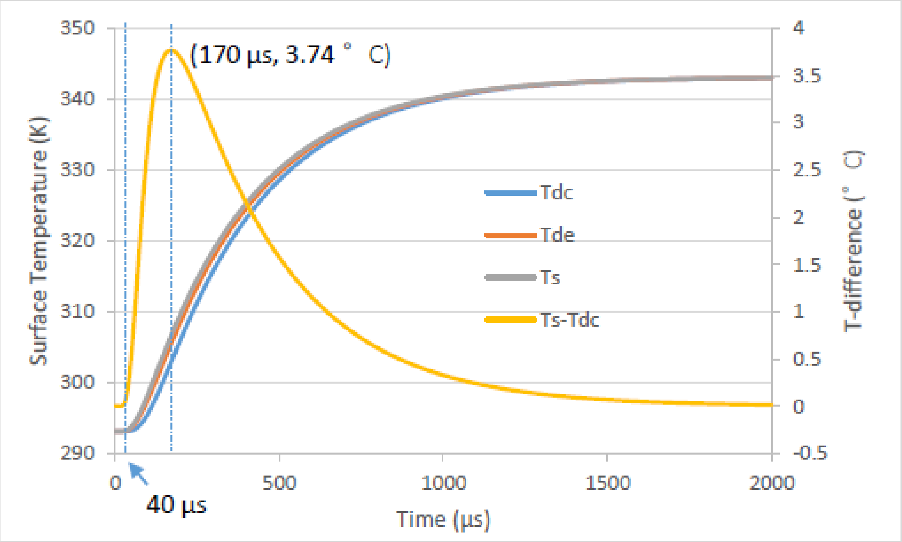

Figure 5.7 Surface temperature lines and surface temperature difference of the defect centre and non-damaged areas over time.

Figure 5.8 provides a clearer image of these temperature changes by replotting the data with the r-axis on a log scale. The log-scale temperature-difference curve presents a rare mirror symmetrical trend at t=170 µs (maximum temperature difference). The peak temperature difference occurs at 170 µs, and its value is 3.76 °C. Thus, 40 µs to 1250 µs is considered to be ideal observation time window to locate defects using the temperature difference. In this window, the temperature difference is larger than 0.2 °C (thermal sensitivity of a typical thermal camera). Meanwhile, Figure 5.9 shows the relative detectability $-\frac{\Delta T_{dc}}{\Delta T_s} = \frac{\Delta T}{\Delta T_s}$ ($\Delta T_{dc}$ is the change in $T_{dc}$ from the initial temperature and $\Delta T_s$ is the change in $T_s$ from the initial temperature), which was defined in Chapter 2. This definition is the ratio of the temperature difference to the temperature variation on the surface. However, the change in surface temperature is very small at the beginning of heating due to the transient heating method, and the ratio is improved when the temperature difference is large enough. As seen in Figure 5.9, when the time is longer than 800 µs, the detectability is approximately equal to 0. Therefore, in this case, considering the achievable temperature difference and relative detectability, the observation time window is set between 40 µs and 800 µs.

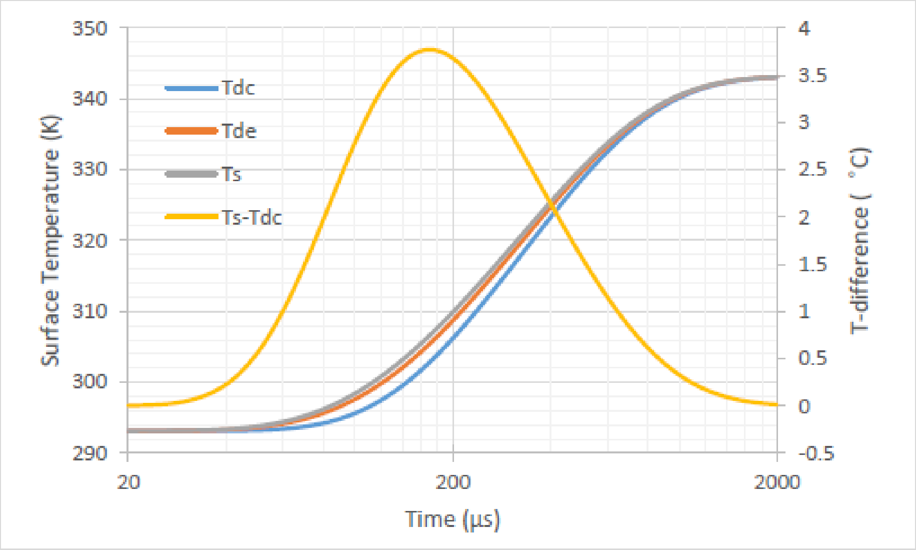

Figure 5.8 Surface temperature profiles from Figure 5.7 replotted with the r-axis on the log scale.

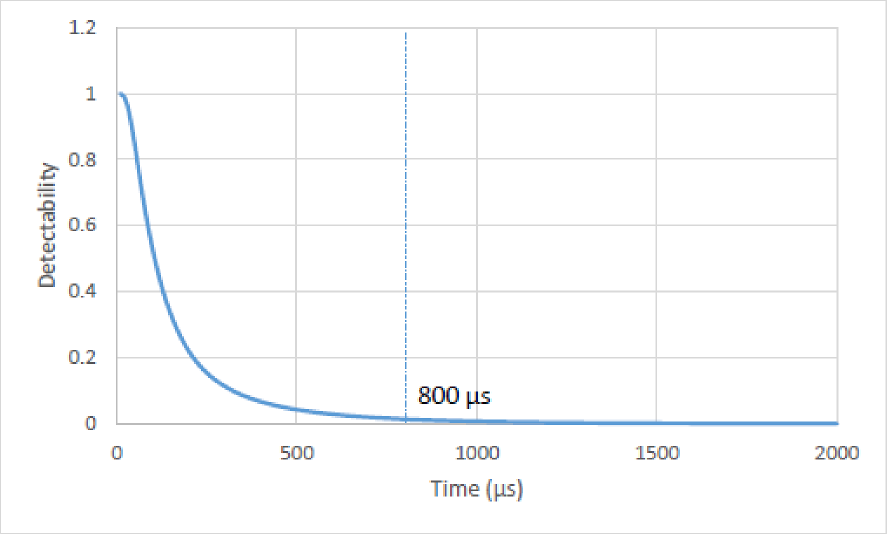

Figure 5.9 Relative detectability of the defect as a function of time.

## 5.3.2 Internal Vertical Temperature Distribution in a Solid

The change in the surface temperature is dependent on the internal heat flux around the defect, as well as the internal temperature distribution. The internal temperature distribution is essential for analysing and elaborating the surface temperature distribution and difference. Moreover, the thermal characteristics and thickness of the materials also influence the internal temperature distribution, which provide intuitive physical interpretations and provide a reference for the analysis of the surface temperature distribution.

Figure 5.10 (a) shows the temperature distribution along the z direction of the sound area, the crack area and the crack edge (lines in Figure 5.1) at 170 μs after heating. The temperatures at all these regions decrease from the bottom of the substrate to the film interface. The average rate of temperature change is calculated to be approximately 0.21 °C/μm at the sound area and the crack edge. However, at the near-defect regions, the local temperature is predicted to be higher, as heat exchange with the air or in vacuum is far less than that in the substrate material. In the sound film, the temperature drops continuously during heat conduction in the solid nickel, which possesses a similar thermal conductivity as the silicon substrate. However, in contrast to heat transfer across the defect-free region, the heating of the film in the crack area and at the crack edge is restricted, since the heat is slowly exchanged through thermal radiation at low temperature. The temperature therefore suddenly decreases in the z direction of the film at the crack edge and at the obvious fault in the centre of the crack region (Figure 5.10 (b)). As this limited heating also retards the heat flow into and inside the nickel film, the temperature gradient along the z direction of the film is minor, which increases greatly as the distance from the centre of the crack region increases due to the stronger horizontal heat conduction from the solid area.

Figure 5.10 (c) and (d) show the predicted temperature profiles from the model with the defect set as an air plane. According to the obtained results, the temperature distribution at the substrate/film interface becomes continuous as a result of heat conduction between the substrate and the air. However, the heat conduction in the air layer is insufficient (0.024 W/m·K) compared to that of nickel (90.7 W/m·K). Thus, the improvement in the heating on the surface of the film is minor. Although an additional method of heat conduction is introduced in the air-defect model, other than thermal radiation, the temperature distribution is similar to that achieved from the vacuum-defect model. Therefore, the following numerical investigations are carried out using the vacuum-defect model.

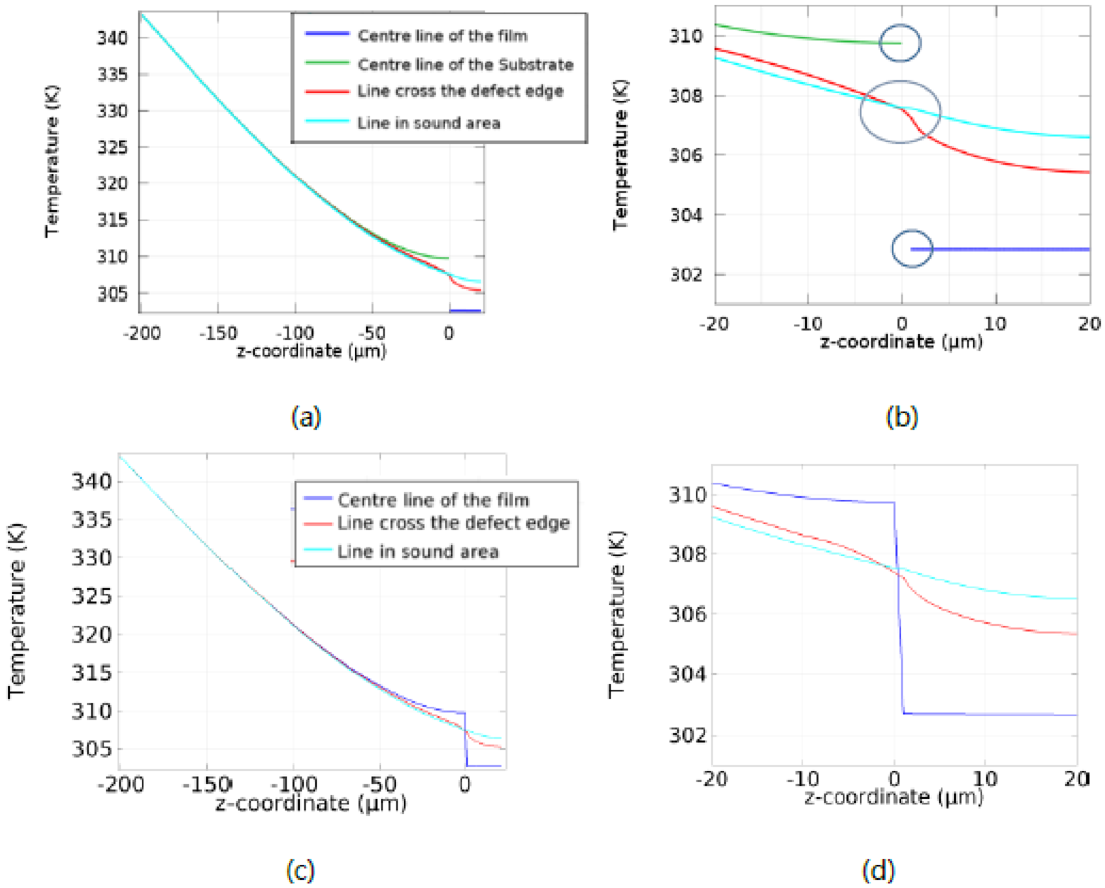

Figure 5.10 Temperature profiles of the model with a vacuums defect in the z direction of the (a) defect centre, defect edge and non-damaged area and (b) magnification at the interface area. Temperature profiles of the model with an air defect in the z direction of the (c) defect centre, defect edge and non-damaged area and (d) magnification at the interface area.

## 5.3.3 Isotherm contour

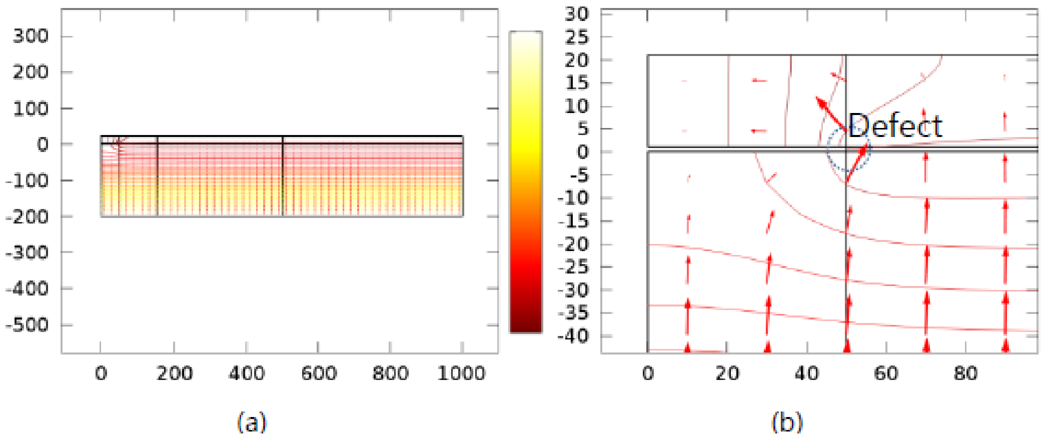

Figure 5.11 Isothermal contours and arrows profile of (a) the entire model (full view) and (b) magnification at the defect area.

In the isotherm plots, the contour lines reveal the temperature distribution, while the arrows represent the direction and magnitude of the heat flux. Figure 5.11 (a) reveals the isotherm contour and arrow image of the entire model after 170 μs of heating from the bottom, i.e., when the surface temperature difference is maximized. The temperature difference between the adjacent contour lines is 1 °C. The denser the contour lines, the larger the temperature gradient. Figure 5.11 (b) shows the magnified image at the defect area, and the sparseness of the contour lines indicates the slight temperature difference between the film and substrate around the defect centre, implying that the heat flux is extremely low. The defect can be viewed as a thermal barrier around which the heat is forced to flow. Therefore, the path length of heat transfer is increased, and the surface temperature at the defect centre ($T_{dc}$) increases more slowly. The duration for the growth of $T_{dc}$ is the best detection window.

Figure 5.12 shows that the temperature of the area over and below the defect ($T_{over}$ and $T_{beneath}$) changes with time, and the temperature difference corresponding to the temperature of the defect tip ($T_{tip}$) is approximately that of the sound area at the same depth. Compared with Figure 5.8, the peak temperature difference over the defect (4.73 °C) occurs slightly earlier t=160 μs (considering the time step is 10 μs), while the peak temperature difference beneath the defect (2.28 °C) occurs at t=140 μs.

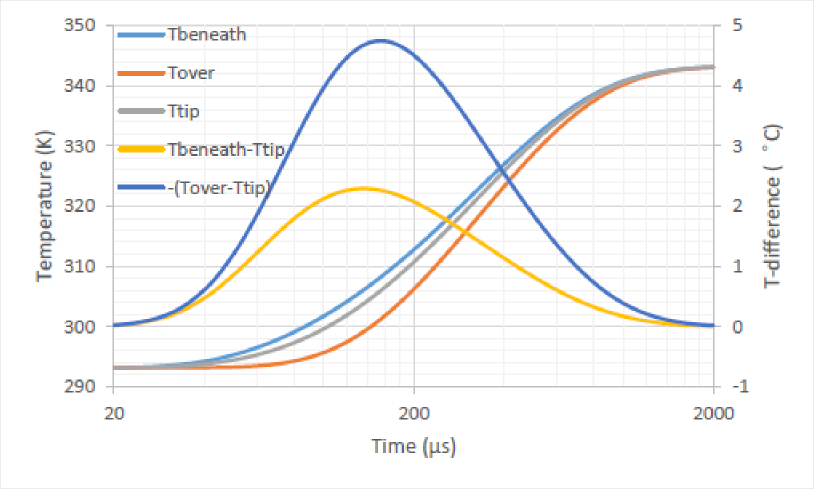

Figure 5.12 Internal temperature and temperature difference over time on the log scale.

Figure 5.13 provides a clearer image of the ratio of the change in temperature over time over and beneath the defect with respect to that of the sound area ($\frac{dT_{over}}{dt}/\frac{dT_{tip}}{dt}$ and $\frac{dT_{beneath}}{dt}/\frac{dT_{tip}}{dt}$). The temperature at the area beneath the defect rises earlier and faster than that at the defect-free area due to reflection from the defect surface. While the temperature at the area over the defect rises later and slower than that at the defect-free area. However, all points reach the same increment after 800 μs, because the centre area over the defect (r=0) maintains the same temperature increment along the z direction, while the temperature at the area over the defect rises more slowly than that at the sound area. The time delay results from the longer diffusion distance of heat transfer. Thus, the increment and peak time are related with the radius and depth of the defect, which are analysed in detail in the last section.

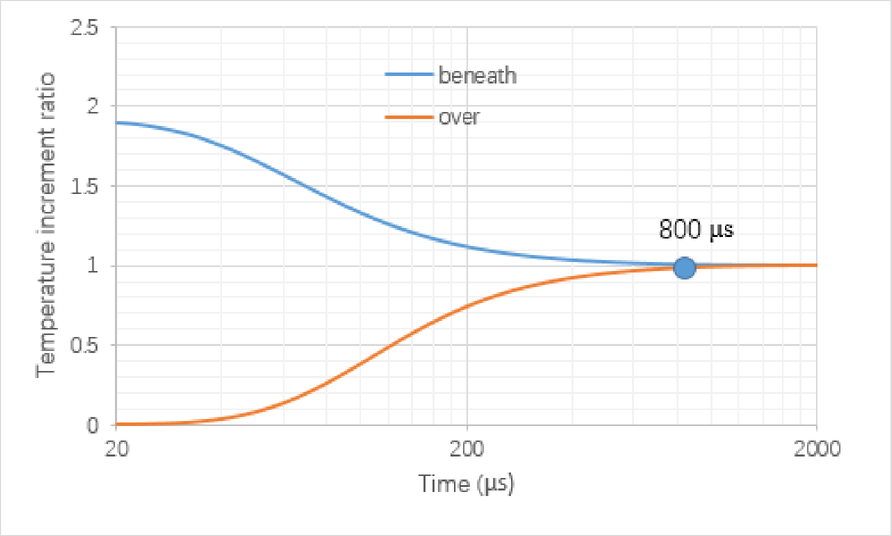

Figure 5.13 Ratio of the temperature increment over and beneath the defect to that of the sound area.

### 5.3.4 Identification of the Defect Radius by the Surface Temperature Gradient

Figure 5.14 shows the simulated surface temperature and temperature gradient along the radius direction of the model at t=170 μs. The temperature increases from r=0 μm to r=100 μm and then gradually flattens. The lower temperature region provides the approximate position of the defect but does not allow for the determination of a particular radius of the defect. However, Figure 5.15 shows that if the temperature gradient is analysed, the peak of the temperature gradient is found near the defect edge position. The maximum of the temperature gradient clearly varies with heating time, while the radius of the peak is almost the same.

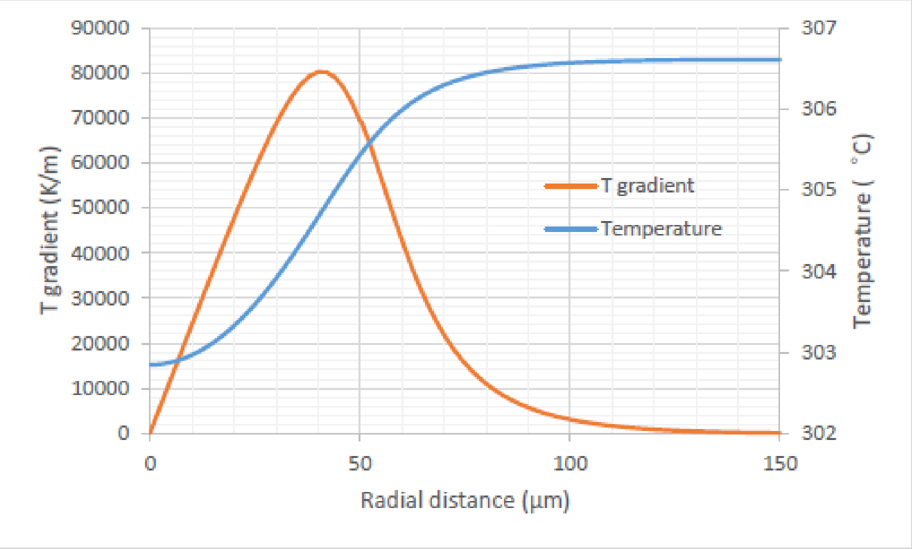

Figure 5.14 Surface temperature and temperature gradient at 170 μs.

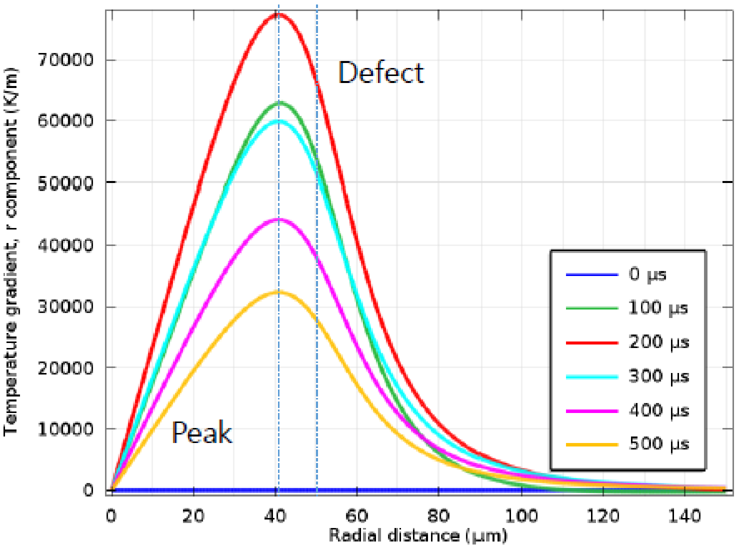

Figure 5.15 Surface temperature gradient radial distance versus radius at different times.

The COMSOL software presents 3/4 of the 3D model by rotation of the 2D axisymmetric model. Figure 5.16 compares the x-y image of the predicted surface temperature and peak of the surface temperature gradient. The black circle shows the defect edge. Figure 5.16 (a) shows a circular lower temperature area with a fuzzy edge near the defect edge, while Figure 5.16 (b) shows a smaller and clearer circle near the defect edge, denoting the position of the defect.

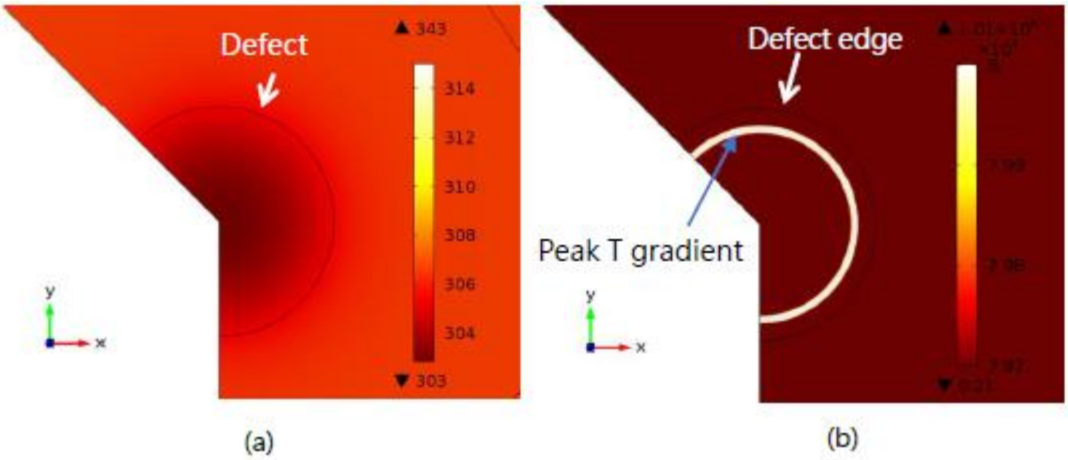

Figure 5.16 Images of the (a) surface temperature and (b) relative temperature gradient of a 50 μm-radius defect after 170 μs.

Figure 5.17 shows the temperature gradient versus the radius of the defect, ranging from 20 μm to 200 μm, at time t=170 μs. Each radius predicted from the peak of the temperature gradient is slightly smaller than that of the corresponding defect edge location, and the smaller distance is approximately half the thickness of the film. Figure 5.18 shows that the location of the peak of the temperature gradient gives the same radius over time, from 100 μs to 200 μs.

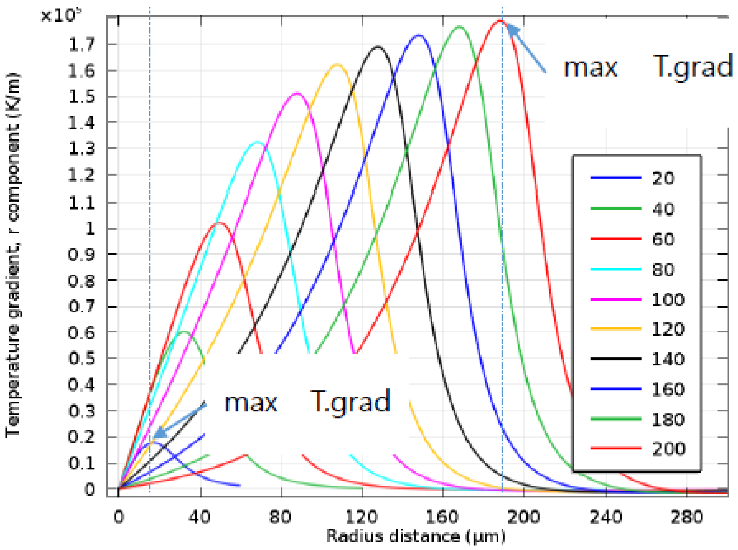

Figure 5.17 Temperature gradient versus defect radius from 20 µm to 200 µm.

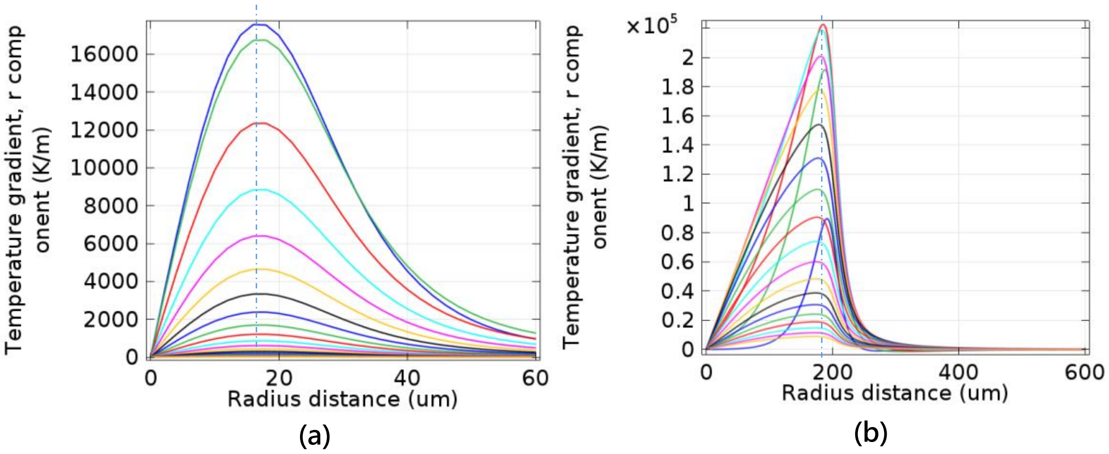

Figure 5.18 Temperature gradient of (a) a 20 µm-radius defect and (b) a 200 µm-radius defect for times of 100 µs to 2000 µs.

However, in this model, the thickness of the film is 20 µm, which is much smaller than the diameter of the defect. The heat transfer route in the film above the defect is nearly parallel to the interface and surface of the film because the thermal resistance of the Ni film is much less than that of the interface between the film and the external environment. When the diameter of the defect is close to the thickness of the film, the sound surface near the defect receives less energy. The surface temperature around the defect is less than that far away from the defect. Meanwhile, the temperature difference decreases, and the maximum temperature gradient moves to the sound area. Figure 5.19

shows an image of the temperature gradient of the model with a 50 µm-radius defect and a 100 µm-thick film. The radius of the peak temperature gradient is larger than the radius of the defect.

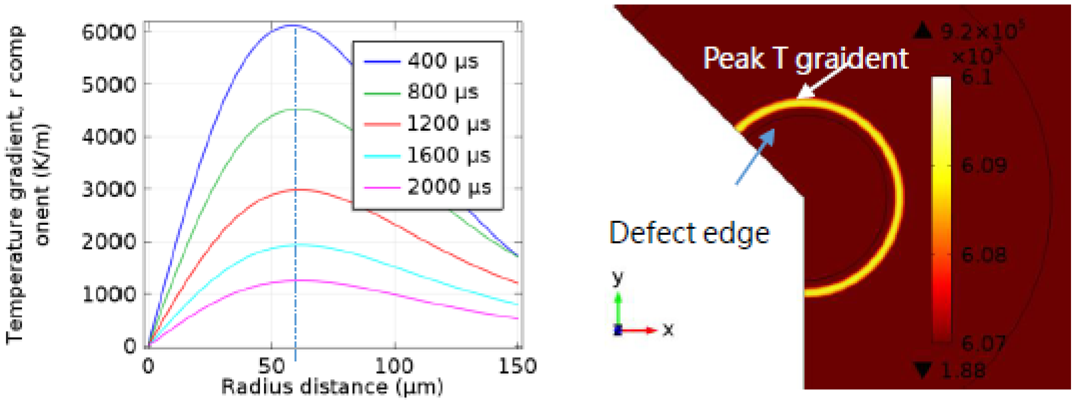

(a) (b)

Figure 5.19 (a) Temperature gradient of a 50 µm-radius defect and 100 µm-thick film at times of 400 µs to 2000 µs and (b) the image of the relative temperature gradient at 400 µs.

### 5.3.5 Maximum Temperature Difference

I. Constant heating temperature

An important parameter in thermographic NDT is the heating temperature. If the temperature is too large, the specimen will be destroyed, while if the temperature is too small, a relatively small temperature difference will be obtained, making it difficult for the thermal detector to distinguish regions of different temperature. Thus, the effect of the heating temperature on the surface temperature difference is discussed in this section.

In Figure 5.20, the temperature difference response resulting from heating temperature increments (ΔT) of 20 °C, 50 °C, 80 °C and 110 °C shows that the temperature difference is proportional to the heating increment, while the time at which the maximum temperature difference occurs is almost the same at t=170 µs. The surface temperature difference is promotional to the temperature increment. Therefore, the higher the applied temperature increment, the larger the obtained temperature difference. However, Figure 5.21 shows that the relative detectability is the same at temperature increments of 50 °C, 80 °C and 110 °C. The relative detectability at ΔT=20 °C is larger before the peak time of t=170 µs due to the very small temperature increment of both $T_{dc}$ and $T_s$, and the small change in the reference temperature makes the contrast of the defect temperature less obvious. Thus, too small of a temperate increment decreases the detectability.

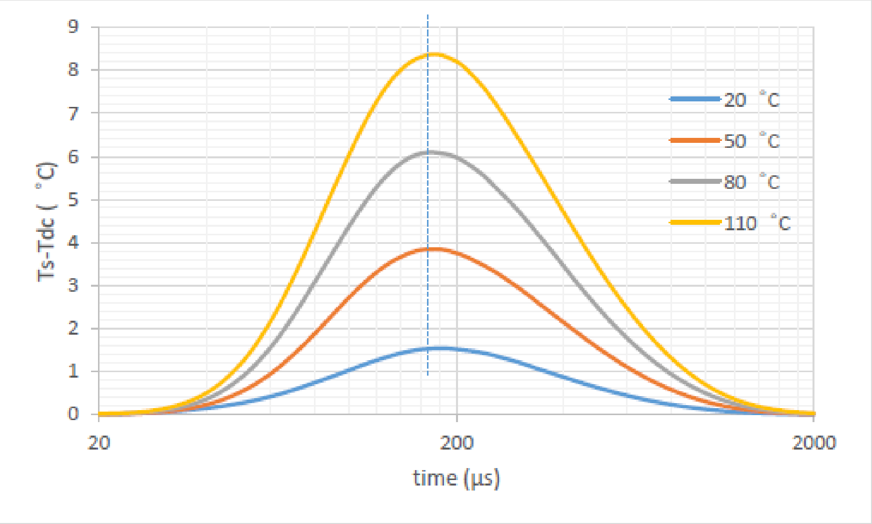

Figure 5.20 Temperature difference over time for various heating temperature increments of 20 °C, 40 °C, 80 °C and 100 °C.

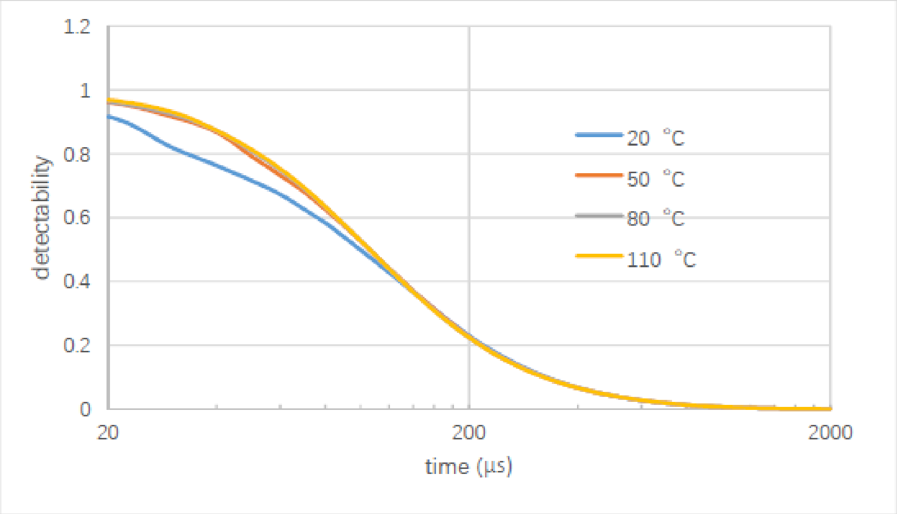

Figure 5.21 Relative detectability over time for temperature increments of 20 °C, 50 °C, 80 °C and 110 °C.

II. Thickness of the film and substrate

The defect depth can be detected by NDT. In this model, the defect depth is equal to the thickness of the film. Figure 5.22 shows the temperature difference over time for the film thicknesses ranging from 1 μm to 20 μm. Figure 5.23 displays the relationship of the film thickness to the maximum temperature difference and peak time. The temperature difference increases more quickly and reaches a higher peak value when the film is thinner. However, the increase in the temperature difference and rate is not proportional to the increase in the thickness, because when the thickness is less than a particular value, it can be seen as an extremely thin film whose thickness can be ignored. However, the relative detectability curves cross many times before 200 μs, and it is difficult to determine which film gives a better result. After 200 μs, the thinner film shows a worse relative detectability than that of the thicker film (Figure 5.24), possibly because the thickness of the film does not greatly influence the temperature difference, the values of which fall between 3.7-4.7 °C, while the surface temperature of thinner films increases faster, which indicates that the temperature increment is larger. In conclusion, the thinner film shows an improved temperature difference but not an obviously better detectability.

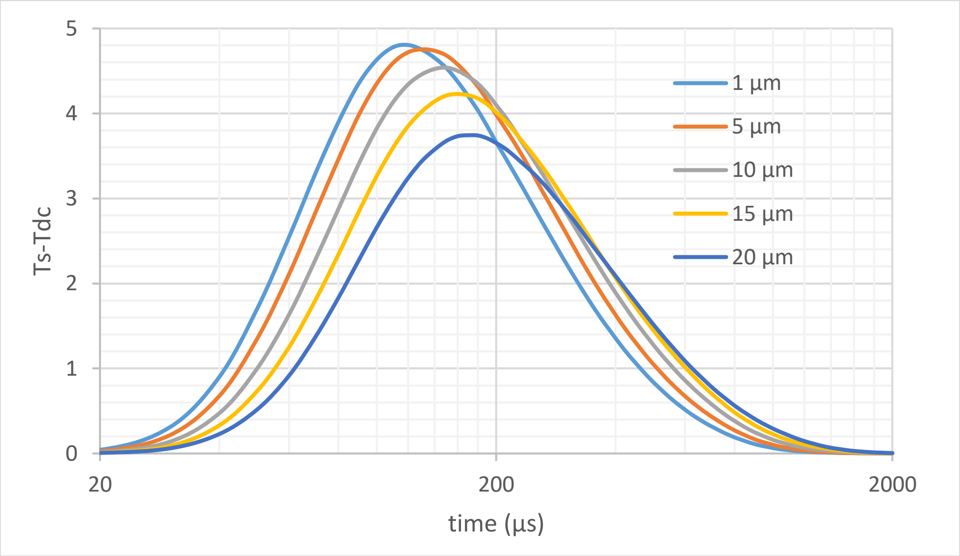

Figure 5.22 Temperature difference over time for various film thicknesses.

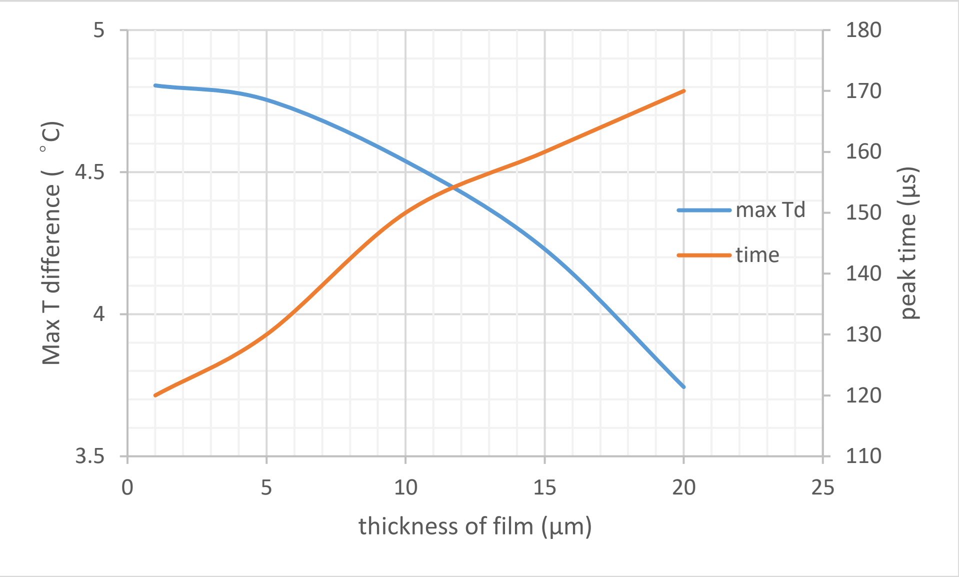

Figure 5.23 Maximum temperature difference and peak time as a function of film thickness.

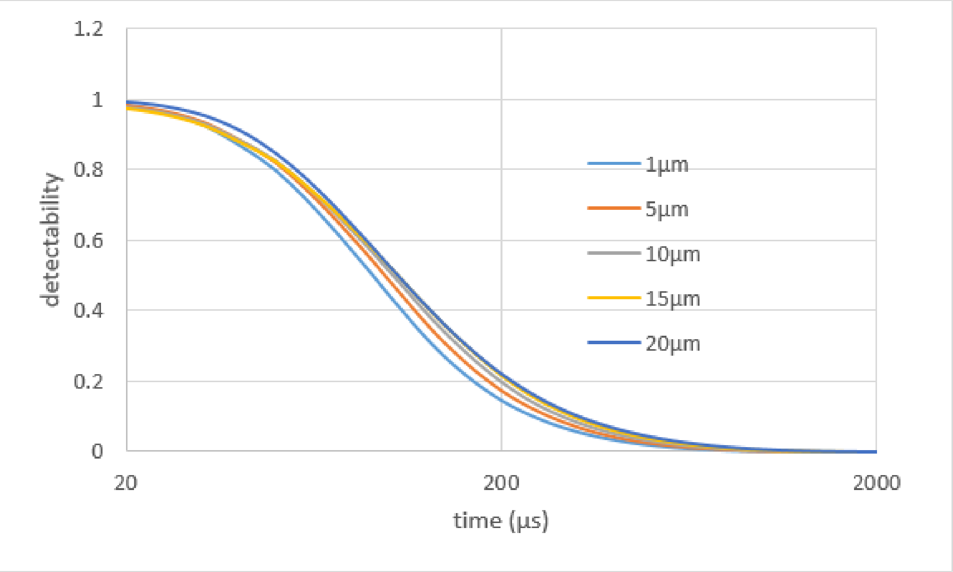

Figure 5.24 Detectability over time for various film thicknesses.

As mentioned in Chapter 5, most thermographic research has not considered the thickness of the substrate as a factor that influences the detectability. However, for detection in transmission mode, the thickness of the substrate is a key factor to determine the heating time and amount of heat energy after arriving at the defect.

Similar to the plot of the film thickness, Figure 5.25 shows the temperature difference over time for substrates with thicknesses ranging from 50 μm to 200 μm. The thinner substrate provides a larger and faster temperature difference for detection because the reduced thickness affords a shorter route for heat transfer and reduces the time required to heat the model. However, as shown in Figure 5.26, the thinner substrate has a lower detectability than the other substrates. Figure 5.27 shows that the maximum temperature difference and peak time have a similar relations to the substrate thickness compared with that of the film thickness.

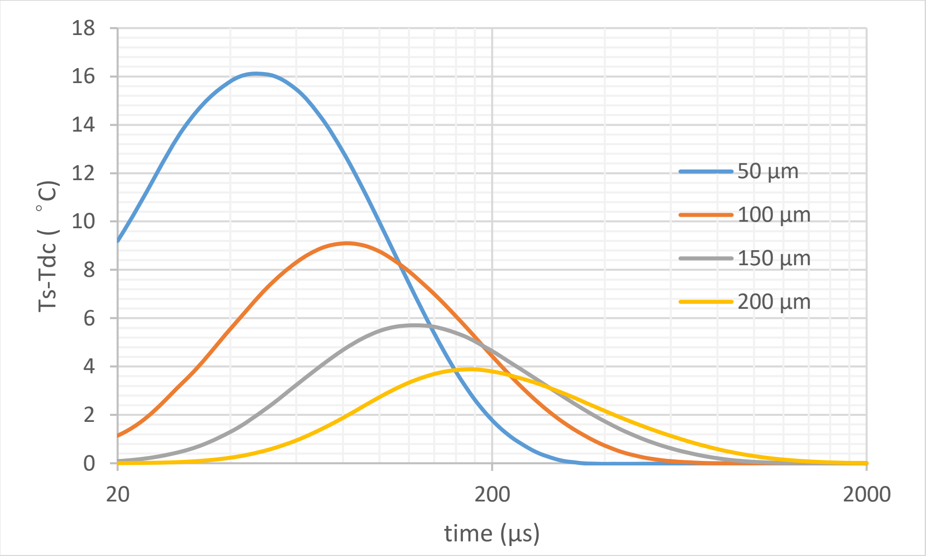

Figure 5.25 Temperature difference over time for various substrate thicknesses.

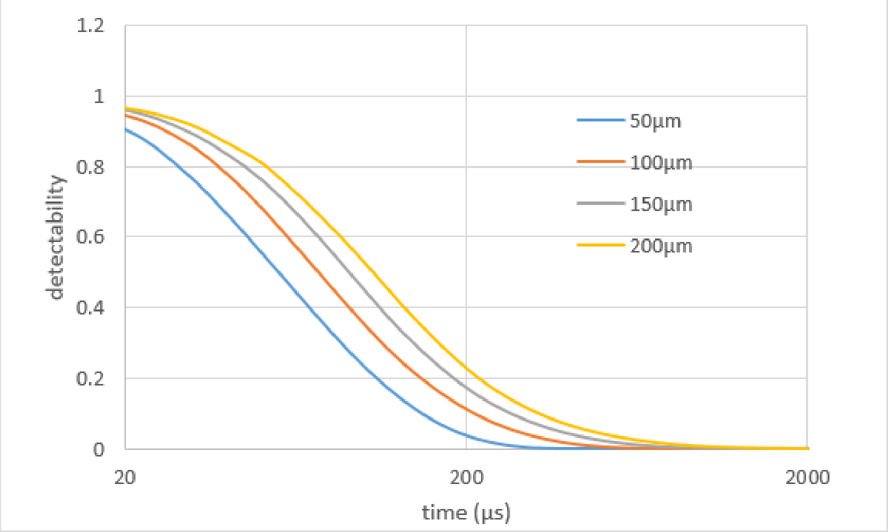

Figure 5.26 Detectability over time for various substrate thicknesses.

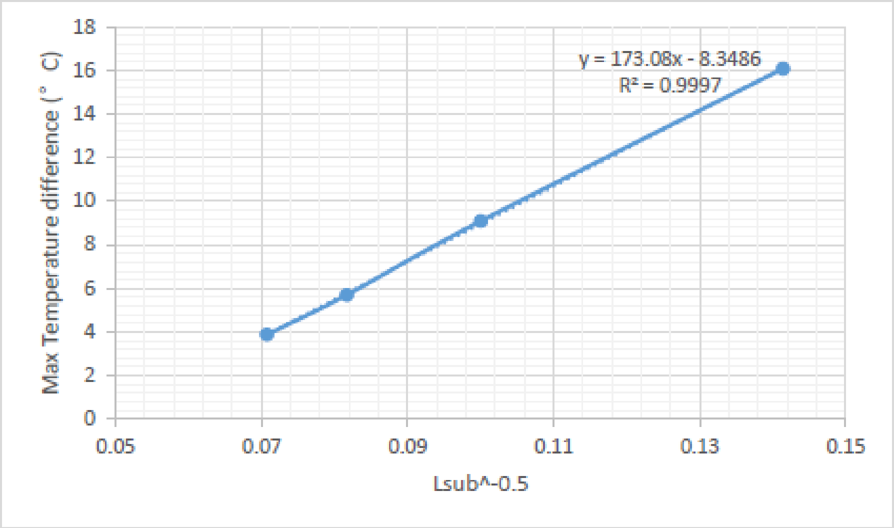

Figure 5.27 Maximum temperature difference and peak time as a function of substrate thickness.

III. Radius of the detect

As discussed in Chapter 4, the time required for the heat energy to reach the centre of the defect is longer than that to reach the sound area, because the radius of the defect increases the heat transfer path to a certain extent. Thus, a larger defect leads to a higher maximum temperature difference and a later peak time, as shown in the simulation results presented in Figure 5.28.

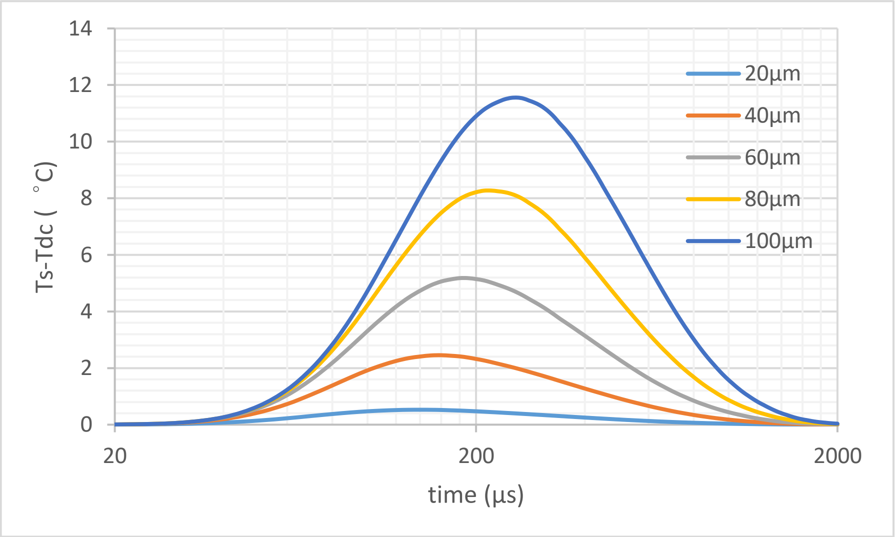

Figure 5.28 Temperature difference over time for various defect radii.

### 5.3.6 Effects of the Thermal Properties of the Material

The last section discussed structural factors such as the defect depth, the substrate thicknesses, and the defect radius. These factors influence the detectability in transmission thermographic NDT. Because the interface temperature dynamically changes with the thermal capacity and thermal conductivity, to simplify the calculation, we focus on the parameter $\alpha = k/\rho c$. This section examines the influence of the thermal diffusivity on the temperature distribution on the surface and the maximum achievable temperature difference, as well as the time it takes to achieve this difference.

I. Substrate material

Because thermal-based defect detection methods are reliant on heat diffusion in solid materials, devices containing different materials can be expected to present different surface temperature response profiles. This study demonstrates the applicability of pulse heating tests for several typical substrate and film materials, such as aluminium nitride (AlN), sapphire, aluminium, etc.

Although silicon (Si) is the most commonly adopted semiconductor material for use as a substrate in the microelectronics industry, some alternatives have been proposed. Silicon carbide (SiC) is a mature wide-bandgap semiconductor material, comparable with other wide-bandgap materials, and has a number of advantages, including the commercial availability of the substrates, known device processing techniques, and the ability to grow thermal oxides. In contrast to silicon, SiC contains a higher thermal conductivity [163]. Thus, SiC will present a different temperature distribution in thermographic NDT than silicon. Another substrate material with high thermal conductivity is polycrystalline AlN, which is a ceramic material primarily used for high-power device packaging. An aluminium (Al) substrate is commonly used in LED packaging and high-density three-dimensional packaging [164]. Sapphire ($Al_2O_3$) is also widely used as substrate material for LEDs and LDs [165]. High-power module packaging consisting of an iron (Fe) core substrate has been utilized due to its high thermal conductivity and low cost [166]. Table 5.4 lists the thermophysical characteristics and relative thermal diffusivities of these six typical substrate materials.

Table 5.4 Thermal characteristics of typical substrate materials for MEMS devices [167].

| **Material** | **Heat capacity (J/kg·K)** | **Thermal conductivity (W/m·K)** | **Density (kg/m$^3$)** | **Thermal diffusivity (m$^2$/s)** |
|---|---|---|---|---|
| **Sapphire** | 782 | 24 | 3980 | $7.71\times10^{-6}$ |
| **Fe** | 449 | 80.2 | 7860 | $2.27\times10^{-5}$ |
| **Silicon** | 700 | 130 | 2329 | $7.97\times10^{-5}$ |
| **Al** | 904 | 237 | 2700 | $9.7\times10^{-5}$ |
| **AlN** | 719.6 | 297.8 | 3240 | $1.28\times10^{-4}$ |
| **6H-SiC** | 690 | 490 | 3216 | $2.21\times10^{-4}$ |

The influence of the substrate material on the maximum temperature difference predicted by the simulation is shown in Figure 5.29. The model with higher thermal diffusivity presents a relatively large temperature difference and also achieves this maximum temperature difference earlier than the lower diffusivity model. The reason for this enhancement is that heat energy diffuses quickly in high diffusivity materials and thus decreases the time it takes to travel the same diffusive distance. In contrast, the temperature difference in the low-diffusivity substrates is much smaller, and more time is required to reach the maximum temperature difference. The influence of the higher thermal diffusivity substrate material is similar to that of the thinner substrate (for comparison, see Figure 5.25).

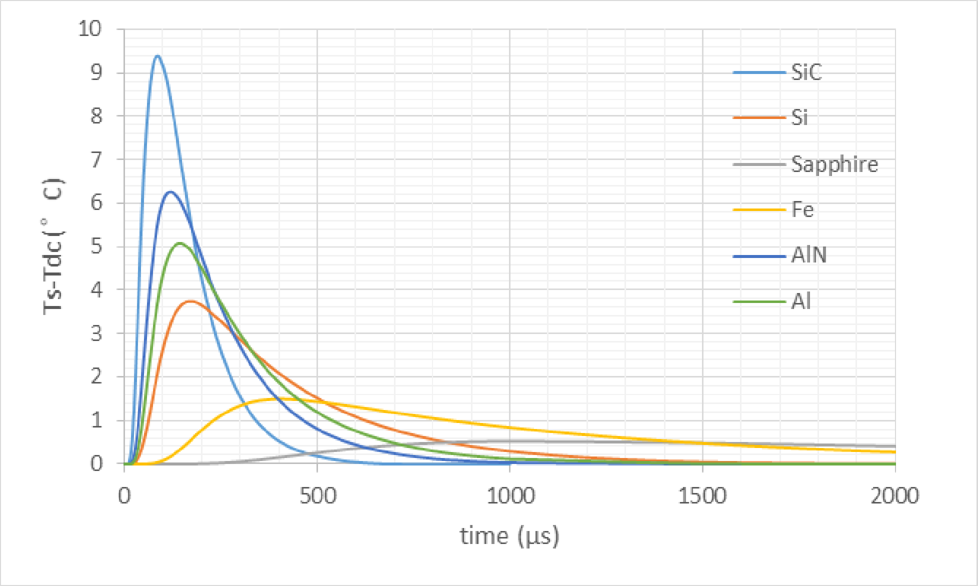

Figure 5.29 Predicted surface temperature difference for Si, SiC, Al, sapphire, AlN and Fe substrates.

Figure 5.30 shows the surface temperature profiles of the models of the five substrates over time for five points from t=0 μs to the peak time. These profiles reveal the temperature changes from the initial uniform condition to that at the time of maximum temperature difference at both the defect and non-damaged areas. Over a fixed temperature range, all the temperature profiles are nearly flat at the initial time, and then, the surface temperature of the non-damaged area greatly increases, while that of the defect area increases much more slowly. Overall, as time passes, the surface temperature profile of the non-damaged area increases slightly faster than that of the defect area until the difference reaches the maximum.

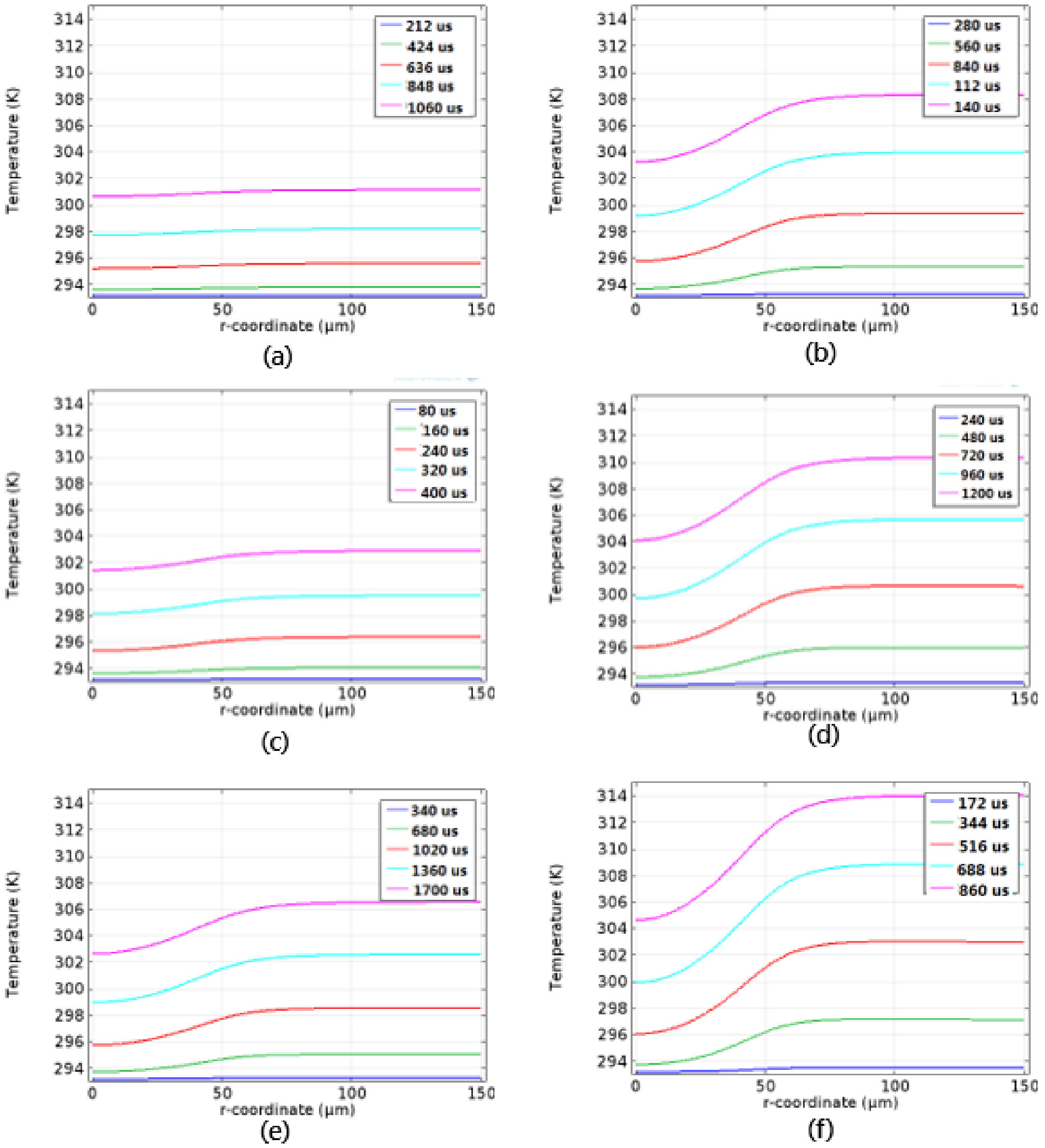

(a) (b) (c) (d) (e) (f)

Figure 5.30 Predicted surface temperature profiles for (a) sapphire, (b) Al, (c) Fe, (d) AlN, (e) Si and (f) SiC substrates at each peak time.

However, energy transfer through the samples with Al, AlN and SiC substrates leads to the evident curvature of each curve at peak time, while the temperature lines of the sapphire and Fe substrates are almost straight, even at the peak time. For low thermal conductivity materials, the rate of the temperature increase at the defect area is virtually equal to that at the non-damaged area. Thus, the time of maximum temperature difference occurs when the growth rates of $T_{dc}$ and $T_s$ are equal. In the temporal processing of the temperature by differentiation over time, the peak time satisfies the equation as follows:

$$\frac{dT_s}{dt} - \frac{dT_{dc}}{dt} = 0 \tag{5. 6}$$

Since measurement in actual detection focuses on the change in temperature at each point, the equation is written as the time derivative of the temperature at each point, rather than the temperature difference.

The speed of surface temperature diffusion is defined by the properties of the material and the geometry of the structure. During heat transfer, the substrate acts as a thermal resistor and thermal capacitor, and a large amount of heat energy is required to heat a substrate composed of a low thermal diffusivity material, which leads to the film obtaining less energy and having a lower heat flux. The heat flux varies with the thermal potential difference between the top surface and the interface, when the thermal resistance of the film is constant. Meanwhile, the thermal capacitor in the system is ‘charged’ over a period of time, which increases the temperature of the substrate. This ‘charging’ period delays the time to reach the maximum temperature difference.

In summary, Figure 5.31 shows the achievable maximum temperature difference of nickel films on various substrates. The higher the thermal diffusion, the larger the possible maximum temperature difference of the specimen.

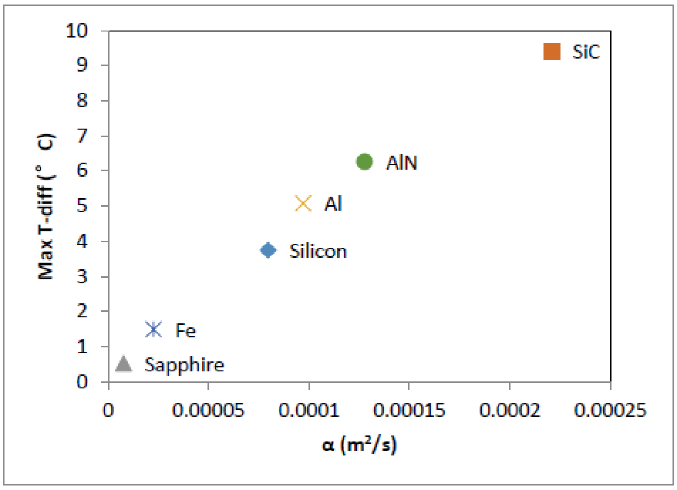

Figure 5.31 Maximum temperature difference versus the thermal diffusivity of various substrate

materials.

II. Thin-film material

The thermal properties of the thin-film material also influence the response, when the substrate material and geometry are constant. Table 5.5 lists some of the materials often used in thin-film manufacturing [167, 168, 169]. The result of heating a sample from the bottom in 50 °C increments is shown in Figure 5.32. Because the temperature difference and duration are much larger than that of higher diffusivity materials, the coordinates are plotted on a log scale. Metal materials such as silver (Ag), copper (Cu) and Al are good conductors of heat. Heat transfers very fast in specimens containing these types of materials, and thus, the surface temperature reaches the heating temperature very quickly, not leaving much time for measurement by the detector. The maximum temperature difference will be reached more quickly, and the temperature difference will be reduced.

Table 5.5 Thermal characteristics of typical thin film materials for MEMS [167].

| **Material** | **Heat capacity (J/kg·K)** | **Thermal conductivity (W/m·K)** | **Density (kg/m$^3$)** | **Thermal diffusivity (m$^2$/s)** |
|---|---|---|---|---|
| **Nickel** | 445 | 90.7 | 8900 | $2.29\times10^{-5}$ |
| **Copper** | 384 | 401 | 8960 | $1.16\times10^{-5}$ |
| **Teflon** | 1050 | 0.35 | 2200 | $1.51\times10^{-7}$ |
| **NiCr Alloy** | 444 | 12.6 | 8314 | $3.41\times10^{-6}$ |
| **Al** | 904 | 237 | 2700 | $9.71\times10^{-5}$ |
| **Ag** | 235 | 429 | 10500 | $1.74\times10^{-4}$ |

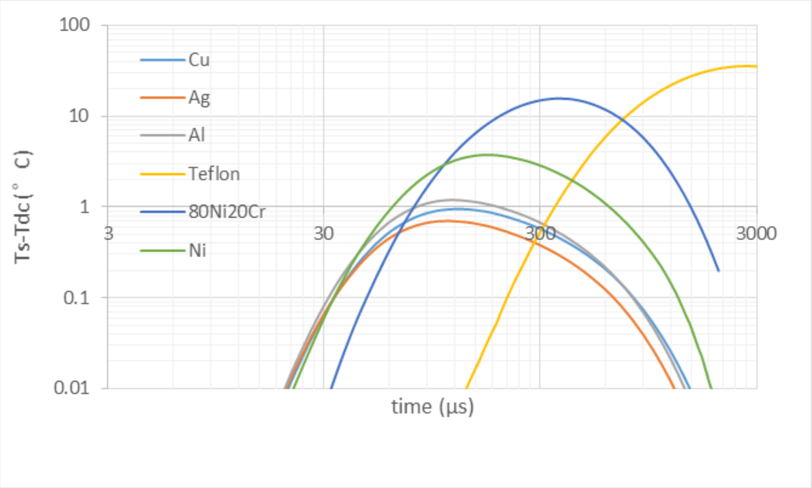

Figure 5.32 Predicted temperature difference for Ag, Al, Cu, Ni, 80Ni20Cr and Teflon thin films.

Figure 5.33 shows the surface temperature distribution of these film materials over time, from the initial conditions to the time at which the maximum temperature difference occurs. Because the temperature of lower diffusivity materials is much larger than that of higher diffusivity materials, these two materials have different temperature scales.

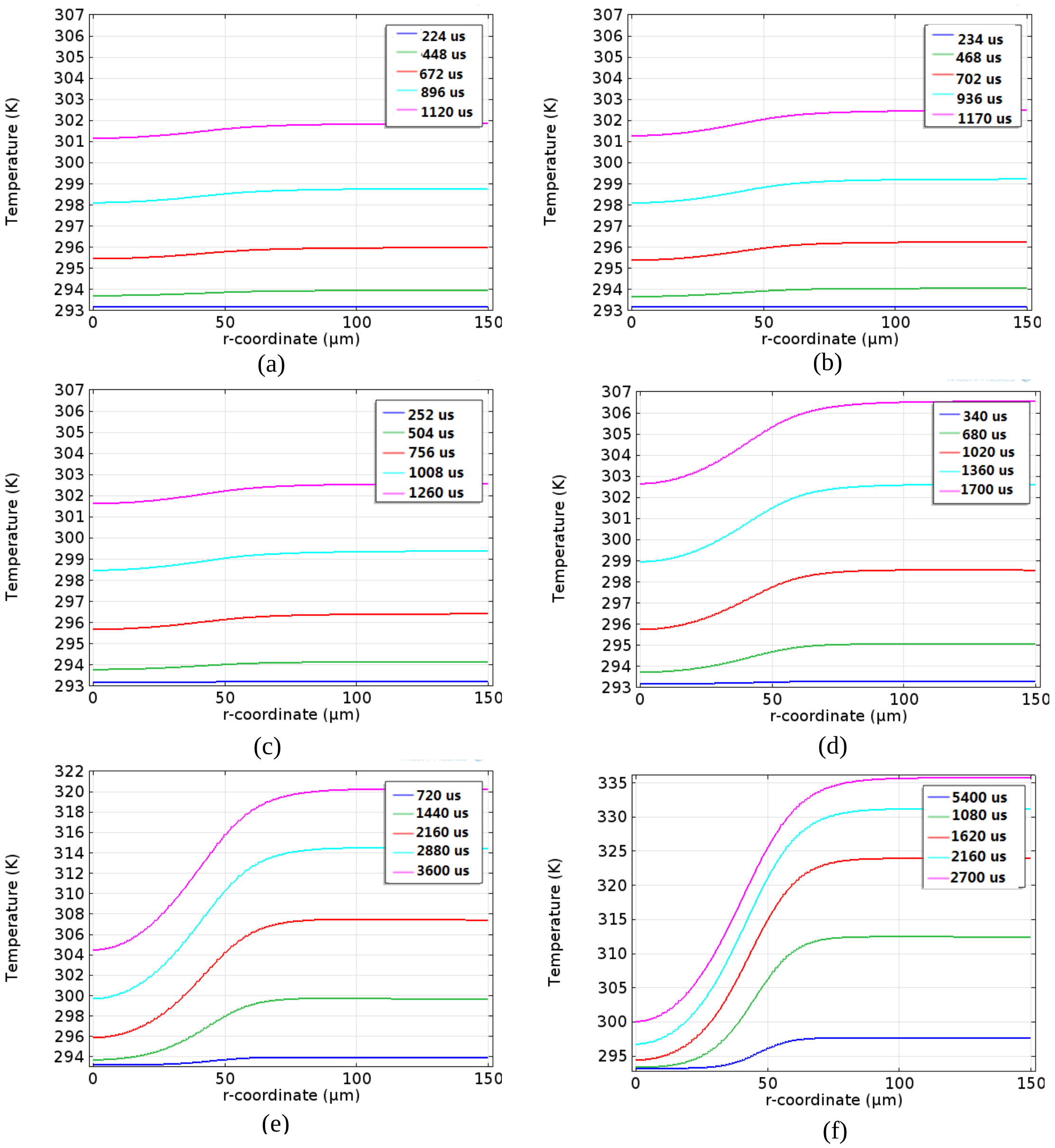

(a) (b) (c) (d) (e) (f)

Figure 5.33 Surface temperature line profiles of models with (a) Ag, (b) Al, (c) Cu, (d) Ni, (e) 80Ni20Cr and (f) Teflon thin films at each peak time.

The parameter $\sqrt{\alpha t_{peak}}$ is typically used to describe the thermal diffusion of a material that presents a temperature difference at points in a half infinite plate. This parameter is chosen to represent the relations among the maximum temperature difference, the thermal diffusivity of a material (α) and the peak time ($t_{peak}$). Figure 5.34 illustrates that the maximum temperature difference is almost linearly proportional to the reciprocal of $\sqrt{\alpha t_{peak}}$. On the other hand, the thermal diffusivity characterizes the homogenization speed of the temperature in a solid. For a film with asymmetry mainly in the horizontal direction, the homogenization speed on a horizontal surface depends on the film material. In contrast, the substrate, as an infinite plane, shows an asymmetrical temperature distribution in the vertical direction. Large thermal diffusivity leads to small temperature homogenization speeds and slow temperature heating at the interface of the sample, which weakens the shock effect. In conclusion, a substrate with higher thermal diffusivity develops a larger temperature difference, and the peak time occurs earlier. Meanwhile, a lower thermal diffusivity film results in a larger temperature difference and later peak time.

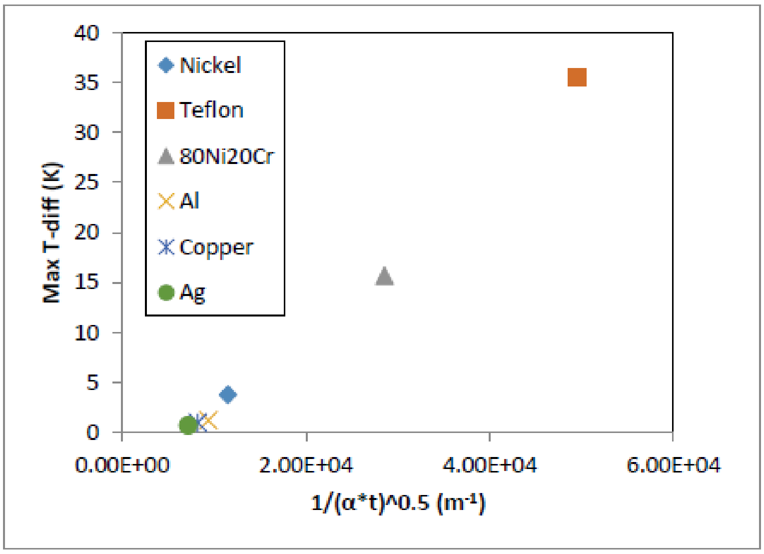

Figure 5.34 Maximum temperature difference versus the thermal diffusivity of various film materials.

## 5.4 Analysis of the Model Heated by Constant Heat Flux

### 5.4.1 Limitation of Constant Heat Flux and Heating Duration

Heating a sample at constant heat flux is not an appropriate method, as the very high temperatures induced by extended heating periods may damage the sample or even destroy it. Therefore, the heat flux and heating duration should be carefully selected to achieve the largest temperature difference without causing damage during measurement.

Because the seed layer is much thinner than that of the silicon substrate and nickel film, the energy Q required to uniformly increase the entire specimen by 50 °C can be roughly calculated by considering only the silicon substrate and nickel metal film in the product of the temperature increment, specific thermal capacity, density and volume of the materials:

$$Q = \Delta T c_p \rho V \tag{5. 7}$$

Thus, the total energy required to heat silicon and nickel is 0.127 J, according to Equation (5.2):

$$Q = \Delta T \frac{1}{2}\pi \times radius^2 \times (c_{pSi}\rho_{Si}L_{sub} + c_{pNi}\rho_{Ni}L_{film}) \tag{5. 8}$$

Heat flux is defined as the rate of heat energy transfer through a given surface per unit time. Therefore, the relationship between the heating duration and the heat flux is:

$$q_0 = \frac{Q}{A \times t} = \frac{1}{t} 2.03 \times 10^4 J/m^2 \tag{5. 9}$$

Considering the time over which this transfer occurs, according to the calculation in Chapter 4, the heating time when applying a constant heat flux should be less than 2 ms. Therefore, to increase the temperature of the specimen by 50 °C, the bottom surface of the sample should be supplied with a constant uniform heat flux of approximately $q_0 = 10\ MW/m^2$.

However, due to convection cooling on the upper surface, some of the heat is lost from the specimen, and the longer the heating period, the more energy is lost. The convection cooling rate is related to the difference between the surface and external temperature, which changes during heating. Therefore, to achieve a temperature difference, various constant heat fluxes 10 $MW/m^2$, 20 $MW/m^2$, 30 $MW/m^2$ and 40 $MW/m^2$ are applied on the bottom surface for a duration of 2 ms in the simulation. Also, the bottom temperature increment during heating will be considered to protect the specimens from damage.

Figure 5.35 presents the predicted centre bottom temperatures of the specimen at different constant heat fluxes. Because the heat flux is over the entire bottom of the specimen and cooling convection occurs at the side boundaries, the bottom temperature at the edge of the specimen is lower than that at the centre. Since we are more interested in the maximum temperature, the bottom temperature $T_b$ discussed in this section is the centre bottom temperature. Due to the rapid temperature response on the bottom surface, the bottom temperature undergoes a short period of sharp increase and then increases linearly. The $10\ MW/m^2$ temperature curve reaches 75 °C in 2 ms, which is higher than the 70 °C calculated for the entire body, but the system will rapidly cool when the heat is cut off. However, one additional factor to consider is the time at which the peak surface temperature difference occurs.

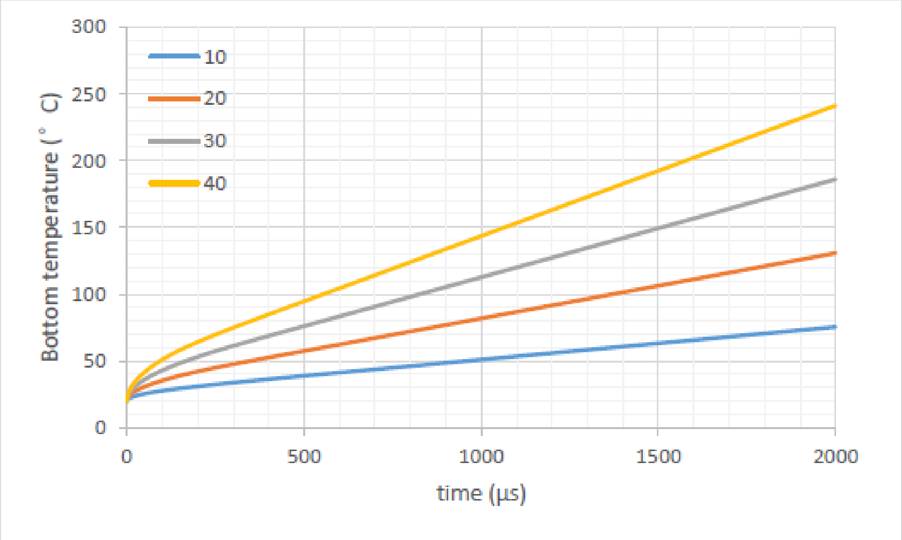

Figure 5.35 Temperature at the centre of the bottom surface for constant heat fluxes of 10, 20, 30 and 40 MW/m$^2$.

Figure 5.36 reveals the change in the temperature difference of the upper surface over the defect centre and the non-damaged area over time. The difference in the surface temperature for $40\ MW/m^2$ heat flux excitation is nearly 4 times higher of that of $10\ MW/m^2$, after reaching the largest value. Figure 5.37 shows that before t=500 μs, larger heat flux provides the best detectability. Therefore, enlarging the heat flux is an effective method to increase the temperature difference.

Additionally, because of the time delay for heat to transfer through the thick substrate, the surface temperature difference is zero in the first few microseconds. After that, the temperature difference sharply increases until reaching a constant value after approximately 500 µs. This time is dependent on the heat transmission distance and propagation speed but not on the heat flux.

However, according to the definition of detectability, a higher surface temperature with the same temperature difference will decrease the sensitivity of temperature detection. Thus, to achieve a large temperature difference, 500 µs is suitable for the heating duration. Meanwhile, stopping the heating before the sample reaches high temperatures protects the specimen from damage. For example, if the temperature limit of the bottom surface of the specimen is 100 °C, the heating duration for heat fluxes of $20\ MW/m^2$, $30\ MW/m^2$ and $40\ MW/m^2$ must be less than 1500 µs, 600 µs and 500 µs, respectively. Thus a $40\ MW/m^2$ heat flux for 500 µs will provide the best defect detection.

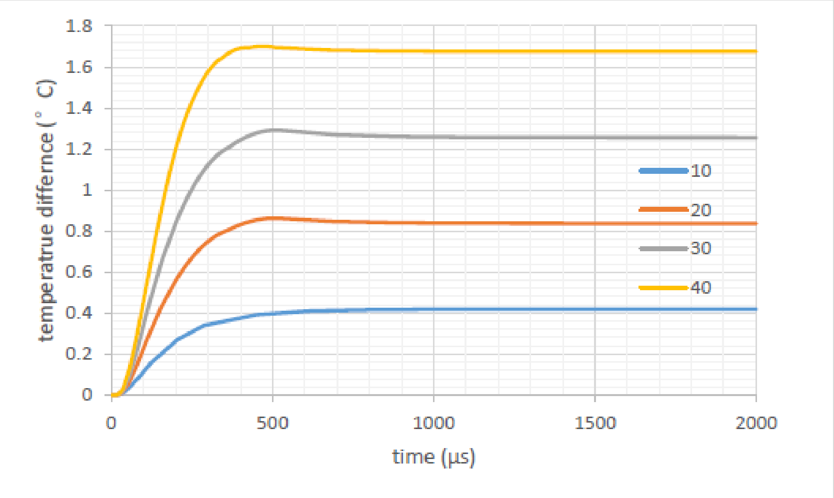

Figure 5.36 Temperature differences between $T_s$ and $T_{dc}$ of a specimen heated at constant heat fluxes of 10, 20, 30 and 40 MW/$m^2$.

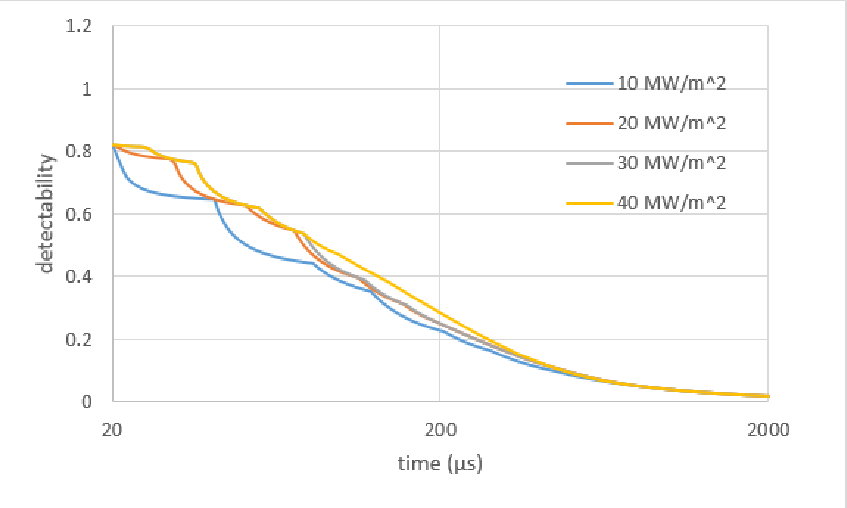

Figure 5.37 Detectability over time using heat fluxes of 10, 20, 30 and 40 MW/m$^2$.

The pulse width for heating the specimen with a $40\ MW/m^2$ heat flux was therefore set to 500 µs in the following simulations. As shown in Figure 5.38, the bottom temperature $T_b$ quickly increases during the heating duration as expected until reaching 94.29 °C (367.44 K, $\Delta T_b$=74.29 °C) and then drops sharply after heating is stopped until reaching an approximately stable value at 70 °C ($\Delta T$=50 °C), which then slowly decreases to room temperature. The top surface temperatures over the defect centre $T_{dc}$ and the non-damage area $T_s$ increase in a similar manner to those in the constant heating temperature method, but in fact, the temperature difference curve shows that there is a 150 µs period of a maximum temperature difference of 3.3 °C. Meanwhile, the temperature difference starts to decline at 60 µs after heating is stopped. Because there is a time delay between the bottom and top surface temperature, when the surface temperature profile achieves a constant increasing slope, the temperature difference remains invariant. In addition, a time delay exists between the heating cut-off and the decrease in temperature difference. Although the maximum surface temperature difference is 0.4 °C smaller than that in the constant temperature heating method, which shows a peak value of 3.7 °C, the time over which a large temperature difference can be observed is much longer for the constant flux heating method.

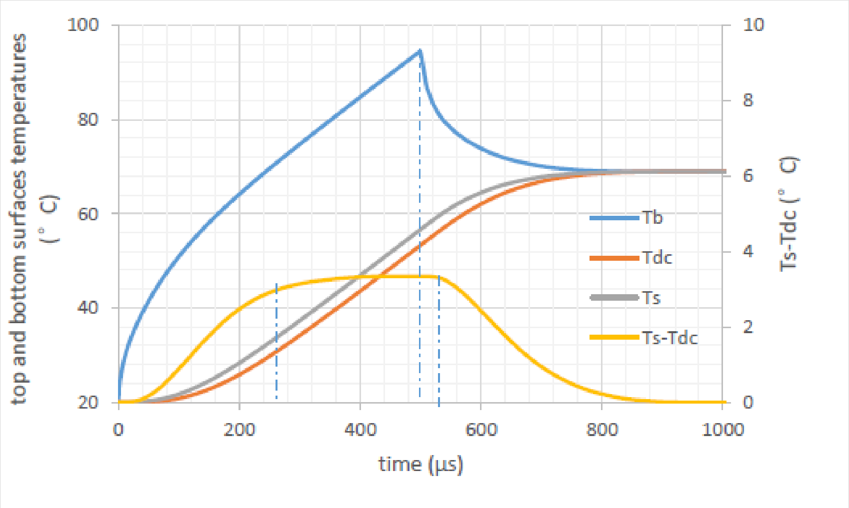

Figure 5.38 Top and bottom surface temperature profiles and changes in the surface temperature difference over the defect centre and non-damaged area over time.

## 5.4.2 Temperature Response and Limitations

Although thermal cameras are sensitive to temperature differences as low as 0.1 °C (sometimes 0.01 °C), noise exists in the experiment. Vibration of the equipment, surface roughness and environmental temperature changes can increase the temperature noise. Therefore, reducing the influence of noise requires large temperature differences and long observation times. Therefore, increasing the heat flux and reducing the heating duration can lead to greater temperature differences and prevent the surface temperature from exceeding safe limits. The ten temperature curves in Figure 5.39 indicate that the bottom temperature increases quickly. The heat flux on the bottom ranges from 50 $MW/m^2$ to 500 $MW/m^2$. The heating duration limit can be defined from this plot when the heat flux and the maximum temperature of the bottom are fixed, in order to protect the specimen from being destroyed at excessive temperatures. For example, Figure 5.40 gives the longest heating durations for various constant heat fluxes when the maximum temperature of the specimen bottom is 400 K. Although a larger constant heat flux will induce a larger temperature difference, the suitable heating period will be greatly reduced. For example, when the heat flux is larger than 400 $MW/m^2$, the pulse power must be stopped after only 12 µs, which is difficult to achieve using typical excitation sources for thermographic NDT, such as xenon flash or lasers, and difficult for thermal detectors to observe.

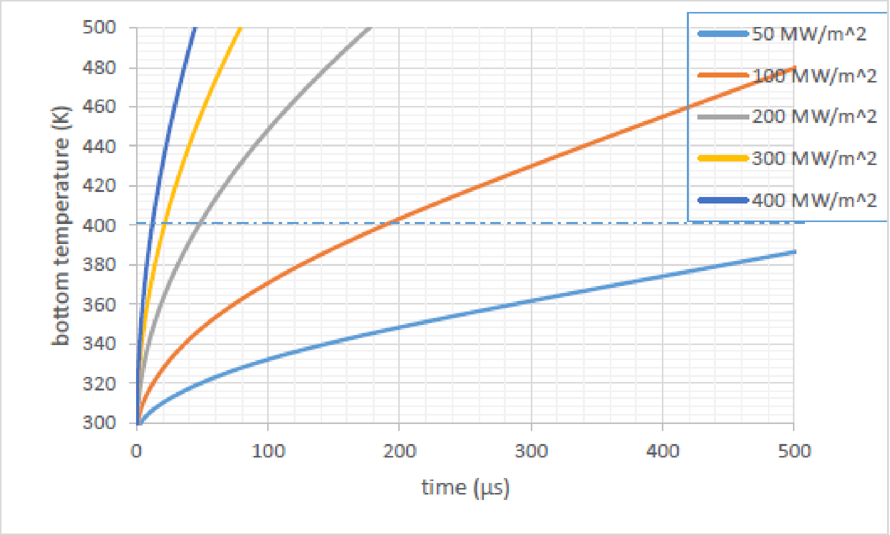

Figure 5.39 Bottom surface temperature plots for constant heat fluxes ranging from 50 to 400 MW/m$^2$.

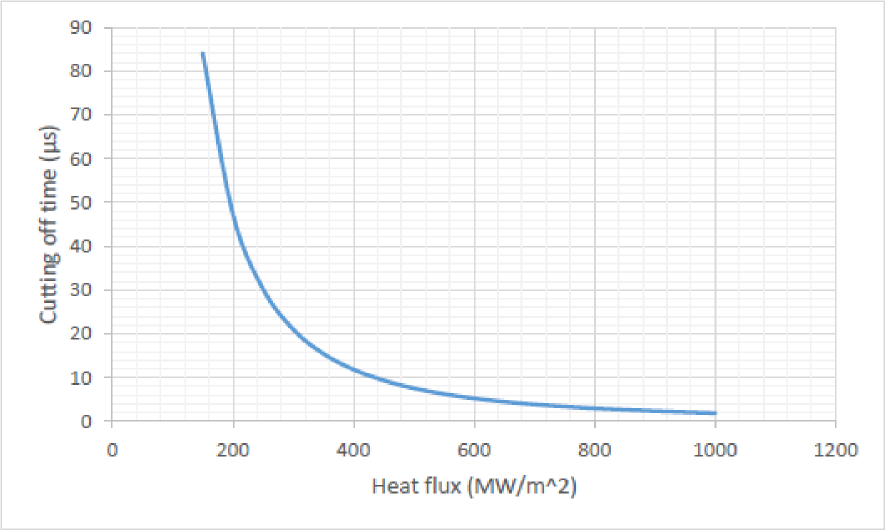

Figure 5.40 Maximum heating duration with various constant heat fluxes for a specimen that can withstand a bottom temperature of 400 K.

Figure 5.41 shows the change in the surface temperature difference stimulated with different heat fluxes ranging from 50 MW/m$^2$ to 200 MW/m$^2$. If 400 K is the bottom temperature limit, the heating cut-off time is 600 µs, 400 µs, 84 µs and 47 µs, depending on the heat flux. Because the maximum heating period mainly occurs between 1 and 100 µs, the maximum temperature difference is less than 6 °C for heat fluxes between 150 MW/m$^2$ and 200 MW/m$^2$. Therefore, increasing the heat flux significantly limits the possibility of enhancing the temperature difference when the maximum bottom temperature is fixed.

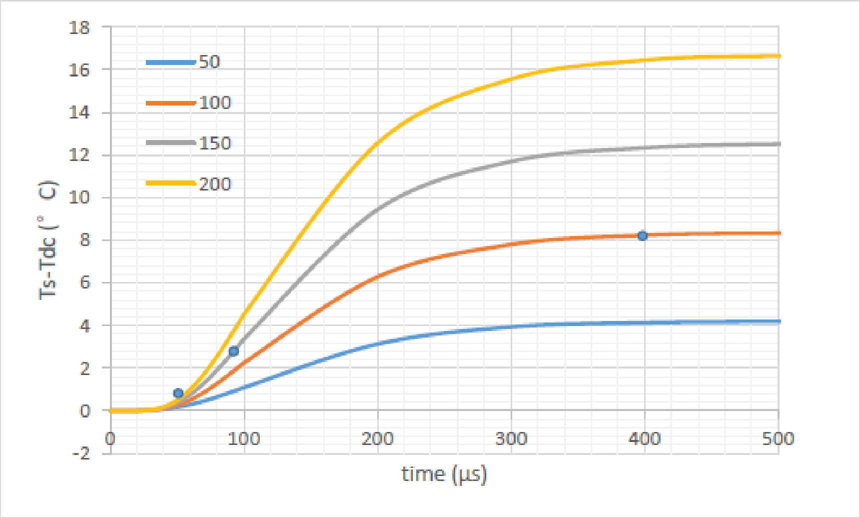

Figure 5.41 Surface temperature difference of specimens with constant heat fluxes from 50 to 200 MW/m$^2$.

On the other hand, if $T_b$ is high enough, the peak time at which a maximum temperature difference occurs is different from the cut-off time. Figure 5.42 shows the surface temperature differences of $T_{dc}$ and $T_s$ of a specimen when a constant heat flux of 10 MW/m$^2$ is applied with various cut-off times of 100 μs, 200 μs, 300 μs, 400 μs, 500 μs and 600 μs. Compared with the temperature difference curve for 600 μs of heating, the temperature difference curve for 100 μs of heating continues to increase after heating is stopped and achieves a peak value of 0.41 °C at 170 μs, which is 0.2 °C larger than that achieved at the cut-off time and 70 μs later. Similarly, other temperature differences have similar results – as the pulse width increases, the delay time gradually decreases. When the pulse width is 600 μs, the peak time is equal to the cut-off time (600 μs), which is termed the threshold time. The time to reach the maximum temperature difference will be equal to the threshold time when the cut-off time is larger than a threshold time.

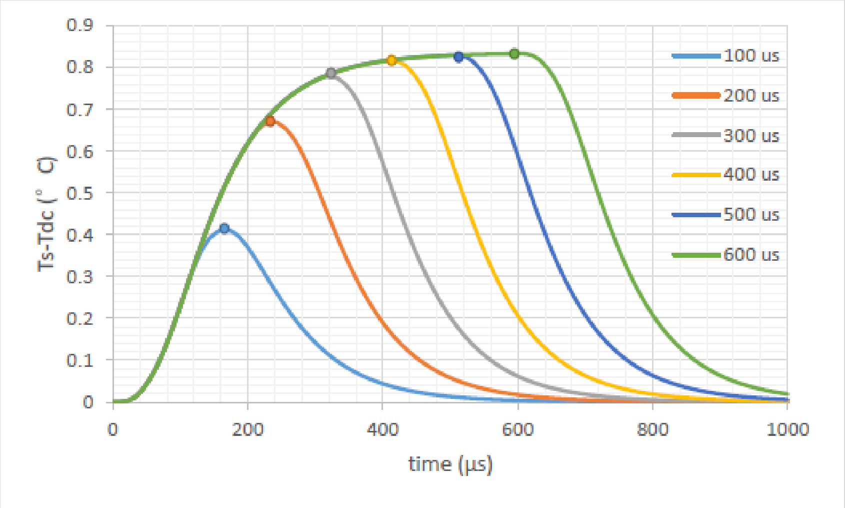

Figure 5.42 Surface temperature difference of $T_{dc}$ and $T_s$ of a specimen heated at a constant heat flux of 10 MW/m$^2$ for various times.

Figure 5.43 shows that the temperature differences at various heat fluxes have similar trends and are proportional to the heat flux. Meanwhile, delays in the peak time and threshold time are relatively enhanced.

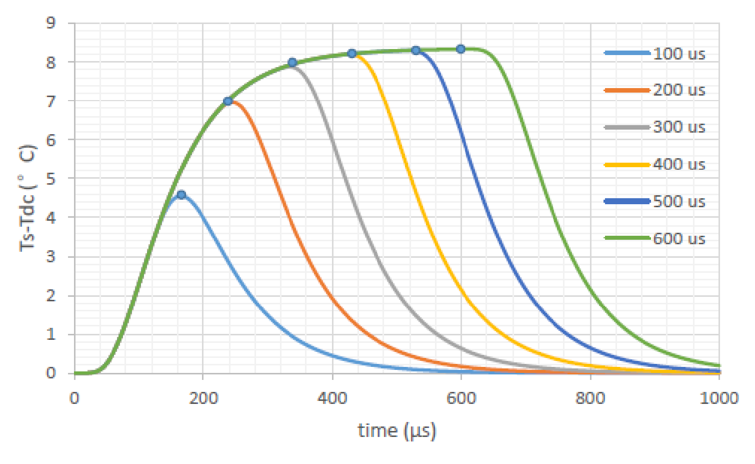

Figure 5.43 Surface temperature difference of $T_{dc}$ and $T_s$ of a specimen heated at a constant heat flux of 100 MW/m$^2$ for various times.

To analyse the effect of the heat flux density, the cut-off time was varied with different heating powers to ensure a constant total energy input. A parametric sweeping pulse was applied over a heating duration of 100 µs to 600 µs, and the total energy was fixed at 20 kJ/m$^2$. In Figure 5.44, the maximum bottom temperature exponentially decreases with increasing pulse duration, and all of the final bottom temperatures tend to stabilize at 343 K ($T_{ext}$=293 K and ΔT=50 °C). However, without input power, the average temperature will reach ambient temperature after a long enough cooling time due to convection cooling. The maximum bottom temperature curve can be used to calculate the minimum value of the pulse duration when the maximum temperature that a specimen substrate can support is given. The exponential function fitted by Matlab cftool is:

$$T_{b.max} = 167.8e^{-9414t} + 385.5e^{-106.6t} \tag{5. 10}$$

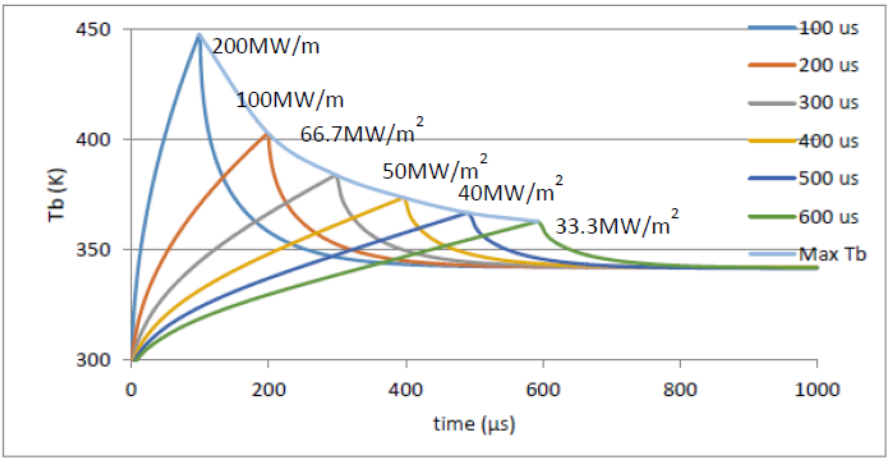

Figure 5.44 Bottom temperature for a constant heat flux versus pulse duration from 100 μs to 600 μs.

The corresponding temperature difference and duration can be determined from Figure 5.45. Rapid heating with a large heat flux can excite the specimen to achieve a large maximum temperature difference in a very short time, while the specimen heated by a relatively slower and smaller heat flux will show a lower temperature difference over a longer time for observation. In practical detection, it is difficult to observe the exact peak time at which the maximum temperature occurs. In addition, some errors may exist during detection, such as fluctuations in the environmental temperature. Therefore, it is useful to define a period of time, based around the peak time, over which to measure the temperature difference. In common temperature detection methods, the temperature approximately stabilizes after exceeding 1/e, i.e., 63% of its peak value. The temperature difference curve increased much faster, and thus, we chose 70% to estimate the achievable maximum temperature difference and peak time.

Table 5.6 shows the observation period and effective value when detection occurs at 70% of the maximum temperature difference. Compared with the constant temperature heating method, shown in Table 5.7, the pulse heating method can produce two or three times larger temperature differences (the maximum value is 9.10 °C) and observation times (the maximum value is 515 μs). Meanwhile, the maximum temperature difference obtained by pulse heating occurs later than that obtained by constant temperature heating. For detection, the surface temperatures obtained from the two methods are controlled under a heating temperature of $\Delta T+T_{ext}$, and thus, the detectability is the same because the surface temperature distribution is the same. However, to avoid specimen damage, the constant temperature method can guarantee that the temperature of every domain in the specimen is lower than the heating temperature. In contrast, the pulse heat flux method may produce an extremely high temperature on the bottom area, causing deformation and stress concentration depending on the material properties.

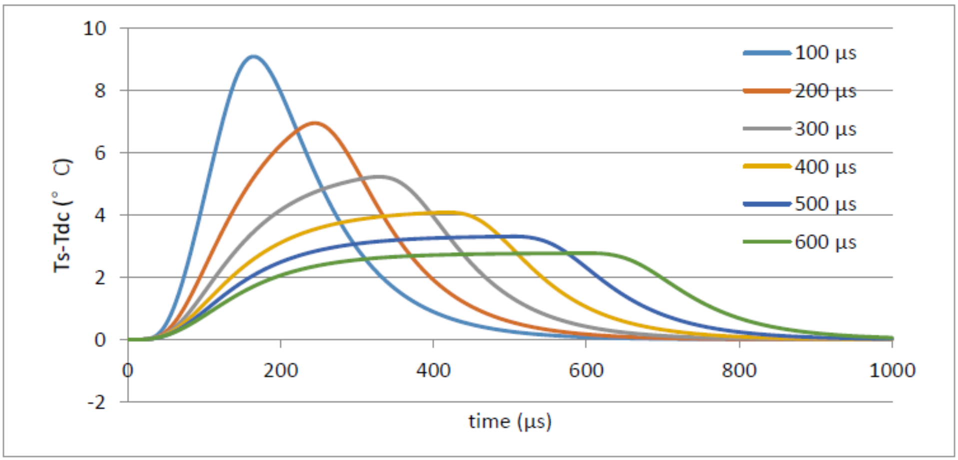

Figure 5.45 Surface temperature difference.

Table 5.6 Maximum temperature difference, peak time, duration and effective value at constant heat flux.

| Pulse Duration (μs) | Peak time (μs) | Max $T_s$-$T_{dc}$ (°C) | 70% Max $T_s$-$T_{dc}$ (°C) | Observation duration (μs) | Max $\Delta T_b$ (°C) |
|---|---|---|---|---|---|
| **100** | 164 | 9.10 | 6.37 | 100 | 154.38 |
| **200** | 245 | 7.00 | 4.87 | 158 | 109.75 |
| **300** | 328 | 5.23 | 3.66 | 235 | 90.8 |
| **400** | 420 | 4.09 | 2.86 | 324 | 80.52 |
| **500** | 508 | 3.32 | 2.32 | 415 | 73.61 |
| **600** | 603 | 2.78 | 1.94 | 515 | 69.68 |

Table 5.7 Maximum temperature difference, peak time, duration and effective value at constant heating temperature.

| Constant ΔT (°C) | Peak time (μs) | Max $T_s$-$T_{dc}$ (°C) | 70% Max $T_s$-$T_{dc}$ (°C) | Lasting time (μs) | Max $\Delta T_b$ (°C) |
|---|---|---|---|---|---|
| **50** | 170 | 3.74 | 2.62 | 230 | 50 |

### 5.4.3 Identification of the Defect Radius

Similar to section 5.2, the radius of the maximum thermal gradient demonstrates the radius of the defect, as shown in Figure 5.46. The radius (r=40 μm) of the largest temperature gradient on specimen surface presents the approximate location of the edge of the internal defect. Because the mesh of the defect area is set to 0.5 μm, the radius of the peak heat flux is the same as that determined by the constant temperature method.

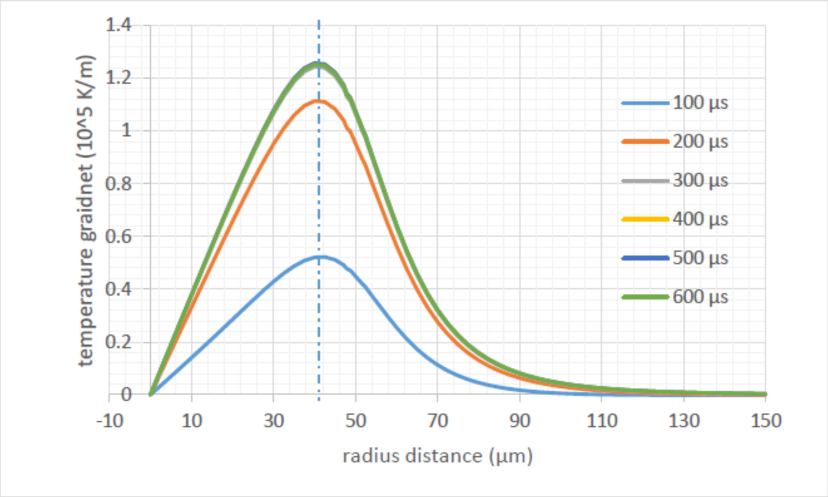

Figure 5.46 Temperature gradient with different pulse durations at the peak time.

## 5.5 Summary

An analytical expression was defined by using a 2D axisymmetric model as an infinite circular plane with an internal circular defect (50 μm radius) between a metal film and a semiconductor substrate in the centre of the plane. Two boundary conditions were evaluated to examine the thermal behaviour of heat transfer in a model with a defect. The results indicate the following:

- Dirichlet boundary conditions applied to specimens heated from the bottom surface produce a region of obviously lower temperature on the surface above the defect.
- In a nickel-copper-silicon model, the temperature difference between the defect and non-damaged areas achieves a peak value of 3.7 °C at 170 μs but rapidly approaches zero after 2000 μs. Thus, the response time of the thermal detector used in thermographic NDT must be less than 500 μs.
- The radius of the maximum temperature gradient on the surface can be used to locate the edge of the defect. The radius of the maximum temperature gradient is slightly smaller than the radius of the defect when the thickness of the film is less than the diameter of the defect. If the film thickness is larger than the defect diameter, the radius of the maximum temperature gradient is slightly larger than the defect radius.
- Neumann boundary conditions applied to specimens heated from the bottom also present an area of lower temperature on the surface above the defect. However, the temperature difference stabilizes after a period of time, and this threshold time is dependent on the intrinsic characteristics of the structure.
- The excitation method can control the response temperature and response time but not the location of the maximum temperature gradient, which is determined by the structure of the specimen.
- To protect the specimen from damage, a pulse heat flux is adopted to excite the specimen. The heat flux is inversely related to the pulse duration. Before the threshold time is reached, the surface temperature difference decreases, and the temperature difference duration increases as the pulse duration increases. Meanwhile, the maximum bottom temperature also increases.
- The detectability is related to the dimensions of the specimen and the defect. The maximum temperature difference increases almost linearly with the thermal

diffusivity of the substrate material but decreases in a more complex manner with the thermal diffusivity of the film material.

- The maximum temperature difference is obtained earlier when the substrate material has a higher thermal diffusivity.
- Lower thermal diffusivity materials, such as PTFE, NiCr and Ni, can provide better detectability than higher diffusivity materials, such as Ag, Cu and Al.
- The maximum temperature difference decreases with the thickness of both the film and the substrate, while the time to achieve the maximum difference increases. Due to the low thicknesses of films in MEMS devices, which are typically on the order of a few micrometres, the substrate thickness has larger effect on the detectability.
- The required temperature resolution and time resolution vary with the material and thickness of the film and substrate. High thermal diffusivity materials require high-speed cameras and a high temperature resolution. The thermal diffusivity influences the time resolution more than the film thickness. High-diffusivity substrate materials require a high time resolution, while thick substrates require a high temperature resolution. The time resolution is approximately 1/10 of the time duration.

# Chapter 6 Experimental Evaluation of Defect Detection using Infrared Thermography

## 6.1 Introduction

Chapters 4 and 5 investigated the relationship between the achievable temperature difference and various parameters such as structural parameters (layer thickness and defect radius), physical parameters (thermal diffusivity) and excitation parameters (heat flux and heating duration). The temperature difference was found to increase with an increase in the defect radius (detectability increases) but decrease when using a thicker film or substrate (detectability worsens). However, it is difficult to validate this trend at the micro- and nanoscale because the resolution of current IR cameras, including the spatial resolution and imaging speed (frames per second), is not high enough to observe small defects. Therefore, investigations based on specimens possessing artificial defects at the millimetre scale are designed and implemented using the IR thermography NDT method to verify the above conclusion. Specimens composed of layers of various materials are examined. In addition, the lock-in thermographic detection method is applied to reduce noise.

## 6.2 Specimen Preparation

The specimens used in this experiment contained three materials with very different thermal conductivities, i.e., copper, which has a high thermal conductivity (401 W/m·K); stainless steel, which has a moderate thermal conductivity (15 W/m·K); and an acrylic material with a low thermal conductivity (0.6 W/m·K) [170, 172]. In this respect, these materials present the extreme thermal conductivities of materials used in MEMS devices. Meanwhile, the acrylic material also functions as an adhesive to connect the other materials. Relevant thermal properties, i.e., the melting point, density (ρ), thermal capacity ($c_p$), thermal conductivity (k) and thermal diffusivity (α), of these three materials are given in Table 6.1.

Table 6.1 Thermal properties of the experimental materials at 300 K.

| **Materials** | **Melting point (K)** | **ρ (kg/m$^3$)** | **$c_p$ (J/kg·K)** | **k (W/m·K)** | **α×10$^6$ (m$^2$/s)** |
|---|---|---|---|---|---|
| **Copper [170]** | 1358 | 8933 | 385 | 401 | 117 |
| **Stainless steel [170]** | 1670 | 8055 | 480 | 15.1 | 3.91 |
| **Copper leaf frame [171]** | 1083 | 8780 | 386 | 260 | 76.7 |
| **Acrylic [172]** | 400-410 | 1190 | 1470 | 0.6 | 0.34 |

The specimen includes three different layers: the covering layer, the middle layer and the substrate. To ensure a reliable bond between these layers, thin adhesive layers (typically acrylic glue) are applied on the surface of the covering layer and the substrate. This adhesive layer is only 5 μm thick and can thus be neglected in calculations. Meanwhile, open windows with widths and lengths ranging from 1 mm to 4 mm were created in the middle layer to simulate possible defects. A sketch of the middle layer is shown in Figure 6.1 (a), and the structure of the triple-layered specimen is shown in Figure 6.1 (b).

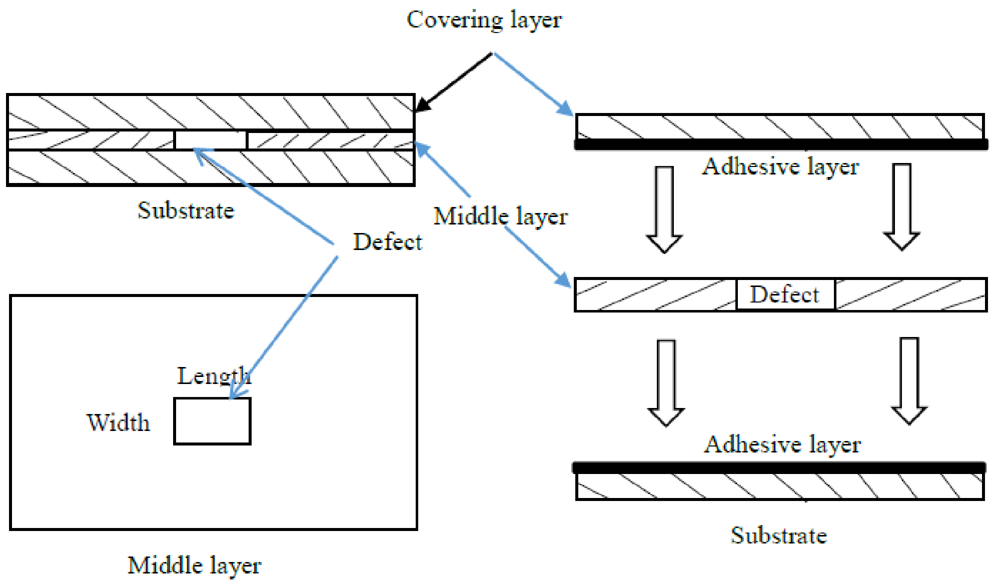

Figure 6.1 Sketches of (a) the specimen structure with a defect and (b) the assembly schematic.

To avoid surface unevenness, which can result in variations in the surface emissivity and further affect the detected temperature, the covering and substrate layers should be as smooth as possible, especially the surface over the defect area. Thus, after these three layers are assembled using the pre-coated acrylic glue, the entire structure is placed between two smooth glass plates and pressed under a ballast (the average pressure is calculated to be approximately 1 MPa) for 24 hours. The specifications of the prepared specimens are listed in Table 6.2. In the different middle layers, a rounded window 4 mm in diameter is created in the copper film, a rectangular window with a size of 4 mm × 2.3 mm is prepared in the stainless-steel plate, and a special pattern containing holes of uneven sizes is created in the 0.2 mm-thick copper plates (lead frame). As shown in Figure 6.2, the dimensions of the smallest holes in the copper plate are 2 mm × 1 mm, while the largest holes have dimensions of 4.5 mm × 1.5 mm. The overall length and width of the specimens are approximately 50-80 mm, which are much larger than that of the defect. The specimen can thus be regarded as an infinite plane compared to the defect.

Table 6.2 Specifications of the specimens.

| | Materials | Thickness (mm) | Length×Width of Defect (mm × mm) |
|---|---|---|---|
| **S1** | Steel-Cu film-Acrylic | 0.15-0.05-0.31 | 4 × 4 |
| **S2** | Cu film-Steel-Acrylic | 0.05-0.15-0.31 | 4 × 2.3 |
| **S3** | Cu film-Cu plate-Cu film | 0.05-0.20-0.05 | 1.2 × 0.7 |
| **S4** | Cu film-Cu plate- | 0.05-0.20-0.31 | 1.2 × 0.7 |
| | Acrylic/Cu film | 0.05-0.20-0.05 | 1.2 × 0.7 |
| **S5** | Cu film-Cu plate-Acrylic | 0.05-0.20-0.31 | 1.2 × 0.7 |

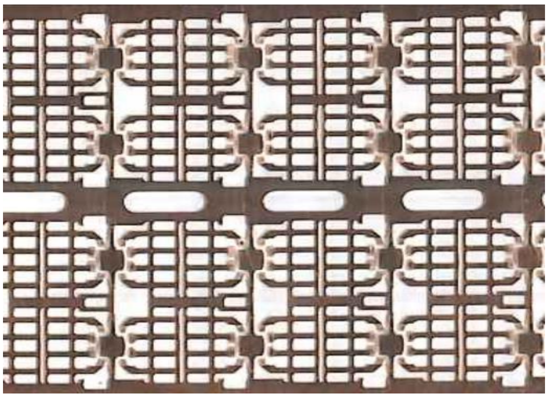

Figure 6.2 Photograph of the hollow copper plate used in the middle layer.

## 6.3 Experimental System

Figure 6.3 shows a sketch of the lock-in thermographic NDT experimental setup. The instruments used in the experiment are shown in Figure 6.4. The experimental lock-in thermographic imaging detection system, discussed in Chapter 2, was composed of an 808 nm semiconductor laser with a power supply as the exciter, a cooled IR imager (FLIR model SC7000) and an NI (National Instruments) data acquisition card as the detector. In the experiment, the specimen was fixed by a small fixture on the track. An 808 nm semiconductor laser and power supply were used to excite the specimen from the bottom surface in transmission mode. The modulation frequency of the laser was chosen to be either 0.1 Hz or 0.2 Hz, and the peak power of the laser was set to 18 W. The spot size of the laser on the specimens was 1000 mm$^2$. The heat flux was applied in a sinusoidal function:

$$\mathrm{q(t)} = q_0(1 - \cos(2\pi f_e t)) \tag{6. 1}$$

where q(t) is the periodically varying heat flux, $q_0$ is the heat flux at the heating location of the sample and $f_e$ is the frequency modulation of the heating exciter.

The temperature field on the top surface was measured with a cooled IR imager (FLIR model SC7000 [166]) that was placed parallel to the surface of specimen. This system can achieve a pixel pitch of 15 μm using a 22 mm microlens. The FLIR SC7000 thermal camera could achieve dimensions of 640 × 512 pixels with high accuracy (±2 °C, ±2%), and an indium antimonide (InSb) detector was used to achieve a NETD as low as 20 mK. The camera offers integrating times ranging from 10 μs to 1 ms, while the frame rate is 25 F/s due to memory limitations of the controlling computer used to synchronize the laser and camera and to calculate the amplitude and phase of the collected signals.

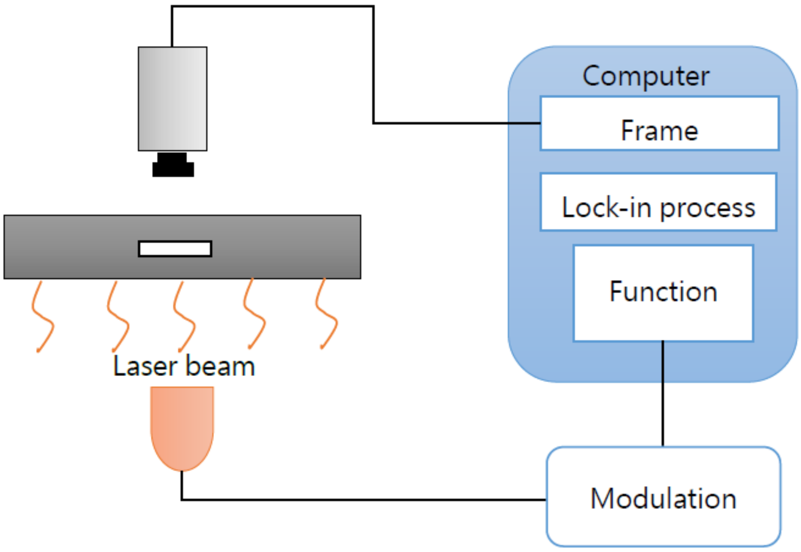

Figure 6.3 Sketch of the lock-in thermographic NDT system.

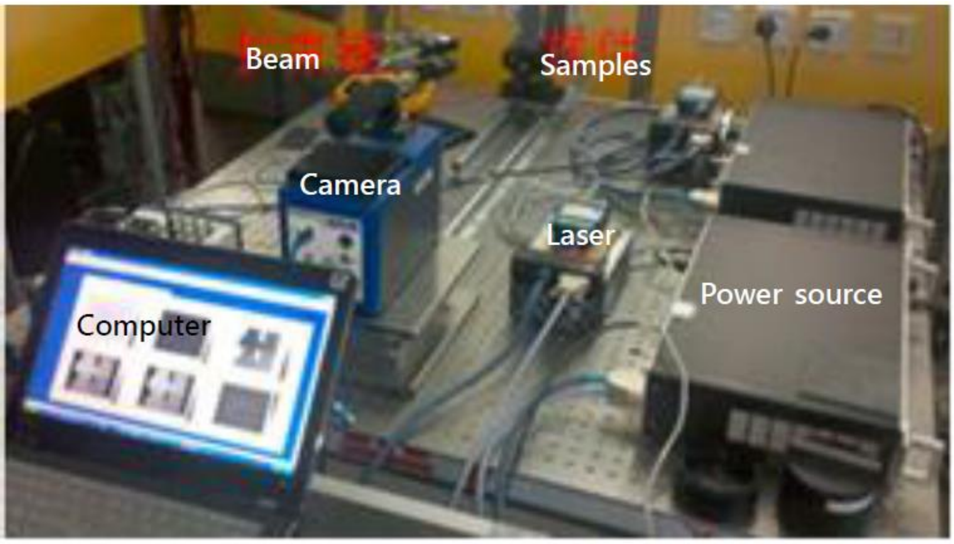

Figure 6.4 Photograph of the lock-in thermographic NDT system in transmission mode.

In the experiment, although the shortest exposure time the thermal camera can attain is 10 μs, the frame rate is only 170 F/s (5.9 ms for a frame). Thus, it is difficult to examine the heating temperature, as the heating time is too short to be captured exactly in a single frame (230 μs). This problem can be solved by improving the imaging speed of the thermal camera or repeating the pulse heating. However, current thermal cameras are not capable of providing such high-speed imaging. Additionally, repeated pulse heating may induce a large amount of noise during high-speed cooling. Hence, another technique, namely, the lock-in method, is proposed to solve this issue.

In lock-in thermography, the surface of the specimen is heated by a modulated periodic energy pulse. The temperature modulation signal induced from the heating pulse propagates as a "thermal wave" in the specimen. As this wave (which describes the space-time dependence of the temperature modulation) undergoes refractions, the resulting signal across the component is modified. The phase angle and amplitude difference between the input energy and the resulting surface temperature oscillation are sensitive indicators for such modifications. By comparing the thermal response of the defect regions with respect to the sound regions of the material, the position and thickness of the defects inside the specimen can be analysed. For this purpose, the surface temperature is monitored with a thermographic camera during modulated heating, and Fourier transformation is used to extract the magnitude and phase data by transforming the surface temperature data to a polynomial with respect to time. In the obtained results, the contribution from any signal that is not at the same frequency as the heating pulse is attenuated close to zero. In addition, the out-of-phase component of the signal that has the same frequency as the reference signal is also attenuated (because sine functions are orthogonal to cosine functions of the same frequency), making lock-in thermography a phase-sensitive detection method. Depending on the dynamic reserve of the instrument, signals up to 1 million times smaller than the noise components and potentially fairly close in frequency can be reliably detected. Therefore, thermography NDT using the lock-in technique can be used to examine detects inside of a specimen, as it can distinguish minor temperature differences on the specimens from the noise induced by fluctuations of the input energy or tested structure. A typical temperature curve obtained from lock-in NDT is demonstrated in Figure 6.5. The temperature increases continuously until stabilizing at a level determined by the heating criterion and thermal dissipation conditions. Once the temperature is stabilized, the amplitude and phase angle can be measured. To ensure the accuracy of the results, data at four different times were collected (Figure 6.6) in 1/4 increments of the total time. In addition, the temperature amplitude (A) and phase angle (Φ) of the tested component were then calculated using the following equation [175]:

$$A = \sqrt{(T_1 - T_3)^2 + (T_2 - T_4)^2} \tag{6. 2}$$

The phase was calculated by Equation (6.3).

$$\emptyset = \tan^{-1}\left(\frac{T_1 - T_3}{T_2 - T_4}\right) \tag{6. 3}$$

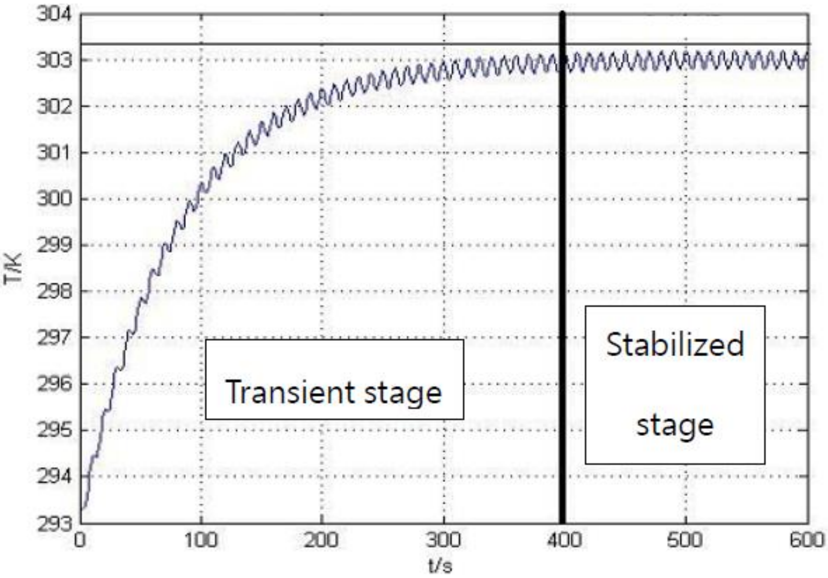

Figure 6. 5 Spot temperature measurement of the system from the transient stage to the stabilized stage [174].

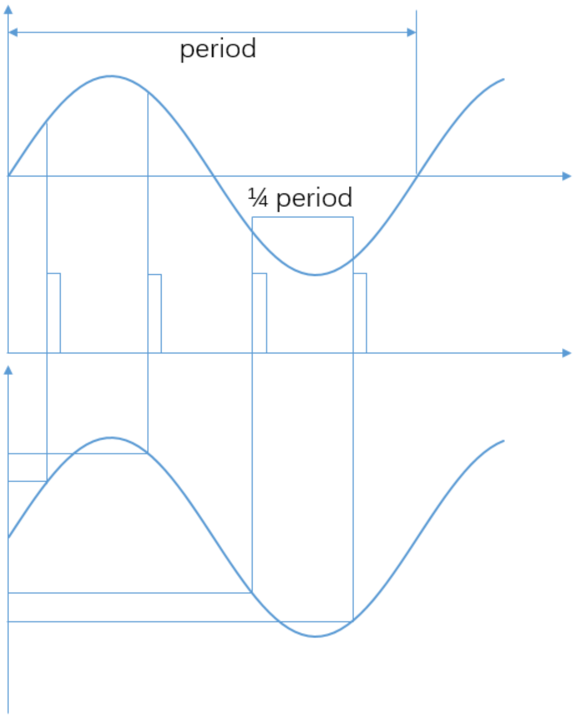

Figure 6.6 Sketch of the principle behind lock-in thermographic NDT.

To evaluate the feasibility of active thermography NDT in transmission mode, experimental tests based on the lock-in technique in transmission mode were performed on the prepared specimens, as many devices are built on substrates thin enough (for instance, a 200 μm silicon wafer) to undergo heating excitation. The simulation model for lock-in thermography is similar to the transient model established previously. The dimension of each material was enlarged, as listed in Table 6.2, and the relevant material properties were based on those of the bulk materials, as presented in Table 6.1. Additionally, in contrast to the transient model, the heating boundary conditions were set to be a periodically changing heat flux, as in Equation (6.1), with $q_0$=16 KW/$m^2$ and $f_e$=0.1 Hz/0.2 Hz.

## 6.4 Experimental Results and Analysis

Experimental studies were performed to examine the applicability of this method for the detection of artificial delamination defects in multilayer specimens. The amplitude and phase image results for five specimens (S1-5) achieved by lock-in thermography

NDT were analysed using the Matlab software version R2012a [176]. Meanwhile, the defect pattern and temperature pattern on the surface are compared.

### 6.4.1 Specimen with Substrates with Different Thermal Diffusivities

I. Stainless-steel substrate and copper middle layer

Figure 6.7 and Figure 6.8 show the amplitude and phase images of specimen S1 heated from the stainless-steel substrate. The images were obtained 5 min after heating and when the temperature of the specimen reached a steady state. In Figure 6.7, the lower temperature area, highlighted by a dark blue circle, indicates the location of the internal artificial defect. The image was found by the Matlab software to contain 416 × 617 pixels. The calibration of the actual dimension to pixels is 0.10 mm/pixel, and that of temperature to the RGB value is 60 °C/255, according to the legend in Figure 6.7 (a). To analyse the temperature difference between the defect and defect-free areas, a line profile crossing the centre (x=26.3 mm, y=26.3 mm) of the lowest temperature point along the y direction was determined.

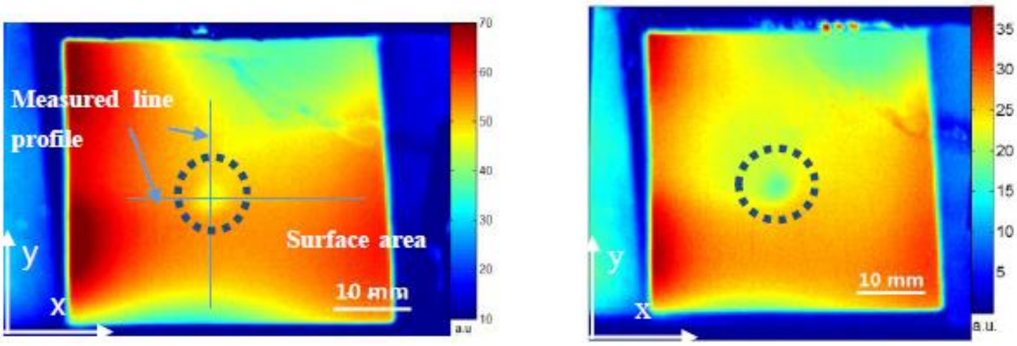

(a) f=0.1 Hz (b) f=0.2 Hz

Figure 6.7 Amplitude images of specimen S1 at different excitation frequencies of (a) 0.1 Hz and (b) 0.2 Hz.

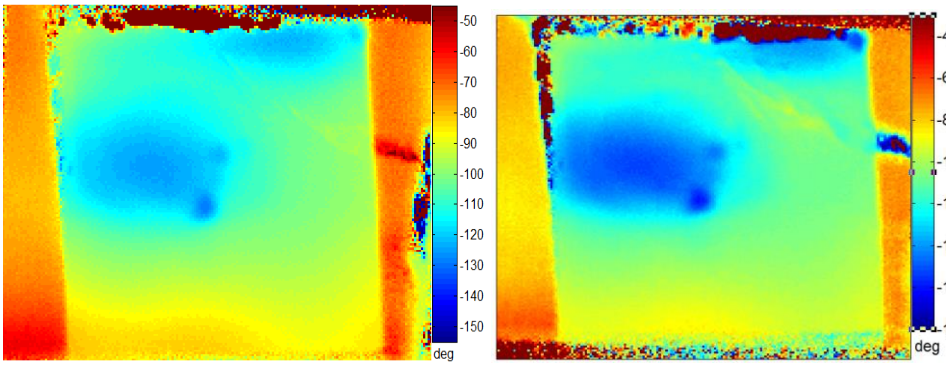

(a) f=0.1 Hz (b) f=0.2 Hz

Figure 6.8 Phase images of specimen S1 at different excitation frequencies of (a) 0.1 Hz and (b) 0.2 Hz.

The original temperature amplitude images were denoised using the Adobe Photoshop Express software. A filtered amplitude image of specimen S1 at 0.1 Hz excitation is shown in Figure 6.9. The amplitude temperature lines in following analysis were extracted from the filtered images. As shown in Figure 6.10, the blue dots depict the change in the surface temperature amplitude (noise removed) through the lowest temperature centre in the y direction. The smallest amplitude is 45.28 °C, while the sound area shows a temperature amplitude of approximately 55 °C. To determine the position of the largest temperature amplitude gradient, the Curve Fitting Tool in the Matlab software was used to approximate the temperature amplitude points into a smooth curve by using a sum of the sine expression (curve cfA in Figure 6.10). A lower temperature amplitude is clearly revealed in the amplitude profile. Then, the temperature amplitude gradient (curve TA grad in Figure 6.10) was obtained by taking the derivative of the curve cfA with respect to the y distance. The two largest absolute values of the temperature amplitude gradient at the sides of the defect centre (26.30 mm), determined by the lowest temperature amplitude, determine the edges of the defect to be located at 25.10 mm and 27.50 mm. Thus, the measured diameter of the defect in the y direction is 2.40 mm, which is smaller than the real size. Figure 6.11 shows the temperature amplitude profile and temperature amplitude gradient in the x direction. The locations of the two largest absolute values of the temperature gradient are 25.08 mm and 28.42 mm. The measured diameter of the defect is 3.34. Because the pixel resolution in this image is 0.10 mm, the experimental measurement may have errors on the order of a fraction of a millimetre.

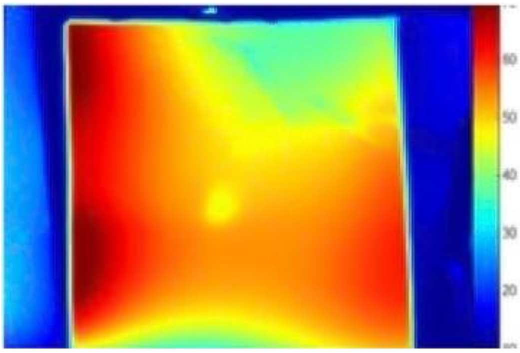

Figure 6.9 Filtered amplitude image (from Figure 6.7 (a)).

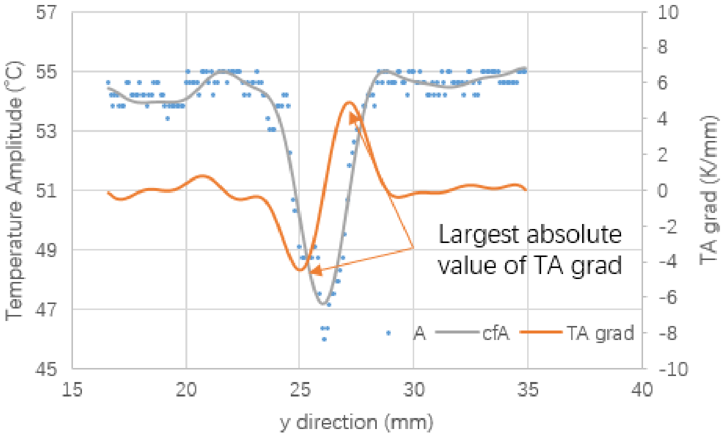

Figure 6.10 Surface temperature amplitude line profile through the centre of the defect in the y direction and the temperature amplitude gradient for f=0.1 Hz.

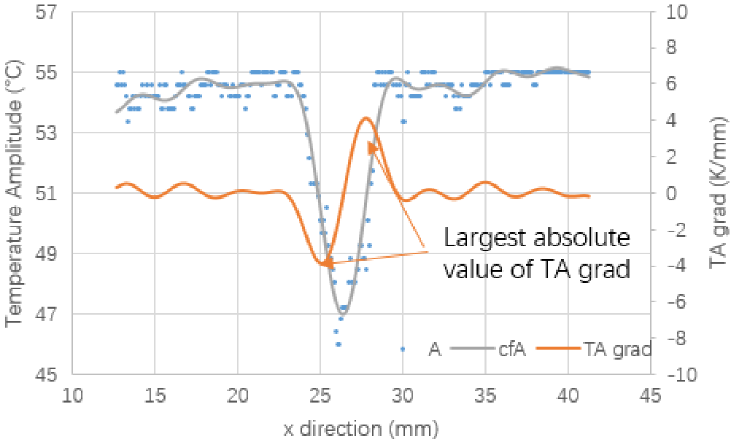

Figure 6.11 Surface temperature amplitude line profile through the centre of the defect in the x direction and the temperature amplitude gradient for f=0.1 Hz.

The predicted temperature amplitude distribution of specimen S1 at 0.1 Hz excitation (the partial enlargement at the defect area is shown in Figure 6.12) reveals a low-temperature area on the surface, which agrees with the experimental image (Figure 6.7 (b)). The lowest predicted temperature amplitude of the defect centre is 32.8 °C, and the sound area temperature amplitude is 37.1 °C, which are slightly smaller than the experimental results, possibly because the internal algorithm in the camera software used in the lock-in technique is complex and proprietary. The phase diagrams in Figure 6.8 (a) and (b) can also reveal the location of the defect, as discussed in section 6.3. The phase difference is approximately 50.0°, which is similar to the predicted simulation result of 51.6°. Furthermore, the measured diameter of the defect is 2.8 mm, which agrees with the experimental result.

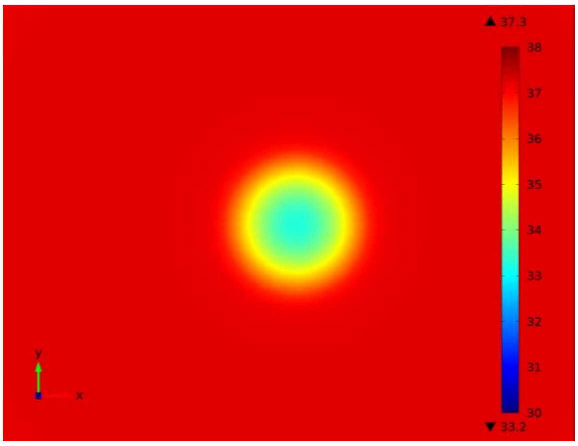

Figure 6.12 Partial magnification of the simulated amplitude image on the surface of specimen S1 at 0.1 Hz excitation.

Figure 6.13 and Figure 6.14 show the temperature profiles and temperature gradients using laser excitation with a 0.2 Hz modulation frequency. The smallest temperature amplitude of the defect centre is 17.89 °C. The temperature amplitude differences in the y direction are 8.05 °C and 9.94 °C. The two maximum absolute temperature amplitude gradients are located at 25.28 mm and 27.81 mm. Therefore, the measured diameter of the defect is 2.53 mm. In the x direction, the measured diameter of the defect is 27.9–24.5 mm=3.4 mm. The simulated temperature amplitude difference in the steady state is 1.0 °C, where the stabilization duration is 300 s and the measured diameter is the same as that found in the simulation result using a 0.1 Hz modulation frequency.

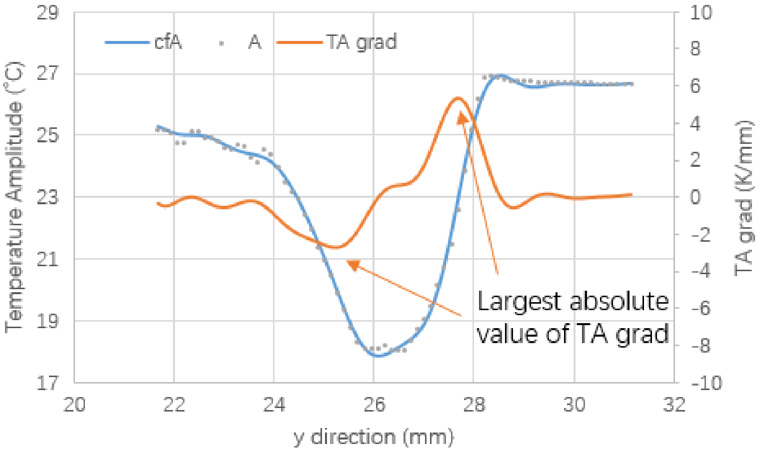

Figure 6.13 Surface temperature amplitude line profile through the centre of the defect in the y direction and the temperature amplitude gradient for f=0.2 Hz.

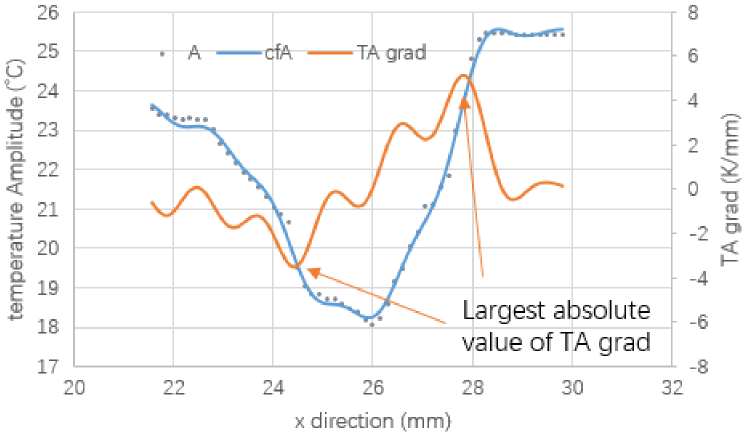

Figure 6.14 Surface temperature amplitude line profile through the centre of the defect in the x direction and the temperature amplitude gradient for f=0.2 Hz.

II. Copper substrate and stainless-steel middle layer

Figure 6.15 and Figure 6.16 show the amplitude and phase images of specimen S2 (acrylic/copper/steel) excited by a 0.1 Hz and 0.2 Hz laser pulse. A dark area can be observed in the upper left corner of the diagram, over the defect. Specimen S2 contains a rectangular defect (4 mm × 2.3 mm) on a stainless-steel plate. The corner of the specimen is shown in the bottom right corner of the image. Similar to specimen S1, the experimental images were denoised by the Photoshop software. The distance-to-pixel calibration is 0.047 mm per pixel, and the temperature-to-RGB calibration is 0.118 °C/255. The 0.1 Hz image is fuzzier than the 0.2 Hz image, and thus, it is more difficult to locate the edge of the defect. The lowest temperature amplitudes of the defect area are 2.2 °C and 1.5 °C, while the greatest temperature amplitude differences are 2.2 °C and 2 °C. The defect area in the phase image is slightly clearer than that in the amplitude image; however, the image of the defect can be influenced by edge effects.

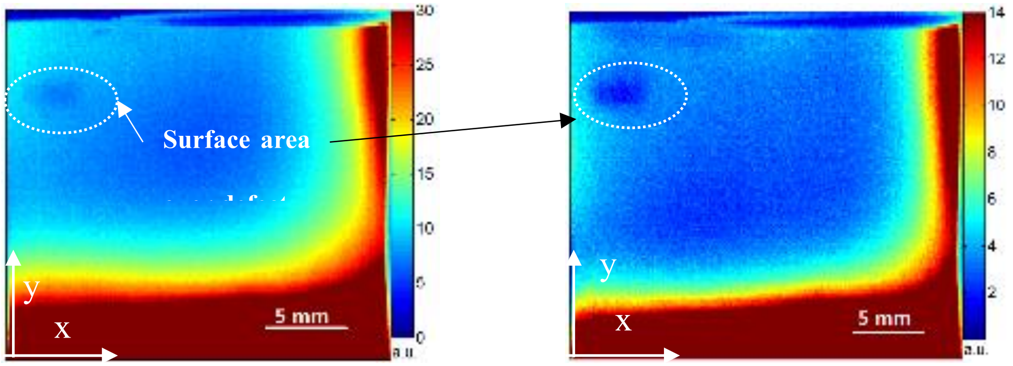

(a) f=0.1 Hz (b) f=0.2 Hz

Figure 6.15 Amplitude of specimen S2 at different excitation frequencies of (a) 0.1 Hz and (b) 0.2 Hz.

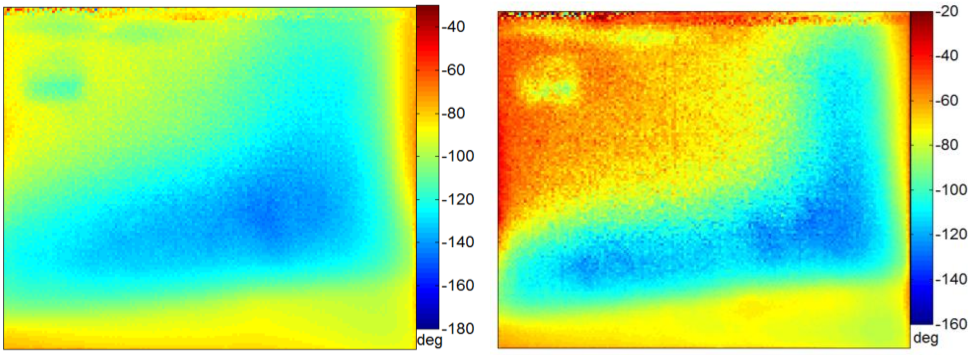

(a) f=0.1 Hz (b) f=0.2 Hz

Figure 6.16 Phase images of specimen S1 at different excitation frequencies of (a) 0.1 Hz and (b) 0.2 Hz.

The difference in the simulation amplitude and detectability of specimen S2 is smaller than that of specimen S1, which agree with the experimentally observed amplitude differences. Meanwhile, specimen S1 contains the same top film as specimen S2, but shows a worse temperature image. This phenomenon can be analysed in future work. In conclusion, the above experiments on specimens S1 and S2 improve the analyses presented in Chapter 4 and Chapter 5 on the thickness and thermal diffusivity of the substrate material.

In summary, this section has shown that the maximum absolute value of the temperature gradient near the centre of the low-temperature area aids in the measurement of the defect size, and the measured size will be smaller than the actual size. In addition, a substrate material with low thermal diffusivity will show a smaller temperature difference.

### 6.4.2 Specimen with High Thermal Diffusivity Covering Layer

According to the simulation results, the higher the thermal conductivity of the covering film material, the more difficult it is to detect the defect area. Figure 6.17 and Figure 6.18 show the amplitude and phase images of specimen S3, which contains a covering film composed of copper. The high thermal conductivity of copper allows the heat energy to quickly diffuse in the lateral direction. The surface area over the defect is quickly heated by the surrounding area, which was heated directly from the defect-less middle layer. Using the existing technical equipment, even the phase image could not provide a clear image of the defect.

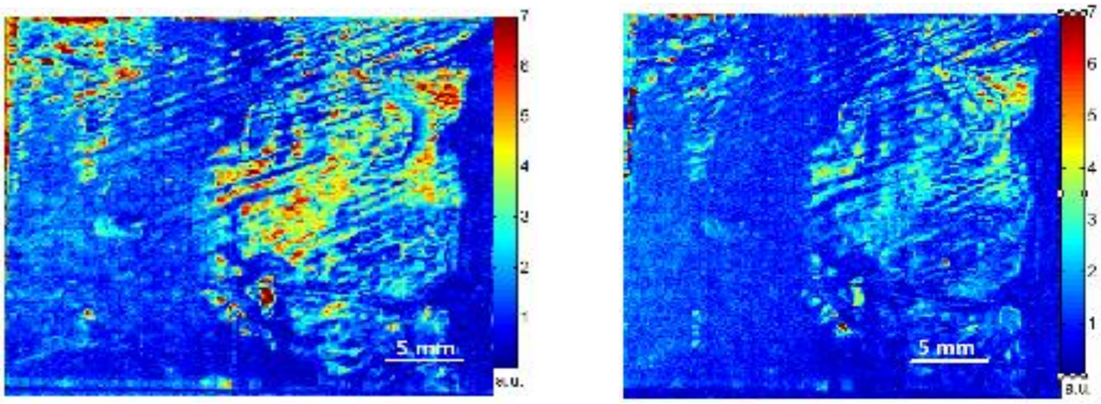

(a) f=0.1 Hz (b) f=0.2 Hz

Figure 6.17 Amplitude images of specimen S3 at different excitation frequencies of (a) 0.1 Hz and (b) 0.2 Hz.

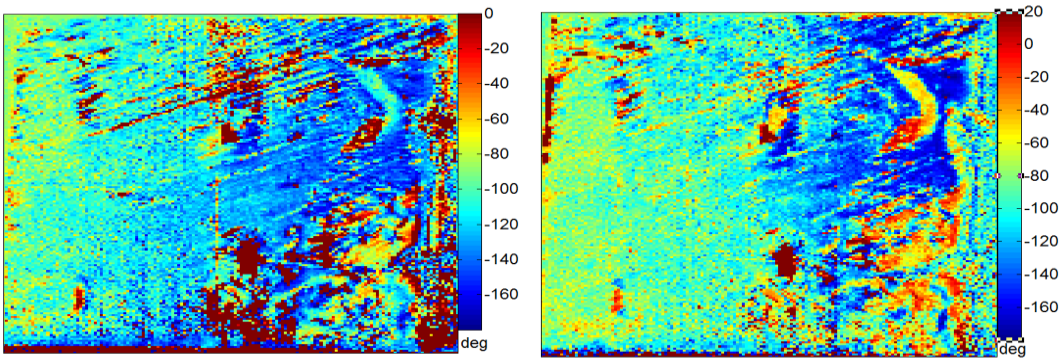

(a) f=0.1 Hz

(b) f=0.2 Hz

Figure 6.18 Phase images of specimen S3 at different excitation frequencies of (a) 0.1 Hz and (b) 0.2 Hz.

The copper and acrylic covering layers were compared using specimen S4, which is covered with copper on the left side and acrylic on the right side, as shown in Figure 6.19. The amplitude and phase images of specimen S4 excited by a 1 Hz laser pulse are shown in Figure 6.20. The temperature on the acrylic surface shows a clearer image, revealing the defect pattern related to the hollow copper plate (Figure 6.2), than that on the copper film surface.

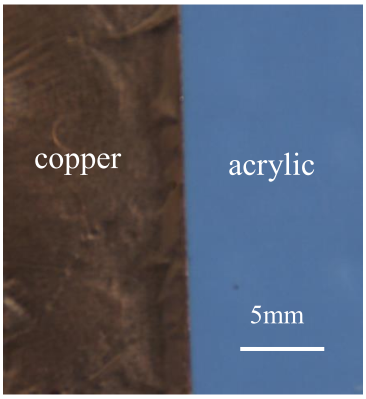

Figure 6.19 Optical photograph of specimen S4.

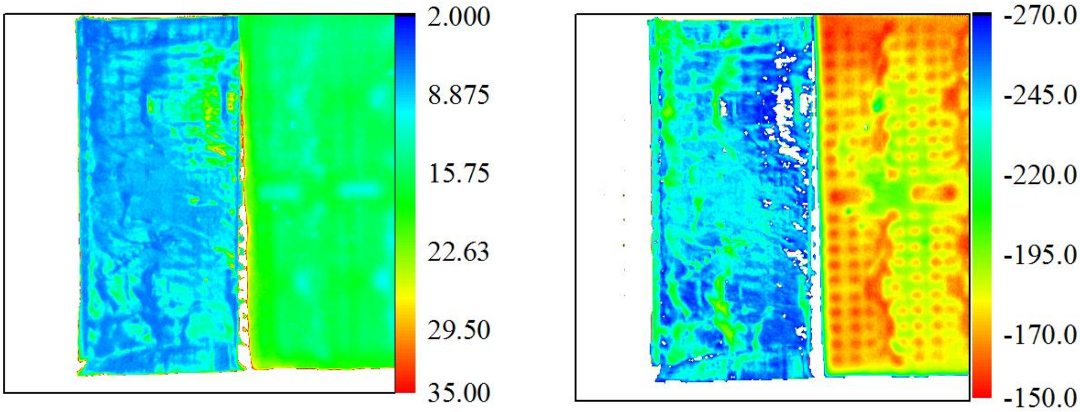

(a) Temperature amplitude image (b) Phase image

Figure 6.20 Thermographic images of the amplitude and phase of specimen S4.

### 6.4.3 Comparison of the Surface Temperature of the Pattern and the Middle Layer

Figure 6.21 and Figure 6.22 show the amplitude and phase images of specimen S5, in which the covering film is composed of acrylic. Due the intricate pattern of the defect, the surface temperature over a hole is not only heated by energy transfer from the nearest wires but also cooled by the next hole. Although the sizes of the open spaces are similar to that of the defect in specimens S1 and S2, the image of the surface temperature is more uniform. The low-temperature area over the artificial defects is blurry. To compare the real defect size with the experimental result, Figure 6.2 and Figure 6.21 (b) were overlapped, and Figure 6.23 shows that the lower temperature area is smaller than the actual size of the gap between the wide leads. While for the gap between narrow leads, the low-temperature area is larger than the actual size. By comparison, the temperature image demonstrates the exact location and relative size of the defect. The low-temperature area is slightly smaller than the actual defect.

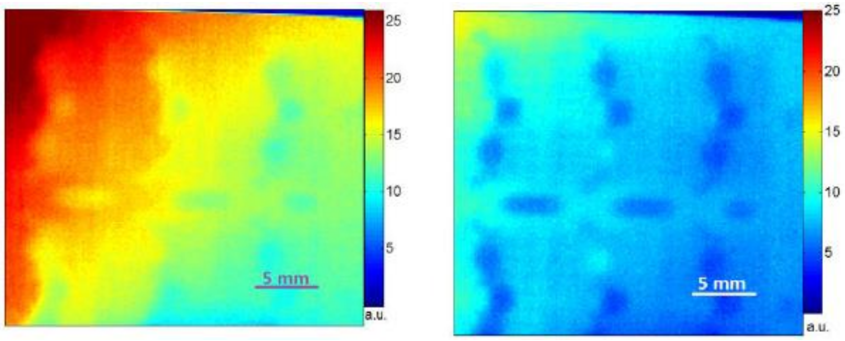

(a) f=0.1 Hz (b) f=0.2 Hz

Figure 6.21 Amplitude images of specimen S4 at different excitation frequencies of (a) 0.1 Hz and (b) 0.2 Hz.

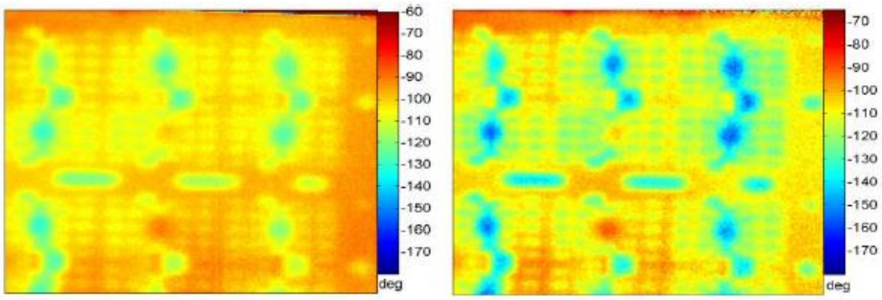

(a) f=0.1 Hz (b) f=0.2 Hz

Figure 6.22 Phase images of specimen S4 at different excitation frequencies of (a) 0.1 Hz and (b) 0.2 Hz.

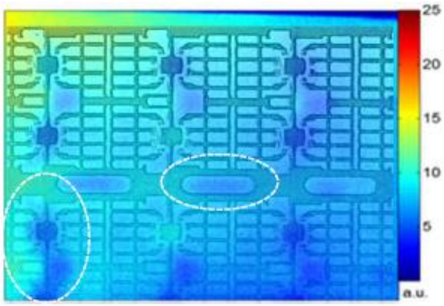

Figure 6.23 Overlapping image of the transmission image of the copper plate and the temperature amplitude image.

## 6.5 Conclusion

In this chapter, experimental tests and numerical predictions were carried out using the lock-in method. The experimental results agree well with the predicted data, thus confirming the accuracy of the established model. The lock-in thermography results show that transmission thermographic NDT is able to detect an internal defect on the millimetre scale. The maximum absolute value of the temperature gradient can be used to locate the edge of the defect. The temperature difference is also influenced by the sample materials. A high-diffusivity substrate material affords high detectability, while a low-diffusivity substrate reduces the detectability. In contrast, a low-diffusivity covering film affords better detectability. Specimens containing very high-diffusivity materials, such as copper, are difficult to detect.

# Chapter 7 Conclusions, Recommendations and Future Works

## 7.1 Main Conclusion

In this research, a unique model of heat transfer and the dynamic temperature distribution under various thermal excitation conditions (constant temperature, constant heat flux, pulse heat flux, periodic pulse heat flux) was developed to examine internal defects between the thin layer and substrate in a structure. Computational FEM simulations were used to analyse in detail several important aspects of thermal effects on a structure with an internal defect. Some of simulation results (lock-in technique in transmission mode) were verified by corresponding experiments, including the heat transfer characteristics near the defect, temperature variations on the surface and inside the structure, and influencing factors and trends in the temperature difference on the defect and defect-free surfaces.

Similar thin film and substrate structures have been studied [107]. However, these studies have neglected the substrate thickness and assumed the substrate to be a semi-infinite solid, which equivalently acted as a thermal sink. These assumptions limited the models used with the thermographic reflection method. In this research, the substrate thickness is comparable to the thickness of the thin top layer, which must be taken into account in the tests. Transmission thermography analysis is appropriate for small-sized objects, in which the exciter and detector cannot be placed on the same side.

The conclusions from this research are summarized in this section and categorized into three main areas: 1) typical thermal behaviours of thin film and substrate structures in the transient transmission thermographic NDT method; 2) effects of the thermal excitation method on the corresponding temperature difference and duration; 3) and the influence of structural parameters, such as the thicknesses of the top layer and substrate, the radius of the defect, and the characteristics of the thermal material, on the temperature distribution and detectability.

### 7.1.1 Thermal Behaviour of Thin Film/Substrate Structures

I. Constant temperature heating

When the bottom surface of the substrate is subjected to a constant temperature, the temperatures of both the defect ($T_{dc}$) and defect-free ($T_s$) area increase, and the temperature difference ($T_s$–$T_{dc}$) increases until it achieves a peak value (max $T_{diff}$) at a particular time ($t_{peak}$). When $T_{dc}$ and $T_s$ reach a constant value slightly lower than the given temperature, $T_s$–$T_{dc}$ trends towards zero. The time at which the constant peak value occurs is an essential parameter.

The analysis showed that the vertical heat flux applied at the bottom is forced to change its orientation at the edge of the defect before arriving at the interface, because the defect blocks most of the heat transfer. The heat flux accumulated near the edge of the defect is the primary reason for the temperature difference on the surface, as shown in Figure 7.1. After the heat flux circumvents the defect, the heat energy in the thin film over the defect transfers in the horizontal direction to the centre of the defect. Temperature of the thin film over the defect increases, and therefore, the temperature difference ($T_s$–$T_{dc}$) decreases. Thus, the defect can be located by calculating the surface temperature gradient (equivalent to the heat flux), as the location of the maximum value corresponds to the edge of the defect. According to the modelling results, the location at which the maximum temperature gradient occurs is not time dependent. Moreover, the location is slightly smaller than the radius of the defect when the thickness of the film is smaller than the diameter of the defect, while the location is slightly larger than the defect when the diameter is equal to or larger than the film thickness. The distance between the maximum gradient and the defect edge depends on the thickness of the film and the ratio between the film thickness and the defect diameter. However, the distance is independent of the time it takes to reach the maximum temperature difference.

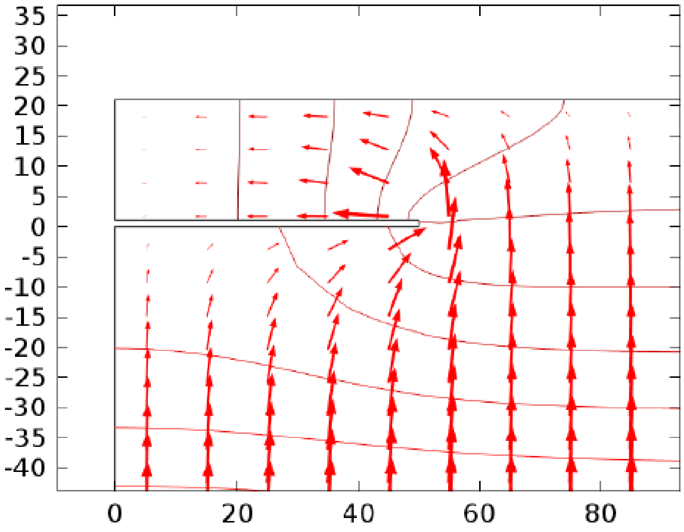

Figure 7.1 Heat flow near the edge of a defect.

II. Constant heat flux

When a constant heat flux is applied to the bottom surface of the substrate, the temperature both of the substrate and film continues to rise, and $T_s$–$T_{dc}$ increases until it achieves steady state after a certain time. The selection of the heat flux and pulse duration is essential to maintain a measurable temperature difference while keeping the temperature as low as possible. Comparing the results of two methods, i.e., constant temperature and constant heat flux, for the same maximum temperature increment, the maximum observable temperature difference of the latter is 143% greater ((6.37–2.62 °C)/2.62 °C) for the particular studied case.

Moreover, the internal heat flow of the structure obtained in the constant heat flux method has a similar transfer orientation as that obtained in the constant temperature method. Therefore, the surface temperature is maximized near the defect edge and can be used to locate the defect edge.

### 7.1.2 Temperature Difference for Various Excitation Methods

In the temperature stimulations, according to the dynamic temperature field analysis results, the peak value of the temperature difference occurs at the same time for different temperature increments. While under constant heat flux conditions, a high-power heat flux and short pulse duration can induce a large temperature difference, while a low-power heat flux and long pulse duration result in a small temperature difference within the same temperature increment. However, better results are obtained when the pulse duration is longer than the time it takes for the temperature difference to stabilize. Otherwise, the temperature difference may be less under an excessively high heat flux and short pulse duration.

### 7.1.3 Detectability versus the Thermal Characteristics and Thickness of the Film and Substrate

I. Material of the thin film and substrate

When the same structure is used, the substrate material greatly influences the temperature difference under the same thermal excitation conditions. The maximum temperature difference is reached earlier if the substrate is composed of a higher thermal diffusivity material. In this case, the maximum temperature difference increases almost linearly with the thermal diffusivity.

When the thermal diffusivity of the top layer varies, the trend in the temperature difference is opposite to that of the substrate. The numerical results show that the maximum temperature difference is proportional to the reciprocal of $\sqrt{\alpha t}$, which indicates that the maximum temperature difference is proportional to the half power of the time it takes for heat to transfer from the defect edge to the defect centre.

Thus, we suggest using the parameter $\alpha_{sub}/\sqrt{\alpha_{fim}}$ to characterize the achievable maximum temperature difference to detect internal delamination defects by combining these two theories. The maximum temperature difference linearly decreases with the parameter $\alpha_{sub}/\sqrt{\alpha_{fim}}$, which makes the test applicable to a wide range of materials.

II. Thickness of the film and substrate

The simulation results show that the influence of the substrate thickness is opposite to that of the thermal diffusivity. Increasing the thickness of the substrate decreases the maximum temperature and delays the time at which the maximum temperature is obtained. The influence of the film thickness is the same as that of the thermal diffusivity: the temperature difference decreases with the thickness. In summary, the thermal diffusion in the vertical direction of the substrate (diffusivity/thickness) increases the maximum temperature difference and reduces the time necessary to achieve the maximum temperature difference, while the temperature difference increases as the thermal resistance of the film $(1/L_{film}\sqrt{\alpha_{film}})$ increases. Therefore, these parameters can also be used to characterize the detectability of the test technology.

## 7.2 Comparison of the Experimental and Simulation Results using Lock-in Thermography

Periodic pulse heat flux is also called the lock-in method, and lock-in thermographic NDT can reduce the noise in the experiment. Comparing the simulation and experimental results led to the following conclusions: the specimens with a low thermal diffusivity top layer material (acrylic) present a clear image of the defects, while that with the high thermal diffusivity material (copper) do not produce a clear image of the internal structure; the defect size has a large influence on the surface temperature difference; and the location of the maximum temperature gradient reveals the defect edge.

## 7.3 Future Work

Due to the constraints of research facilities, a number of areas have not been fully investigated this study. Therefore, future work on transmission thermographic NDT method will focus on the following:

- The materials in this research all have isotropic thermal diffusivity. According to the analysis results, heat transfer in the vertical direction of the substrate and the horizontal direction of the film are the two main factors that influence the temperature difference and detectability. Thus, future work would involve the simulation of a wider range of isotropic materials.
- This research focused on two fundamental excitation methods: constant temperature and constant heat flux. However, in real detection, there are many excitation sources with other heating methods, such as the eddy current hot plate method, which involve a dynamic heat flux and distance and can achieve a very high temperature in a short time. These other methods can be adopted in experiment and simulation to improve the detectability.
- Transmission transient thermographic NDT is not widely used for MEMS devices due to the speed of the thermal camera. According to the simulation results, a maximum temperature difference occurs on the order of hundreds of microseconds, which is difficult for most thermal cameras to achieve. Moreover, high-speed and high-resolution cameras often require very high temperatures, which is unrealistic for MEMS devices. In future work, synchronizing the excitation source and detector may overcome the shortcoming of the camera speed.
- Although lock-in thermographic NDT can improve the NETD, the available equipment is still unsuitable for applications involving high thermal diffusivity materials, such as copper. For future work, improving the detectability of such

materials may rely on the configuration of the detection method, i.e., decreasing the external temperature or strong convective surface cooling.

- The pixel resolution of the thermal camera is a critical limitation of thermographic NDT, as the IR wavelength ranges from 760 nm to 1 mm, which limits the pixel resolution to the micrometre scale, which is too high for some MEMS devices. However, thermoreflectance microscopy with blue illumination can offer thermal and pixel resolutions as small as 10 mK and 250 nm [177]. This method is based on thermoreflectance imaging, which measures the fractional change in the reflectivity of the surface in response to variations in the surface temperature. Knowledge of the material-dependent thermoreflectance coefficient enables the calculation of the temperature change from the measured fractional change in the reflectivity of the sample. Because the spatial resolution scales linearly with wavelength, a shorter wavelength can be chosen to resolve a smaller distance [178]. Therefore, this is one direction for future work

# References

[1] Hsu, T. R. (2006, March). Reliability in MEMS packaging. In *2006 IEEE International Reliability Physics Symposium Proceedings* (pp. 398-402). IEEE.

[2] Zhao, Y. P., Wang, L. S., & Yu, T. X. (2003). Mechanics of adhesion in MEMS—a review. *Journal of Adhesion Science and Technology*, 17(4), 519-546.

[3] Srikar, V. T., & Spearing, S. M. (2003). A critical review of microscale mechanical testing methods used in the design of microelectromechanical systems. *Experimental mechanics*, 43(3), 238-247.

[4] Chang, L. (2006). Foundations of MEMS. *Person Prentice Hall*, 30-33

[5] Harris, N. R., Hill, M., Torah, R., Townsend, R., Beeby, S., White, N. M., & Ding, J. (2006). A multilayer thick-film PZT actuator for MEMs applications.*Sensors and Actuators A: Physical*, 132(1), 311-316.

[6] Pritchard, J., Bowen, C. R., & Lowrie, F. (2013). Multilayer actuators: review. *British Ceramic Transactions*.

[7] Franssila, S. (2010). *Introduction to microfabrication*. John Wiley & Sons.

[8] Witvrouw, A., Tilmans, H. A. C., & De Wolf, I. (2004). Materials issues in the processing, the operation and the reliability of MEMS. *Microelectronic Engineering*, 76(1), 245-257.

[9] Tadigadapa, S., & Najafi, N. (2001, October). Reliability of micro-electro-mechanical systems (MEMS). In *Micromachining and Microfabrication* (pp. 197-205). International Society for Optics and Photonics. Proc. SPIE Vol. 4558, Rajeshuni Ramesham

[10] Scott, I. G., & Scala, C. M. (1982). A review of non-destructive testing of composite materials. *NDT international*, *15*(2), 75-86.

[11] Chiou, Y. C., Liu, J. Z., & Liang, Y. T. (2011). Micro crack detection of multi-crystalline silicon solar wafer using machine vision techniques. *Sensor Review*, *31*(2), 154-165.

[12] McCann, D. M., & Forde, M. C. (2001). Review of NDT methods in the assessment of concrete and masonry structures. *NDT & E International*,*34*(2), 71-84.

[13] Drinkwater, B. W., & Wilcox, P. D. (2006). Ultrasonic arrays for non-destructive evaluation: A review. *NDT & E International*, *39*(7), 525-541.

[14] Lin, C. L., & Miller, J. D. (2002). Cone beam X-ray microtomography-a new facility for three-dimensional analysis of multiphase materials. *Minerals and Metallurgical Processing*, *19*(2), 65-71.

[15] Bechou, L., Ousten, Y., & Danto, Y. (2001). New methods for scanning ultrasonic microscopy applications for failure analysis of microassembling technologies. In *Physical and Failure Analysis of Integrated Circuits, 2001. IPFA 2001. Proceedings of the 2001 8th International Symposium on the*(pp. 195-201). IEEE.

[16] Lowrie, C., Desmulliez, M. P., Hoff, L., Jakob Elle, O., & Fosse, E. (2009). Fabrication of a MEMS accelerometer to detect heart bypass surgery complications. *Sensor Review*, *29*(4), 319-325.

[17] Maldague, X. P. (2002). Introduction to NDT by active infrared thermography. *Materials Evaluation*, *60*(9), 1060-1073. W P Eaton, J. H. (1997, May 28). Micromachined pressure sensors: review and recent developments. *Smart Mater. Struct.6*, pp. 530–539.

[18] M. Gęca, A. K. (2013, May). Design, modeling and simulation of MEMS pressure sensors. *Photonics Applications in Astronomy, Communications, Industry, and High-Energy Physics Experiments 2013.* Wilga, Poland: SpIE, P.O. Box 10, Bellingham, WA 98227-0010, United States.

[19] Simion, S., Bartolucci, G., & Marcelli, R. (2006, May). MEMS Based Tunable Band-Stop Structure. In *2006 International Conference on Microwaves, Radar & Wireless Communications* (pp. 159-162). IEEE.

[20] Haogang Cai, Z. Y. (2008, March 10). Fabrication of a MEMS inertia switch on quartz substrate and evaluation of its threshold acceleration. *Microelectronics Journal 39*, pp. 1112–1119.

[21] Zhang, X. M., Liu, A. Q., Tang, D. Y., & Lu, C. (2004). Discrete wavelength tunable laser using microelectromechanical systems technology. *Applied Physics Letters*, *84*(3), 329-331.

[22] Liu, A. Q., Zhang, X. M., Cai, H., Tang, D. Y., & Lu, C. (2005). Miniaturized injection-locked laser using microelectromechanical systems technology. *Applied Physics Letters*, *87*(10), 101101.

[23] Zhang, X. M., Liu, A. Q., Cai, H., Yu, A. B., & Lu, C. (2007). Retro-axial VOA using parabolic mirror pair. *IEEE Photonics Technology Letters*, *19*(9/12), 692.

[24] Schiavone, G., Desmulliez, M. P., & Walton, A. J. (2014). Integrated Magnetic MEMS Relays: Status of the Technology. *Micromachines*, *5*(3), 622-653.

[25] Cai, H., Zhang, X. M., Wu, J., Tang, D. Y., Zhang, Q. X., & Liu, A. Q. (2007, June). MEMS tunable dual-wavelength laser with large tuning range. In *TRANSDUCERS 2007-2007 International Solid-State Sensors, Actuators and Microsystems Conference* (pp. 1433-1436). IEEE.

[26] Cai, H., Yang, Z., Ding, G., & Zhao, X. (2008). Fabrication of a MEMS inertia switch on quartz substrate and evaluation of its threshold acceleration. *Microelectronics Journal*, *39*(9), 1112-1119

[27] Zimmermann, L., Ebersohl, J. P., Le Hung, F., Berry, J. P., Baillieu, F., Rey, P., ... & Caillat, P. (1995). Airbag application: a microsystem including a silicon capacitive accelerometer, CMOS switched capacitor electronics and true self-test capability. *Sensors and Actuators A: Physical*, *46*(1), 190-195.

[28] Wood, R., Mahadevan, R., Dhuler, V., Dudley, B., Cowen, A., Hill, E., et al. (1998). MEMS microrelays. *Mechatronics*, *8*(5), 535-547..

[29] Zavracky, P. M., Majumder, S., & McGruer, N. E. (1997). Micromechanical switches fabricated using nickel surface micromachining. *Journal of Microelectromechanical Systems*, *6*(1), 3-9.

[30] Stanimirović, I., & Stanimirović, Z. (2009). „Reliability of MEMS “. *Micro Electronic and Mechanical Systems, Rijeka: InTech*, 177-184.

[31] Unger, M. A., Chou, H. P., Thorsen, T., Scherer, A., & Quake, S. R. (2000). Monolithic microfabricated valves and pumps by multilayer soft lithography.*Science*, *288*(5463), 113-116.

[32] van Spengen, W. M., De Wolf, I., Puers, R., & Vikhagen, E. (2001, January). Optical imaging of high-frequency resonances and semi-static deformations in micro-electromechanical systems (MEMS). In *International Symposium for Testing and Failure Analysis* (pp. 357-364). ASM International; 1998.

[33] Franssila, S. (2010). *Introduction to microfabrication* John Wiley & Sons.

[34] Joliff, Y., Absi, J., Huger, M., & Glandus, J. C. (2008). Microcracks with unexpected characteristics induced by CTE mismatch in two-phase model materials. *Journal of Materials Science, 43*(1), 330-337.

[35] Stanimirović, Z., & Stanimirović, I. (2009). Mechanical properties of MEMS materials. *Micro Electronic and Mechanical Systems, in Tech*, , 177-184.

[36] Schiavone, G., Bunting, A. S., Desmulliez, M. P., & Walton, A. J. (2015). Fabrication of Electrodeposited Ni–Fe Cantilevers for Magnetic MEMS Switch Applications. *Journal of Microelectromechanical Systems, 24*(4), 870-879.

[37] Stark, B. (1999). MEMS reliability assurance guidelines for space applications..

[38] Schiavone, G., Desmulliez, M. P. Y., Smith, S., Murray, J., Sirotkin, E., Terry, J. G., ... & Walton, A. J. (2012, March). Quantitative wafer mapping of residual stress in electroplated NiFe films using independent strain and Young's modulus measurements. In *Microelectronic Test Structures (ICMTS), 2012 IEEE International Conference on* (pp. 105-110). IEEE.

[39] Chen, W. T., & Nelson, C. W. (1979). Thermal stress in bonded joints. *IBM Journal of Research and Development*, *23*(2), 179-188

[40] Clarke, I. C. (1971). Articular cartilage: a review and scanning electron microscope study. *Bone & Joint Journal, 53*(4), 732-750

[41] Suzuki, E. (2002). High-resolution scanning electron microscopy of immunogold-labelled cells by the use of thin plasma coating of osmium.*Journal of Microscopy*, *208*(3), 153-157.

[42] Zhao, Y. (2012). Nondestructive Testing and Fatigue Analysis Based on Lock-in infrared thermography. *Dalian University of Technology Press* (In Chinese).

[43] Sposito, G., Ward, C., Cawley, P., Nagy, P. B., & Scruby, C. (2010). A review of non-destructive techniques for the detection of creep damage in power plant steels. *Ndt & E International*, *43*(7), 555-567.

[44] Scott, I. G., & Scala, C. M. (1982). A review of non-destructive testing of composite materials. *NDT international*, *15*(2), 75-86.

[45] Wickramasinghe, H. K. (1983). Scanning acoustic microscopy: a review.*Journal of Microscopy*, *129*(1), 63-73.

[46] Blitz, J., & Simpson, G. (1996). *Ultrasonic methods of non-destructive testing* (Vol. 2). Springer Science & Business Media

[47] Kessler, L. W. (1974). Review of progress and applications in acoustic microscopy. *The Journal of the Acoustical Society of America*, *55*(5), 909-918.

[48] Maillet, I., Michel, L., Souric, F., & Gourinat, Y. (2015). Mode II fatigue delamination growth characterization of a carbon/epoxy laminate at high frequency under vibration loading. *Engineering Fracture Mechanics*.

[49] Renshaw, J., Holland, S. D., Thompson, R. B., & Anderegg, J. (2011). Vibration-induced tribological damage to fracture surfaces via vibrothermography. *International Journal of Fatigue*, *33*(7), 849-857.

[50] Holland, S. D., Uhl, C., Ouyang, Z., Bantel, T., Li, M., Meeker, W. Q., ... & Eisenmann, D. (2011). Quantifying the vibrothermographic effect. *NDT & E International*, *44*(8), 775-782.

[51] Rochow, E. (2012). *An introduction to microscopy by means of light, electrons, x-rays, or ultrasound*. Springer Science & Business Media.

[52] Bechou, L., Ousten, Y., & Danto, Y. (2001). New methods for scanning ultrasonic microscopy applications for failure analysis of microassembling technologies. In *Physical and Failure Analysis of Integrated Circuits, 2001. IPFA 2001. Proceedings of the 2001 8th International Symposium on the*(pp. 195-201). IEEE.

[53] Lin, C. L., & Miller, J. D. (2002). Cone beam X-ray microtomography-a new facility for three-dimensional analysis of multiphase materials. *Minerals and Metallurgical Processing*, *19*(2), 65-71

[54] J. Blitz. (1997). *Electrical and magnetic methods of non-destructive testing*(Vol. 3). Springer Science & Business Media.

[55] García-Martín, J., Gómez-Gil, J., & Vázquez-Sánchez, E. (2011). Non-destructive techniques based on eddy current testing. *Sensors*, *11*(3), 2525-2565.

[56] Lovejoy, M. J. (2012). *Magnetic particle inspection: a practical guide*. Springer Science & Business Media.

[57] Jiles, D. C. (1990). Review of magnetic methods for nondestructive evaluation (Part 2). *NDT International*, *23*(2), 83-92.

[58] Jiles, D. C. (1998). *Introduction to magnetism and magnetic materials*. CRC press.

[59] De la Torre-Ibarra, M. H., Ruiz, P. D., & Huntley, J. M. (2006). Double-shot depth-resolved displacement field measurement using phase-contrast spectral optical coherence tomography. *Optics express*, 14(21), 9643-9656.

[60] Maranon, A., Ruiz, P. D., Nurse, A. D., Huntley, J. M., Rivera, L., & Zhou, G. (2007). Identification of subsurface delaminations in composite laminates. *Composites Science and Technology*, *67*(13), 2817-2826.

[61] Ruiz, P. D., Jumbo, F., Seaton, A., Huntley, J. M., Ashcroft, I. A., & Swallowe, G. M. (2006). Numerical and experimental investigation of three-dimensional strains in adhesively bonded joints. *The Journal of Strain Analysis for Engineering Design*, *41*(8), 583-596.

[62] Ruiz, P. D., Huntley, J. M., Shen, Y., Coggrave, C. R., & Kaufmann, G. H. (2001). Vibration-induced phase errors in high-speed phase-shifting speckle-pattern interferometry. *Applied optics*, *40*(13), 2117-2125.

[63] Majumdar, A., Luo, K., Shi, Z., & Varesi, J. (1996). Scanning thermal microscopy at nanometer scales: a new frontier in experimental heat transfer. *Experimental Heat Transfer An International Journal*, *9*(2), 83-103

[64] Roemer, J., Pieczonka, L., Szwedo, M., Uhl, T., & Staszewski, W. J. (2013). Thermography of Metallic and Composite Structures-review of applications. *Int. Work. Smart Mater. Struct. SHM*, *18*(11).

[65] Hartless, P. C. M., & Whalley, D. C. (1991, October). Automated thermographic inspection of surface mount solder joints. In *Automotive Electronics, 1991., Eighth International Conference on* (pp. 178-181). IET.

[66] Schmerr Jr, L. W. (2013). *Fundamentals of ultrasonic nondestructive evaluation: a modeling approach*. Springer Science & Business Media.

[67] Sakagami, T., & Kubo, S. (2002). Applications of pulse heating thermography and lock-in thermography to quantitative nondestructive evaluations. *Infrared Physics & Technology*, *43*(3), 211-218.

[68] Kordatos, E. Z., Aggelis, D. G., & Matikas, T. E. (2012). Monitoring mechanical damage in structural materials using complimentary NDE techniques based on thermography and acoustic emission. *Composites Part B: Engineering*, *43*(6), 2676-2686.

[69] Lee, J. H., & Gianchandani, Y. B. (2004). High-resolution scanning thermal probe with servocontrolled interface circuit for microcalorimetry and other applications. *Review of scientific instruments*, *75*(5), 1222-1227.

[70] Barr, E. S. (1961). The infrared pioneers—I. Sir William Herschel. *Infrared Physics*, *1*(1), 1-IN6.

[71] Ibarra-Castanedo, C., & Maldague, X. (2004). Pulsed phase thermography reviewed. *Quantitative Infrared Thermography Journal*, *1*(1), 47-70.

[72] Maldague, X. P. (2012). *Nondestructive evaluation of materials by infrared thermography*. Springer Science & Business Media.

[73] Barker, G. A. (1934). *U.S. Patent No. 1,959,702*. Washington, DC: U.S. Patent and Trademark Office.

[74] Maldague, X. P. (2002). Introduction to NDT by active infrared thermography. *Materials Evaluation*, *60*(9), 1060-1073.

[75] Bates, D., Smith, G., Lu, D., & Hewitt, J. (2000). Rapid thermal non-destructive testing of aircraft components. *Composites Part B: Engineering*,*31*(3), 175-185.

[76] Nilsson, S. K., & Gustafsson, S. E. (1974). Surface temperature over an implanted artificial heat source. *Physics in medicine and biology*, *19*(5), 677.

[77] Draper, J. W., & Boag, J. W. (1971). The calculation of skin temperature distributions in thermography. *Physics in medicine and biology*, *16*(2), 201.

[78] McLaughlin, P. V. Jr.; McAssey, E. V. Jr.; Koert, D. N.; and Deitrich, R. C., "NDT of Composites by Thermography" (1981). *Proceedings of the DARPA/AFWAL Review of Progress in Quantitative NDE, October 1979–January 1981*. Paper 11.

[79] Rainieri, S., & Pagliarini, G. (2002). Data filtering applied to infrared thermographic measurements intended for the estimation of local heat transfer coefficient. *Experimental thermal and fluid science*, *26*(2), 109-114.

[80] Pickering, S., & Almond, D. (2008). Matched excitation energy comparison of the pulse and lock-in thermography NDE techniques. *NDT & E International*, *41*(7), 501-509.

[81] Ibarra-Castanedo, C., Genest, M., Guibert, S., Piau, J. M., Maldague, X. P., & Bendada, A. (2007, April). Inspection of aerospace materials by pulsed thermography, lock-in thermography, and vibrothermography: a comparative study. In *Defense and Security Symposium* (pp. 654116-654116). International Society for Optics and Photonics.

[82] Pickering, S., & Almond, D. (2008). Matched excitation energy comparison of the pulse and lock-in thermography NDE techniques. *NDT & E International*, *41*(7), 501-509.

[83] Maldague, X., & Marinetti, S. (1996). Pulse phase infrared thermography.*Journal of Applied Physics*, *79*(5), 2694-2698.

[84] Parker, W. J., Jenkins, R. J., Butler, C. P., & Abbott, G. L. (1961). Flash method of determining thermal diffusivity, heat capacity, and thermal conductivity. *Journal of applied physics*, *32*(9), 1679-1684.

[85] Milne, J. M., & Reynolds, W. N. (1985, March). The non-destructive evaluation of composites and other materials by thermal pulse video thermography. In *1984 Cambridge Symposium* (pp. 119-122). International Society for Optics and Photonics.

[86] Bellis, M. "Origins of Thermal Imaging or Infrared (IR) Imaging" 2015 About.com, [http://inventors.about.com/od/militaryhistoryinventions/p/thermal_image.htm](http://inventors.about.com/od/militaryhistoryinventions/p/thermal_image.htm)

[87] Guy Pas, Vice-President Worldwide, Systems Sales, FLIR Systems | Tuesday, March 18th, 2014, http://www.theneweconomy.com/technology/demand-for-flir-thermal-imaging-technology-sees-prices-drop

[88] Ishchuk, I. N. (2008). The detection of defects in materials using thermography. *Measurement Techniques*, *51*(4), 421-427.

[89] Swiderski, W. (2013). Detection of Very Thin Defects in Multi-Layer Composites Made of Carbon Fibre with IR Thermography Methods. In*Nondestructive Testing of Materials and Structures* (pp. 633-639). Springer Netherlands.

[90] Carslaw, H. S. (1959). S and Jaeger JC "Conduction of heat in solids". *Oxford Science Publications, ISBN 0*, *19*(853368), 3.

[91] Lehto, A., Jaarinen, J., Tiusanen, T., Jokinen, M., & Luukkala, M. (1981). Magnitude and phase in thermal wave imaging. *Electronics Letters*, *17*(11), 364-365.

[92] Leppänen, K., Saarela, J., & Fabritius, T. (2014, October). Synchronized thermography for multi-layer thin film characterization. In *SPIE Solar Energy+ Technology* (pp. 917705-917705). International Society for Optics and Photonics.

[93] Connolly, M. P. (1991). A review of factors influencing defect detection in infrared thermography: applications to coated materials. Journal of nondestructive evaluation, 10(3), 89-96.

[94] Suszyński, Z., & Bednarek, M. (2013). Application of the Correlation Function in the Detection of Thermal Heterogeneity Using Pulsed Thermography. *International Journal of Thermophysics*, *34*(4), 680-690.

[95] Asiegbu, G. O., Haidar, A. M., & Hawari, K. (2013, January). A Review of Defect Detection on Electrical Components Using Image Processing Technology. In *Proceedings of the Fourth International Conference on Signal and Image Processing 2012 (ICSIP 2012)* (pp. 247-255). Springer India.

[96] Maev, R. G., Gavrilov, D., Ghodsi, G., & Maeva, E. Y. (2011). An Experimental Comparison of Thermographic and Acoustical Methods for Evaluation of Layered Structures. In *Acoustical Imaging* (pp. 181-192). Springer Netherlands.

[97] Nathan, B. E., Galasko, C. S. B., & Pallett, J. E. (1970). Thermography in breast cancer. *British Journal of Surgery*, *57*(7), 518-520.

[98] Kylili, A., Fokaides, P. A., Christou, P., & Kalogirou, S. A. (2014). Infrared thermography (IRT) applications for building diagnostics: A review. *Applied Energy*, *134*, 531-549.

[99] Borazjani, E., Spinello, D., & Necsulescu, D. S. (2015). Determination of the modulation frequency for thermographic non-destructive testing. *NDT & E International*, *70*, 1-8.

[100] Vavilov, V. P. (2015). Dynamic thermal tomography: Recent improvements and applications. *NDT & E International*, *71*, 23-32.

[101] Tomić, L. D., & Elazar, J. M. (2013). Pulse thermography experimental data processing by numerically simulating thermal processes in a sample with periodical structure of defects. *NDT & E International, 60,* 132-135.

[102] Maize, K., Ezzahri, Y., Wang, X., Singer, S., Majumdar, A., & Shakouri, A. (2008, March). Measurement of thin film isotropic and anisotropic thermal conductivity using 3ω and thermoreflectance imaging. In *Semiconductor*

*Thermal Measurement and Management Symposium, 2008. Semi-Therm 2008. Twenty-fourth Annual IEEE* (pp. 185-190). IEEE.

[103] Almond, D. P., & Pickering, S. G. (2012). An analytical study of the pulsed thermography defect detection limit. *Journal of applied physics*, *111*(9), 093510.

[104] Receveur, R. A., Lindemans, F. W., & de Rooij, N. F. (2007). Microsystem technologies for implantable applications. *Journal of Micromechanics and Microengineering*, *17*(5), R50.

[105] Fürjes, P., Bognár, G., & Bársony, I. (2006). Powerful tools for thermal characterisation of MEMS. *Sensors and Actuators B: Chemical*, *120*(1), 270-277.

[106] Serio, B., Hunsinger, J. J., Conseil, F., Derderian, P., Collard, D., Buchaillot, L., & Ravat, M. F. (2005, June). Close infrared thermography using an intensified CCD camera: application in nondestructive high resolution evaluation of electrothermally actuated MEMS. In *Optical Metrology* (pp. 819-829). International Society for Optics and Photonics.

[107] Maldague, X. P. (2012). *Nondestructive evaluation of materials by infrared thermography*. Springer Science & Business Media.

[108] Holman, J.P. (2005). *Heat Transfer.* McGraw-Hill Book Co.

[109] Ghaffarian, R., 2000. Accelerated thermal cycling and failure mechanisms for BGA and CSP assemblies. *Journal of Electronic Packaging*, 122 (4), 335-340

[110] Colin. M. (2009). *DELI VERABLE D4, MANUFACTURI NG.* Polynoe.

[111] W, R. M. (2011). The effect of mechanical parameters of switch-type contact on relay operation characteristics. *2011 IEEE 57th Holm Conference on Electrical Contacts, Holm 2011 0 Proceedings of Electrical Contacts-2011* (pp. 112-116). Minneapolis, MN, United states: Institute of Electrical and Electronics Engineers Inc, 445 Hoes Lane?P.O. Box 1331. Piscataway, NJ 08855-1331, United States.

[112] H. Lee, R. A. (2006, Feb 8). Characterization of metal and metal alloy films as contact materials in MEMS switches. *Journal of micromechanics and Microengineering*, pp. 557-563.

[113] V. Behrens, T. H. (October 4, 2010 - October 7, 2010). Failure of Arcing Contacts in Low Voltage Switching Devices. *56th IEEE Holm Conference on Electrical Contacts, HOLM 2010,* (pp. 254-260). Charleston, SC, United states.

[114] R. Wood, R. M. (1998, Aug). MEMS microrelays. *Mechatronics,* pp. 535-547.

[115] Poirier, J. P. (1985). *Creep of crystals: high-temperature deformation processes in metals, ceramics and minerals*. Cambridge University Press..

[116] Spengen, W. M. (2003, April). MEMS reliability from a failure mechanisms perspective. *Microelectronics Reliability 43* , pp. 1049–1060.

[117] C.H.Leung, A. L. (October 2, 1995 - October 4, 1995). Thermal modeling of electrical contacts in switches and relays. *Proceedings of the 41st IEEE Holm Conference on Electrical Contacts* (pp. 274-281). Montreal, Can: IEEE, Piscataway, NJ, United States.

[118] Department of Defense, MIL-STD-883E, Test Method Standard, Temperature Cycling, Method 1010.8, March 14, 2014

[119] Lexa, B, Alicona, Measurement Report, corrosion samples, 3D Measurement settings, September 29, 2008.

[120] Victoreen, J. A. (1949). The Calculation of X-Ray Mass Absorption Coefficients. *Journal of Applied Physics*, *20*(12), 1141-1147.

[121] Conseil, F. (2008) Quarterly Status Repoert and Deliverable D1, Reliability Specifications.

[122] KIT catalogue, DualBeam (FIB-SEM) Microscope System, https://equipment.lboro.ac.uk/id/item/244/dualbeam-fib-sem-microscope-system.html.

[123] Nikon official website, X-ray and CT Inspection, http://www.nikonmetrology.com/en_EU/Products/X-ray-and-CT-Inspection, Nikon metrology nv, [Accessed on 1/1/2016]

[124] Schulz, M. J., & Caldwell, L. V. (1995, May). Nonuniformity correction and correctability of infrared focal plane arrays. In *SPIE's 1995 Symposium on OE/Aerospace Sensing and Dual Use Photonics* (pp. 200-211). International Society for Optics and Photonics.

[125] Maligno, A., Whalley, D. and Silberschmidt, V., (2010). *Interfacial failure under thermal fatigue loading in multilayered MEMS structures:* IOP Publishing.

[126] Venkataraju, C. (2009). Effect of Nickel on the Structural Properties of Mn Zn Ferrite Nano Particles. *Applied Physics Research*, *1*(1), 41.

[127] Bergman, T. L., Incropera, F. P., & Lavine, A. S. (2011). *Fundamentals of heat and mass transfer*. John Wiley & Sons.

[128] Campbell, S. A. (2001). *The science and engineering of microelectronic fabrication*. Oxford University Press.

[129] Jeong, C., Datta, S., & Lundstrom, M. (2012). Thermal conductivity of bulk and thin-film silicon: A Landauer approach. *Journal of Applied Physics*,*111*(9), 093708.

[130] Nath, P., & Chopra, K. L. (1974). Thermal conductivity of copper films. *Thin Solid Films, 20*(1), 53-62.

[131] Sugawara, H., Ohkubo, T., Fukushima, T., & Iuchi, T. (2003). Emissivity measurement of silicon semiconductor wafer near room temperature. In*SICE 2003 Annual Conference (IEEE Cat. No. 03TH8734).*

[132] Ravindra, N. M., Sopori, B., Gokce, O. H., Cheng, S. X., Shenoy, A., Jin, L., ... & Zhang, Y. (2001). Emissivity measurements and modeling of silicon-related materials: an overview. *International journal of thermophysics, 22*(5), 1593-1611.

[133] Nguyen, N. T. (1997). Micromachined flow sensors—a review. *Flow measurement and Instrumentation, 8*(1), 7-16.

[134] Bustillo, J. M., Howe, R. T., & Muller, R. S. (1998). Surface micromachining for microelectromechanical systems. *Proceedings of the IEEE, 86*(8), 1552-1574.

[135] Sørensen, B. F., Sarraute, S., Jørgensen, O., & Horsewell, A. (1998). Thermally induced delamination of multilayers. *Acta materialia*, *46*(8), 2603-2615.

[136] Khanna, V. K. (2011). Adhesion–delamination phenomena at the surfaces and interfaces in microelectronics and MEMS structures and packaged devices. *Journal of Physics D: Applied Physics*, *44*(3), 034004.

[137] Lucenko, G., & Gusak, A. (2003). A model of the growth of intermediate phase islands in multilayers. *Microelectronic engineering*, *70*(2), 529-532.

[138] Tu, P. L., Chan, Y. C., & Lai, J. K. L. (1997). Effect of intermetallic compounds on the thermal fatigue of surface mount solder joints.*Components, Packaging, and Manufacturing Technology, Part B: Advanced Packaging, IEEE Transactions on*, *20*(1), 87-93

[139] Xu, L., & Pang, J. H. (2006, June). Effect of intermetallic and Kirkendall voids growth on board level drop reliability for SnAgCu lead-free BGA solder joint. In *Electronic Components and Technology Conference, 2006. Proceedings. 56th* (pp. 8-pp). IEEE.

[140] Choi, S. R., Hutchinson, J. W., & Evans, A. G. (1999). Delamination of multilayer thermal barrier coatings. *Mechanics of Materials, 31*(7), 431-447.

[141] Frederikse, H. P. R., Fields, R. J., & Feldman, A. (1992). Thermal and electrical properties of copper-tin and nickel-tin intermetallics. *Journal of applied physics*, *72*(7), 2879-2882.

[142] Carey, V. P., Chen, G., Grigoropoulos, C., Kaviany, M., & Majumdar, A. (2008). A review of heat transfer physics. *Nanoscale and Microscale Thermophysical Engineering*, *12*(1), 1-60.

[143] Tritt, T. M. (2004). *Thermal conductivity: theory, properties, and applications*. Springer Science & Business Media.

[144] Jones, W., & March, N. H. (1985). *Theoretical solid state physics: Perfect lattices in equilibrium* (Vol. 1). Courier Corporation.

[145] Asheghi, M., Touzelbaev, M. N., Goodson, K. E., Leung, Y. K., & Wong, S. S. (1998). Temperature-dependent thermal conductivity of single-crystal silicon layers in SOI substrates. *Journal of Heat Transfer, 120*(1), 30-36.

[146] Tian, M. (2003). *Substrate for High Density Package*. Tsinghua University Press.

[147] Ho, C. Y., Ackerman, M. W., Wu, K. Y., Oh, S. G., & Havill, T. N. (1978). Thermal conductivity of ten selected binary alloy systems. *Journal of Physical and Chemical Reference Data*, *7*(3), 959-1178.

[148] Chen, G., & Shakouri, A. (2002). Heat transfer in nanostructures for solid-state energy conversion. *Journal of Heat Transfer*, *124*(2), 242-252.

[149] Asheghi, M., Touzelbaev, M. N., Goodson, K. E., Leung, Y. K., & Wong, S. S. (1998). Temperature-dependent thermal conductivity of single-crystal silicon layers in SOI substrates. *Journal of Heat Transfer*, *120*(1), 30-36.

[150] Stewart, D., & Norris, P. M. (2000). Size effects on the thermal conductivity of thin metallic wires: microscale implications. *Microscale Thermophysical Engineering*, *4*(2), 89-101.

[151] Vlachopoulos, J., & Strutt, D. (2002). Basic Heat Transfer and Some Application in Polymer Processing. *Plastics Technician's Toolbox*, 21-33.

[152] Swaminathan, R., Bhaskaran, H., Sandborn, P., Subramanian, G., Deeds, M., & Cochran, K. R. (2003). Reliability assessment of delamination in chip-to-chip bonded MEMS packaging. *Advanced Packaging, IEEE Transactions on*, *26*(2), 141-151.

[153] Szabó, B., & Babuška, I. (2011). *Introduction to Finite Element Analysis: Formulation, Verification and Validation* (Vol. 35). John Wiley & Sons.

[154] Official website from COMSOL. URL: http://www.comsol.com/products. [Accessed on 27/12/2015].

[155] Material Library of COMSOL. URL: https://www.comsol.com/material-library. [Accessed on 27/12/2015]

[156] Abramowitz, M., & Stegun, I. A. (1966). Handbook of mathematical functions. *Applied Mathematics Series*, *55*, *62*.

[157] Martell, S. R., Semmens, J. E., & Kessler, L. W. (2001, October). Nondestructive acoustic microimaging (AMI) analysis of MEMS materials, manufacturing, and packaging. In *Micromachining and Microfabrication* (pp. 260-267). International Society for Optics and Photonics.

[158] Eldridge, J. I., Spuckler, C. M., & Martin, R. E. (2006). Monitoring Delamination Progression in Thermal Barrier Coatings by Mid-Infrared Reflectance Imaging. *International journal of applied ceramic technology*,*3*(2), 94-104.

[159] Jayadevan, K. P., & Tseng, T. Y. (2002). Review Composite and multilayer ferroelectric thin films: processing, properties and applications. *Journal of Materials Science: Materials in Electronics*, *13*(8), 439-459.

[160] Linder, C., Paratte, L., Gretillat, M. A., Jaecklin, V. P., & De Rooij, N. F. (1992). Surface micromachining. *Journal of Micromechanics and Microengineering*, *2*(3), 122.

[161] Huang, Y., Vasan, A. S. S., Doraiswami, R., Osterman, M., & Pecht, M. (2012). MEMS reliability review. *Device and Materials Reliability, IEEE Transactions on*, *12*(2), 482-493.

[162] Milne, J. M., & Reynolds, W. N. (1985, March). The non-destructive evaluation of composites and other materials by thermal pulse video thermography. In *1984 Cambridge Symposium* (pp. 119-122). International Society for Optics and Photonics.

[163] Werner, M. R., & Fahrner, W. R. (2001). Review on materials, microsensors, systems and devices for high-temperature and harsh-environment applications. *Industrial Electronics, IEEE Transactions on*, *48*(2), 249-257.

[164] Werdecker, W., & Aldinger, F. (1984). Aluminum nitride-an alternative ceramic substrate for high power applications in microcircuits. *Components, Hybrids, and Manufacturing Technology, IEEE Transactions on*, *7*(4), 399-404.

[165] Liu, L., & Edgar, J. H. (2002). Substrates for gallium nitride epitaxy.*Materials Science and Engineering: R: Reports*, *37*(3), 61-127.

[166] Ahmad, S. S., Jacobson, J., Johnson, Z., Mattson, K., Reinholz, A. & Strommen, G. (2010, January). A Novel Metal Core Substrate with Simplified Manufacturing Process and High Adhesion Conformal Dielectric and Circuitry Metal for High Density Chip-Scale Packaging Applications. In *International Symposium on Microelectronics*(Vol. 2010, No. 1, pp. 000638-000645). International Microelectronics Assembly and Packaging Society.

[167] Bergman, T. L., Incropera, F. P., & Lavine, A. S. (2011). *Fundamentals of heat and mass transfer*. John Wiley & Sons.

[168] Coutu Jr, R. A., Kladitis, P. E., Leedy, K. D., & Crane, R. L. (2004). Selecting metal alloy electric contact materials for MEMS switches. *Journal of Micromechanics and Microengineering, 14*(8), 1157.

[169] Chong, N., Chan, H. L. W., & Choy, C. L. (2002). Pyroelectric sensor array for in-line monitoring of infrared laser. *Sensors and Actuators A: Physical,96*(2), 231-238.

[170] Bergman, T. L., Incropera, F. P., & Lavine, A. S. (2011). *Fundamentals of heat and mass transfer*. John Wiley & Sons.

[171] Shu, H., Jianzhong, Z., Lingling, H., & Xiaodong, Y. (2012). Laser bending experiment and mechanical properties analysis of C194 copper alloy sheet.*Journal of Jiangsu University (Natural Science Edition), 1*, 021..

[172] Arkema Inc. (2000). Material Safety Data Sheet, Philadelphia, Pennsylvania 19103

[173] FLIR SC7000 Series, FLIR Systems UK, http://www.flirmedia.com/MMC/THG/Brochures/RND_017/RND_017_US.pdf, [Accessed on 29/12/2015]

[174] Ranjit, S., Choi, M., & Kim, W. (2016). Quantification of defects depth in glass fiber reinforced plastic plate by infrared lock-in thermography. *Journal of Mechanical Science and Technology, 30*(3), 1111-1118.

[175] Ranjit, S., Kang, K., & Kim, W. (2015). Investigation of lock-in infrared thermography for evaluation of subsurface defects size and

depth. *International Journal of Precision Engineering and Manufacturing*, *16*(11), 2255-2264.

[176] MathWorks, Matlab 2012a, Matlab offical website http://uk.mathworks.com/index.html?s_tid=gn_logo [Accessed on 1/1/2016]

[177] Farzaneh, M., Maize, K., Lüerßen, D., Summers, J. A., Mayer, P. M., Raad, P. E., Pipe, K.P., Shakouri, A., Ram, R.J. & Hudgings, J. A. (2009). CCD-based thermoreflectance microscopy: principles and applications. *Journal of Physics D: Applied Physics*, *42*(14), 143001.

[178] Mayer, P. M., Luersen, D., Ram, R. J., & Hudgings, J. A. (2007). Theoretical and experimental investigation of thethermal resolution and dynamic range ofCCD-based thermoreflectance imaging. *Journal of The Optical Society of America A-optics Image Science and Vision*, 24(4), 1156-1163.